TECHNICAL REPORT STANDARD TITLE PAGE

1. REPORT NO.	2. GOVERNMENT ACCESSION NO.	3. RECIPIENT'S CATALOG NO.
WA-RD 455.1		

4. TITLE AND SUBTITLE
Modeling of Rigid Pavements:
Joint Shear Transfer Mechanisms and
Finite Element Solution Strategies

5. REPORT DATE
JULY 1998

6. PERFORMING ORGANIZATION CODE

7. AUTHOR(S)
William G. Davids, George M. Turkiyyah,
and Joe P. Mahoney

8. PERFORMING ORGANIZATION REPORT NO.

9. PERFORMING ORGANIZATION NAME AND ADDRESS
Washington State Transportation Center (TRAC)
University of Washington, Box 354802
University District Building; 1107 NE 45th Street, Suite 535
Seattle, Washington 98105-4631

10. WORK UNIT NO.

11. CONTRACT OR GRANT NO.
Agreement T9903-54

12. SPONSORING AGENCY NAME AND ADDRESS
Washington State Department of Transportation
Transportation Building, MS 7370
Olympia, Washington 98504-7370

13. TYPE OF REPORT AND PERIOD COVERED
Final

14. SPONSORING AGENCY CODE

15. SUPPLEMENTARY NOTES
This study was conducted in cooperation with the U.S. Department of Transportation, Federal Highway Administration.

16. ABSTRACT

This report documents the modeling strategy and associated verification which permits analysis of multiple PCC plain jointed slabs. Several subbase/soil layers below the slabs and separation of the slab and base layer are considered. Load effects include those associated with both multiple tire and linear temperature gradients. A technique for modeling aggregate interlock shear transfer across PCC pavement joints is developed and verified. The overall development is contained in the computer program EverFE. The computer program uses a graphical user interface which aids its use.

17. KEY WORDS	18. DISTRIBUTION STATEMENT
Finite elements, rigid pavement, joints load transfer, aggregate interlock, EverFE	No restrictions. This document is available to the public through the National Technical Information Service, Springfield, VA 22616

19. SECURITY CLASSIF. (of this report)	20. SECURITY CLASSIF. (of this page)	21. NO. OF PAGES	22. PRICE
None	None	191	

Final Report
Research Project T9903, Task 54
Enhanced Finite Element Tools for Rigid Pavement Analysis

MODELING OF RIGID PAVEMENTS: JOINT SHEAR TRANSFER MECHANISMS AND FINITE ELEMENT SOLUTION STRATEGIES

by

William G. Davids, George M. Turkiyyah, and Joe P. Mahoney
Department of Civil and Environmental Engineering
University of Washington
Seattle, Washington 98195-2700

Washington State Transportation Center (TRAC)
University of Washington
Box 354802
University District Building
1107 NE 45th Street, Suite 535
Seattle, Washington 98105-4631

Washington State Department of Transportation
Technical Monitors

Robyn Moore
Pavement and Soils Engineer

Linda Pierce
Pavement Management Engineer

Prepared for

Washington State Transportation Commission
Department of Transportation
and in cooperation with
U.S. Department of Transportation
Federal Highway Administration

July 1998

DISCLAIMER

The contents of this report reflect the views of the authors, who are responsible for the facts and the accuracy of the data presented herein. The contents do not necessarily reflect the official views or policies of the Washington State Transportation Commission, Department of Transportation, or the Federal Highway Administration. This report does not constitute a standard, specification, or regulation.

Contents

List of Tables

J = dowel torsional moment of inertia

$\mathbf{J}$ = Jacobian matrix

k = modulus of subgrade reaction

$\mathbf{K}$ = system or element stiffness matrix

m = displacement magnitude of embedding element in gap direction

n = number of unknowns (nodal degrees of freedom)

N_i = i^{th} element shape function

$\mathbf{n}$ = unit normal vector

$\mathbf{N}$ = matrix of element shape functions

$\mathbf{P}, \mathbf{p}$ = vector of applied nodal forces

$(\mathbf{q}, \mathbf{s}, \mathbf{t})$ = dowel element local unit vectors

$\mathbf{Q}$ = basis transformation matrix for interface

$\mathbf{r}$ = system residual force vector

$\mathbf{R}$ = restriction operator

s = dowel local coordinate

$\mathbf{T}$ = interpolation operator; transformation matrix for dowel

(u, v, w) = scalar displacement components at a node in (i,j,k) directions

$\mathbf{u}, \mathbf{U}$ = system or element displacement vector

$\mathbf{v}$ = unit vector in direction of aggregate interlock shear

$\mathbf{y}$ = residual vector in constraint equation

$\mathbf{z}$ = displacement vector in conjugate gradient iteration

α = coefficient of thermal expansion

β = inner loop limit in multigrid algorithm

γ = magnitude of gap between dowel and slab

δ_n, δ_t = normal and tangential relative displacements across crack plane

δv = relative displacement between dowel and slab

Δ = vector of relative displacements

ϵ = residual solution tolerance

Abstract

This study addresses the need to better quantify and model load transfer across joints in rigid (concrete) pavement systems, and presents efficient solution strategies for making three-dimensional finite element analyses of rigid pavements and other large structural systems practical on desktop computers.

A modeling strategy is developed which permits the analysis of multiple slab systems having various geometries. Several soil layers below the slabs and separation of the slab and base layer are considered. Load effects include accurately located tire pressures and linear temperature gradients through the thickness of the slabs.

An embedded bending element is developed and verified that permits the precise location of dowels within the model without regard to meshing of the slab. Debonding and nonlinearities due to looseness of the dowels may be explicitly captured. Details of the inclusion of a general bond-slip law are also presented, extending the capabilities of the element to the modeling of more general reinforced concrete structures.

A technique for modeling aggregate interlock shear transfer across rigid pavement joints is developed that relies on a two-phase model for the concrete. The aggregate interlock model captures variations in shear stiffness and strength with aggregate size, concrete strength, and joint opening and relative tangential displacement.

An efficient iterative solution strategy for large-scale structural systems involving material and contact nonlinearities is developed and tested. This solution strategy relies on a multigrid-preconditioned conjugate gradient solver that permits the use of unstructured, unnested mesh sequences, the incorporation of nodal contact conditions, spatially varying materials, and the meshing of multiple element types within a single model.

Verification of the finite element models is accomplished through comparison with existing laboratory test data of doweled rigid pavements. A parametric study on the decrease in dowel load transfer due to dowel looseness is presented, as is a study on the effect of joint opening on aggregate interlock shear transfer. The potential for detrimental effects on rigid pavements due to poor load transfer is clearly demonstrated by these studies.

Chapter 1

Introduction

1.1 Context

Jointed plain concrete pavement (JPCP) has been in use throughout the world for many years [39], and is common in both roadways and airport runways. In general, JPCP consists of several components as illustrated in Fig. 1.1:

- Multiple unreinforced concrete slabs, often tied to each other by dowels (round steel bars) that assist in transferring load between slabs.
- Base layers consisting of compacted gravel or cement-treated soils, which are often placed below the slabs to better distribute load to the natural subgrade.
- The natural subgrade below the base layers.

A significant feature of JPCP are the joints, which are of two primary types: contraction and construction (see Fig. 1.2). Contraction joints are usually spaced about every 3-5m to permit expansion and contraction of the slabs and control crack location. They are formed by sawcutting 1/4-1/3 the pavement thickness after curing, forcing a crack to occur at the joint through the pavement thickness. Aggregate interlock arising from the interaction of the two rough joint surfaces is an important load transfer mechanism at contraction joints. Construction joints are formed at the end of a pour, and in contrast to contraction joints, have relatively smooth joint surfaces with no aggregate interlock load transfer.

Rigid pavements are complex structural systems. To design them efficiently, engineers need to evaluate the effects of critical load cases and predict the corresponding failure modes, evaluate pavement lifetimes, and develop better retrofit strategies for damaged pavements.

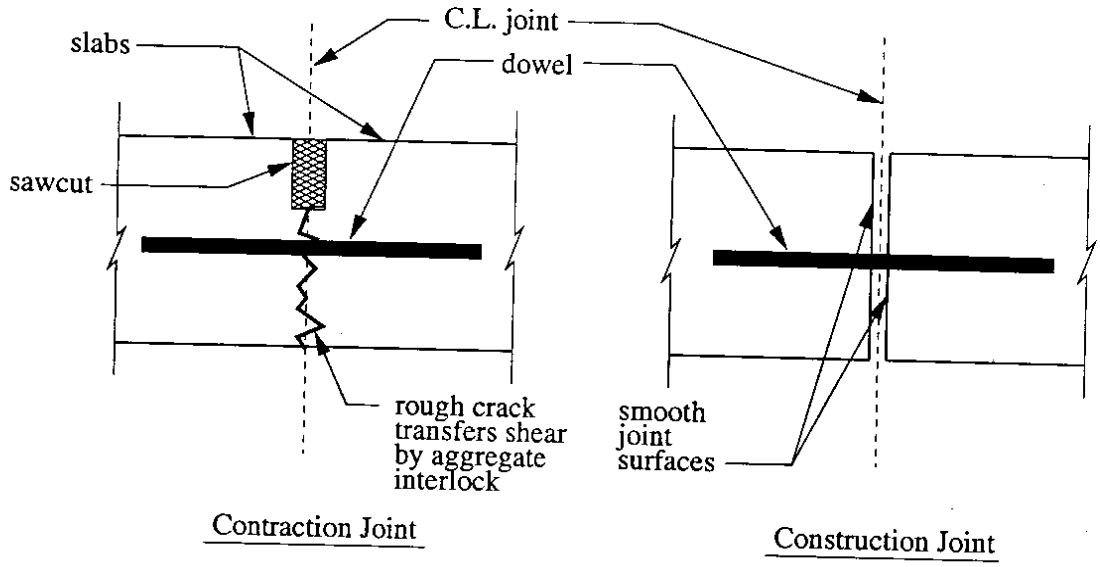

Figure 1.2: Typical Rigid Pavement Joints

methods commonly used to model joint response are simplistic, and do not accurately capture the complex behavior of aggregate interlock and dowel-slab interaction. This is of great concern, since serviceability failures of JPCP are often the result of poor joint performance. For example, faulting, where a permanent relative vertical displacement develops between adjacent slabs as shown in Fig. 1.1, is a common joint failure that is often attributed to poor joint shear transfer and localized degradation of the supporting soil. In addition to concerns about the modeling of joint shear transfer, solution of the three-dimensional (3D) finite element models needed to capture pavement response is not feasible on the desktop computers commonly available to designers.

1.2 Research Objectives

This study focuses on overcoming particular deficiencies in current state-of-the-art analysis of JPCP. In particular, this study focuses on the following topics:

- *Development of new techniques for modeling dowel load transfer.* These techniques permit the consideration of dowel looseness that is known to have a large effect on joint performance [10, 81], but has not been explicitly modeled in previous studies.

- *Investigation into new methods for modeling aggregate interlock shear transfer.* A modeling strategy is developed and implemented that rationally incorporates realistic crack constitutive relations that reflect variations in joint load transfer with joint

- Chapter 5 focuses on the mechanism of aggregate interlock and its inclusion in finite element models of rigid pavement systems. A detailed literature review is presented to explain the mechanics of aggregate interlock and provide an overview of past attempts to model this phenomenon. Based on this research and insight into the physical mechanism of aggregate interlock shear transfer, a modeling technique is developed that rigorously incorporates crack constitutive relations at joints.

- Chapter 6 addresses solution strategies, including the development and implementation of a nonlinear solution scheme appropriate for use with large-scale models incorporating material and contact nonlinearities. A multigrid-preconditioned conjugate gradient solver applicable to unstructured 3D finite element discretizations is developed to solve the linearized systems of equations arising at each iteration in the nonlinear solution. In addition to extensive performance studies, a model problem of a rigid pavement system is solved to illustrate the use of the solution strategy in the context of the present study.

- Chapter 7 examines the accuracy of the finite element models developed in this study by comparison with laboratory test data collected by Hammons [33]. The test data include scale models of doweled two-slab systems both with and without cement-treated base layers.

- Chapter 8 presents parametric studies designed to indicate the usefulness of the proposed joint shear transfer modeling strategies for pavement evaluation and design. The effect of dowel looseness on joint shear transfer efficiency and pavement response, including slab and subgrade stresses, is addressed. The effect of joint opening on aggregate interlock shear transfer efficiency is also examined in detail. Both wheel and temperature loadings are considered in these studies.

- Chapter 9 presents a summary of this study, along with conclusions and recommendations for future research.

measured during the Arlington Road Test [87, 88, 89].

Following the development of these early models, Tabatabaie and Barenberg [82, 84] developed a more general finite element program called ILLI-SLAB which is still in use today. ILLI-SLAB utilizes the same medium-thick plate elements employed in earlier models, and the effect of a bonded or unbonded base can be incorporated using a second layer of plate elements below the slab. The subgrade is modeled as a Winkler foundation. Dowel bars at joints are modeled as discrete bar elements, and shear transfer via aggregate interlock or keyway is modeled with spring elements. Further, the relative displacement between dowel bars and the concrete pavement can be considered by placing a discrete spring element at each end of the dowel bar. Verification of models developed with ILLI-SLAB was achieved by comparison with theoretical solutions for stresses and displacements, as well as comparison with actual field test data from the AASHO Road Tests [1] and tests of concrete pavement on cement treated subbases. Studies were performed to examine the effects of load transfer efficiency on the behavior of plain jointed concrete pavement as well as the effect of transverse crack spacing on load stresses in continuously reinforced concrete pavement. Further, increased support provided by a tied concrete shoulder was examined, as was the the effect of a stabilized base when modeled as a discrete stiff layer. One of the main conclusions from the early studies using ILLI-SLAB was that joint load transfer efficiency must be modeled accurately to predict the possibility of permanent subgrade deformation and slab distress near the slab corners.

Tayabji et al. [86] developed the program JSLAB for analyzing pavements resting on a Winkler foundation. The model incorporates features similar to ILLI-SLAB, utilizing plate elements to model the slab and a bonded or unbonded base. Dowels were modeled with modified beam elements that incorporated the effect of shear deformation and the elastic support provided by the concrete. As in ILLI-SLAB, aggregate interlock and keyways were modeled with springs.

In 1983, Huang [38] extended his earlier model to allow the consideration of multiple slabs and various load transfer devices in a manner similar to ILLI-SLAB. It should be noted that dowels were modeled as having shear stiffness only across the joint, i.e. bending deformations of the dowels were not considered. The deformation of the concrete under the dowel was considered by treating the embedded portion of the dowel as an infinitely long beam on elastic foundation. The subgrade was modeled as an elastic half-space and loss of contact between the subgrade and the slab was considered. Comparisons between the

2.2 Current FE Models of Rigid Pavement Systems

2.2.1 Ioannides and Donnelly (1988)

This study [43] was an early attempt to model a single rigid concrete pavement slab and subgrade using a 3D finite element model. The focus of the study was the effect of subgrade nonlinearity on pavement response. The effects of mesh refinement, vertical and lateral subgrade extent, and boundary conditions on the predicted response were also examined.

The existing 3D finite element program GEOSYS was adopted for the analysis. Linear, 8-noded brick elements were used to model the slab and subgrade, with varying degrees of mesh refinement. The effects of lateral and vertical subgrade extent were examined, with the investigators concluding that the subgrade depth should extend to the point where constant strain is reached. This depth varies depending on the lateral extent of the subgrade, but was generally about 40' for a lateral subgrade extent of between 25' and 35'. The boundary conditions used in the study were vertical supports on the bottom of the subgrade, and lateral restraints on the vertical sides of the subgrade.

Vertical mesh gradation studies showed that sufficient accuracy was achieved when the slab was divided into two layers. Horizontal mesh gradation and element aspect ratio were also studied, resulting in the conclusion that the mesh needs to be refined in the region of loading, and the maximum element aspect ratio should be kept below four.

Interior, edge, and corner wheel loadings were applied and the results compared with analytical solutions and 2D analyses reported previously by Ioannides et al. [42]. To accentuate the effects of subgrade nonlinearity, the foundation material assumed was a relatively soft cohesive material, and the wheel loads used were fairly large. The interior loading produced little subgrade nonlinearity. Comparison with the 2D results and analytical solutions showed some discrepancy in the deflections and stresses which the authors attributed to mesh refinement in the region of the load. The edge loading produced more pronounced subgrade nonlinearity, but the overall response of the slab was not significantly affected, with the upper 2.0 m of the foundation exhibiting significant nonlinear response. Comparison with 2D solutions showed relatively good agreement for slab deflections, with the discrepancies in slab stresses being somewhat larger. The differences in subgrade stresses were quite significant. In the case of corner loading, the effects of subgrade nonlinearity were more significant, with about 20% of the elements experiencing reduced moduli, with these elements concentrated in the upper 1.7 m of the subgrade. Comparison with the ILLI-SLAB 2D solutions for stresses and displacements showed discrepancies of less than

efficiency due to fatigue.

Various loadings were considered, including wheel loads, nighttime curling (cooling of the top of the slab relative to its base), and daytime curling (heating of the top of the slab relative to its base). The main conclusions of the study were as follows:

- Dowel-concrete interface stiffness is reduced due to high stress concentrations near the dowel. This loss of stiffness increases with repeated loadings due to fatigue, reducing shear transfer efficiency.
- The dowel-concrete interface stiffness significantly affects deflection profiles for slabs with normal subgrade support.
- The shear transfer efficiency increases with loss of subgrade support near the joint due to pumping action.
- Nighttime curling causes a loss of support near the joints, as well as widening of the joint. Truck traffic is typically heaviest at night, so nighttime curling in combination with wheel loading is a critical load case.
- During nighttime curling and the resulting loss of support at the joint, the far end of a slab lifts off the base as heavy wheel loads pass. This may help explain joint faulting.
- Daytime curling is not a critical loading, since the slab lifts off the subgrade at its center as opposed to the joints.

2.2.3 Zaghloul, White, and Kuczek (1994)

This study [96] focused on the determination of load equivalence factors (LEFs) by the use of a 3D, nonlinear dynamic finite element model developed using the commercially available finite element program ABAQUS. The model was designed to overcome the inherent limitations of 2D plate finite element models and Westergaard analysis.

The slab and subgrade were modeled using 3D brick elements, and the dowels were explicitly modeled with bar elements that were unbonded over half their length. Joints were modeled with gap elements, and assumed to have an initial opening of 3/8 inch; contact friction was considered if the gap closed during loading.

Concrete, granular subgrade, and clay subgrade materials were all modeled as different nonlinear materials. The concrete was modeled as bilinearly elastic-plastic up until failure, at which point the stress-strain curve descended bilinearly. The granular base, subbase, and

verified by comparing the results to an approximate solution for a point load on a infinite plate by a Winkler foundation, and to the exact solution for a transient point load on a beam of finite length supported by a viscoelastic Winkler foundation. Good agreement was found in both cases. In addition, results from a U.S. Army Corps of Engineers study were compared to those computed using DYNA-SLAB, with good agreement. Further, the foundation models were verified by comparing computed deflection profiles due to harmonic loadings to those determined using a separate 3D soil-structure interaction program. In general, the layered foundation gave good results for all loading conditions, whereas the Winkler foundation model was in good agreement for interior deflections, but overpredicted edge deflections.

Following verification of the model, the authors investigated whether dynamic analysis is necessary for the prediction of rigid pavement response. Parameters included vehicle velocity and pavement roughness, and several different slab thicknesses and load transfer efficiencies were considered. The effect of vehicle velocity on slab bending stress was found to be negligible in all cases. To study the effect of pavement roughness, equivalent loads were developed for various slab profiles that included the effects of curling, faulting, and breaks of varying severity using a separate truck simulation program.

The authors concluded that while it is important to use expected pavement roughness to determine the peak magnitudes and locations for the truck wheel load history, the dynamic effects on the slab response are not significant. The authors caution, however, that the existence of a stiff layer or bedrock at a shallow depth may increase dynamic effects to the point that they should be incorporated in the analysis.

2.2.5 Uddin, Hackett, Joseph, Pan, and Crawley (1995)

This study [90] documented the development of a 3D finite element model of a concrete pavement and subgrade using the general-purpose finite element program ABAQUS. The goal of the study was to examine the effect of pavement discontinuities on surface deflections of a pavement subjected to a standard falling weight deflectometer load (FWD).

The slab, cement-treated base, and subgrade were modeled using 3D elastic brick elements. The following model parameters were investigated in a previous study and employed:

- The model was quarter symmetric with rollers on the lateral sides of the subgrade. One and one-half pavement slabs were modeled.

- The subgrade was modeled well beyond the edge of the pavement slab and shoulder.

(20-noded) brick elements was used to model the slab.

The subgrade was modeled as a dense liquid (Winkler) foundation. Interface friction between the slab and subgrade was modeled using a membrane element coupled with a special interface element designed to model contact and frictional movement. The membrane element was required to provide compatibility between the interface element and a dense liquid foundation. An additional layer of 3D elements between the slab and subgrade.was used to model cement-treated bases.

The dowel bars were modeled as discrete beam elements that were allowed to slip relative to the slab. No attempt was made to model the interaction between the dowel bars and the concrete. Aggregate interlock shear transfer across transverse joints was modeled using spring elements.

Model verification was achieved by comparison with full-scale field test data, specifically the AASHO Road Tests [1], PCA tests on cement-treated bases [14], and the Arlington Road Test [87]. In general, the comparisons between the 3D model and the test results was good. The ability of the model to predict crack initiation locations was verified by comparing the principal stress contours generated by ABAQUS with the actual observed crack locations for various slab thicknesses and loading conditions consistent with the AASHO road tests. The PCA tests on cement-treated bases provided load-deflection data for interior and free edge loading conditions. In general, the model accurately predicted deflections, whereas the conventional 2D plate models and Westergaard's solutions gave less accurate results. Comparison of computed curling stresses with data obtained from the Arlington road test showed good agreement.

2.2.7 Zaman and Alvappillai (1995)

This study [97] examined the effect of moving aircraft loads on systems of multiple, jointed rigid pavement slabs. The pavement slabs were modeled using 4-noded, rectangular, thin plate elements, and the underlying soil was considered a viscoelastic Winkler foundation. The dynamic interaction of the aircraft and the slab system was incorporated in the analysis, with each landing gear modeled as a parallel spring and dashpot with an associated mass.

The longitudinal joints were considered to be keyed or cracked, and were modeled as discrete displacement springs. The transverse joints were modeled as doweled, and debonding and gaps between the dowels and pavement were considered explicitly; this study represents the first attempt to rigorously consider this contact nonlinearity. The constraint conditions between the dowels and the pavement were:

Both linear and nonlinear temperature gradients through the thickness of the slab and uniform temperature changes were considered. Using a model consisting of four slabs and two concrete shoulders with three elements through their thickness, parametric studies were performed to examine the effects of friction, slab lengths and thickness on curling and thermal expansion stresses. The effect of temperature variation on joint openings was also examined. Comparisons were made between the model results and those from similar analyses employing common 2D finite element codes, including ILLI-SLAB and JSLAB. Nonlinear temperature gradients were modeled with a single slab model having nine elements through its thickness. The slab stresses determined from the linear and nonlinear temperature variations were compared.

The main conclusions of the study were as follows:

- Reasonable agreement for maximum curling stresses was found between the model and previous analyses performed using 2D FE models.
- The maximum temperature curling stresses for the entire range of linear temperature gradient analyses were about 28% of the modulus of rupture of concrete.
- The effect of friction on curling stresses was determined to be negligible; slab length had a moderate effect, and increasing the slab thickness markedly increased curling stresses.
- Thermal expansion stresses were found to be significantly smaller than those predicted by subgrade drag theory, although they increased with friction and slab length.
- Nonlinear temperature distributions caused higher slab tensile stresses than linear temperature distributions in general.
- The joint openings predicted by the finite element models due to uniform temperature changes were in general less than those predicted using common design equations.

2.2.9 Kim, Hjelmstad, and Zuo (1997)

This study examined the response of a single rigid pavement slab to the heavy multiple-wheel loading of typical aircraft landing gear [49]. Three dimensional finite element analyses were performed using radially graded meshes and infinite elements to represent the vertical and lateral extents of the natural soils in an attempt to minimize the number of unknowns

jected to edge loading by either a single wheel, Boeing 777 landing gear, or 727 landing gear were performed. Each wheel in the landing gear was modeled explicitly, with mesh refinement done in the region of the load. The model degrees of freedom varied from about 81,000 to 92,000 depending on the load case. The stress results from the finite element analyses were compared with theoretical solutions for a slab on elastic foundation; significant differences in the two solutions were observed for most combinations of loading and subgrade type. To analyze the effect of the stabilized base layer on stress response, further runs were computed for the Boeing 777 landing gear assuming that the stabilized base layer was either continuous or cracked at the joint. It was found that a cracked base layer results in significantly higher slab stresses than an uncracked layer; stress load transfer efficiency is also reduced by cracking of the base layer.

2.3 Summary of Previous Work

Clearly, significant progress has been made in the finite element modeling of rigid pavement slabs. The original, 2D plate models developed in the early 1970's [80, 37] have evolved into 2D finite element packages designed specifically for the modeling of rigid pavement systems [82, 86]. Subsequently, these tools have been extended to allow research into the response of rigid pavements to applied static and dynamic loading (see [42, 44, 97] for example).

At present, it is generally accepted that 3D modeling techniques are necessary to accurately capture the response of rigid pavement systems. Large 3D models are commonly used by researchers to study the dynamic response of rigid pavement systems [96, 13, 90]; the effect of material nonlinearities [12]; for comparison with field test data [54]; and to identify critical loading conditions [12, 49]. Table 2.1 summarizes the salient features of the 3D finite element studies reviewed in this Chapter.

Despite the large number of analytical studies on the structural response of jointed concrete pavements, some significant aspects of the problem have been neglected. Specifically:

- As seen in Table 2.1, modeling of the dowels has been accomplished by explicitly meshing beam elements with the slab in previous 3D finite element investigations. Beyond permitting dowel slip, dowel-slab interaction has not been considered except by Channakeshava et al. [12], where a separate analysis of a single dowel and localized slab region was performed to compute a nonlinear spring stiffness to place between the dowel and the slab in the larger finite element model. Similarly, most 2D models

secant stiffness, valid only for one geometric configuration, set of material properties, and loading. No recent study has addressed the rational determination of load transfer across pavement joints due to aggregate interlock under a variety of loadings, geometries, and joint openings.

- Previous 3D models have been used only in research applications due to computational requirements; realistic, practical solutions of 3D models in design settings are not feasible at present. This is due partially to the efficiency of the solution routines in available finite element programs for the 3D finite element modeling of structural systems.

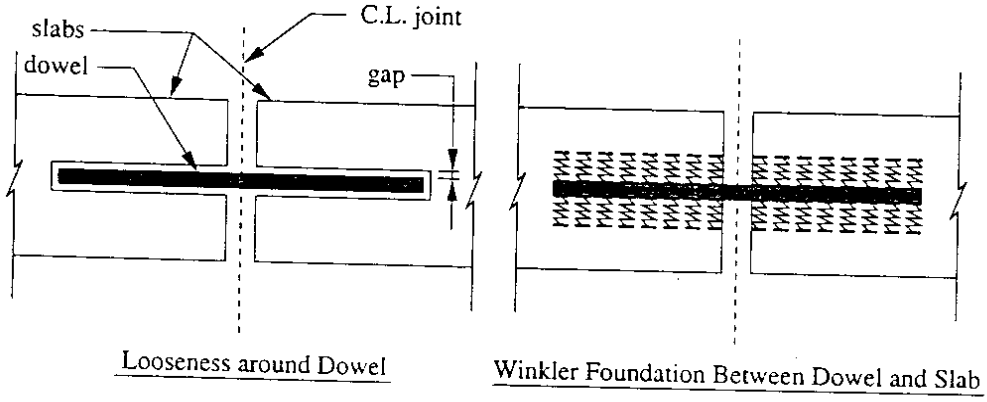

Figure 2.1: Dowel Looseness and Winkler Foundation Around Dowel

These three specific shortcomings of previous investigations are the main research topics of this study. The first two items are of particular importance in the design of rigid pavements, since many failures and shortened pavement lives can be attributed to joint problems caused at least in part by inadequate load transfer. Indeed, many undoweled concrete pavements are commonly retrofitted with dowels in an attempt to lengthen their service life and improve performance [32, 81]. Further, one significant 3D finite element study reviewed in Chapter 2 notes that poor joint load transfer has predictable detrimental effects on pavement behavior [12].

Addressing the third issue is of broad importance, as large, 3D models of any structural system require tremendous computer resources to achieve a reliable solution. Several of the models cited in this literature review employed relatively coarse meshes [12, 54] because of computational limitations. More efficient solution strategies will ease the problem of mesh refinement, as well as making the proposed joint modeling techniques accessible to more pavement researchers and designers to aid in their investigations.

- Loss of contact between the slab and subgrade due to temperature and wheel loading. This can lead to critical loadings as noted in Channakeshava et al. [12].

The remainder of this Chapter addresses these issues.

3.2 Modeling Issues

3.2.1 Dynamic vs. Static Modeling

The literature review in Chapter 2 indicates that several researchers have begun to use dynamic models of rigid pavement systems. However, only static models are employed in the present investigation. This restriction does not represent a severe limitation, and is justifiable for several reasons:

- The development and implementation of new joint shear modeling strategies should first be accomplished with static models that will allow detailed evaluation of their performance and applicability.

- Rigid pavement systems are typically designed assuming static equivalent single axle loads (ESALs) which attempt to account for damage and fatigue due to mixed traffic over the expected lifetime of the structure. The proposed models are not limited to any one type of axle or load magnitude, and any axle loading corresponding to an actual truck or appropriate design axle may be applied.

- One recent study has shown that the dynamic response of the slab may not be significant, and as long as the dynamic interaction between the slab and truck are accounted for in developing the effective wheel loads, static models are reasonably accurate [13]. Such wheel load histories may be generated with an independent model that incorporates the pavement profiles, and the stiffness and damping properties of the truck suspension, or via actual field data.

- The computational requirements of large, 3D dynamic models are significant. At present, implicit time stepping methods are far too computationally expensive for the proposed models, since they require solution of the system of equations arising from the system discretization at each time step. While less expensive explicit methods are available, the stability limitations of these methods can make them computationally inefficient as well.

3.2.3 Modeling of the Base Layers and Subgrade

Finite element models of rigid pavement systems consisting of one or more slabs require a reasonable representation of the subgrade. Several researchers have used continuum models for the entire subgrade [43, 96, 90]; however, this dictates that the subgrade be modeled to a depth where constant vertical strain exists, which may be quite large. This is often done in spite of the fact that the subgrade stresses decrease quite quickly with depth [43] to a point where a continuum model may not be required, unnecessarily increasing the size of the model. Another approach to modeling the subgrade is to use a dense liquid (Winkler) foundation directly below the slab or treated base layer to model the infinite vertical extent of the subgrade [54, 12]. While this greatly reduces computational complexity, it may not accurately model foundation response due to the lack of shear coupling between the discrete foundation springs generated with the dense liquid foundation model.

In the present study, the foundation model varies depending on the system being studied. In general, any number of linearly elastic base/soil layers can be modeled to any depth below the slab. Below the bottom-most layer, a Winkler foundation is used recognizing that foundation stresses at this depth are low and the use of a simplified model will have little effect on the slab response. The base layers can be extended laterally to account for extended shoulders if required as shown for a two-slab system in Fig. 3.1. Note that modeling the soil as linearly elastic is not entirely realistic. However, while nonlinear response of the subgrade is likely under heave axle loads, subgrade yielding may not greatly affect computed slab displacements and stresses [43]. The development of 3D constitutive relations for soils appropriate for use in the modeling of rigid pavements is an active area of research [35]. As better, more reliable models become available, they may be included in future analyses.

3.2.4 Discretization of the Slab and Subgrade

The regular geometry of the system to be modeled lends itself to hexahedral elements. Quadratic elements, while somewhat more difficult to implement than simpler linear elements, have excellent convergence rates and are more robust. Further, other researchers have explicitly demonstrated the applicability of quadratic hexahedra for modeling rigid pavement systems [54]. For these reasons, 20-noded quadratic hexahedra are used to model both the slab and the subgrade. An isoparametric element formulation is used to permit complex geometries such as skewed joints to be rigorously considered; the element stiffness matrices are computed using $3 \times 3 \times 3$ Gaussian integration. See Zienkiewicz and Taylor [98]

[98]:

$$\mathbf{p} = \sum_{i=1}^{l} \int_{A_i} \mathbf{N}_i^{\mathbf{T}} \mathbf{f} dA_i \tag{3.1}$$

In Eq. 3.1, Σ represents assembly and summation.

Evaluation of Eq. 3.1 may be accomplished using a rectangular rule where the wheel load is represented by n small point loads, each equal to the pressure acting over the area $\Delta A = \Delta x \Delta y$ as shown in Fig. 3.2. The evaluation of Eq. 3.1 is then reduced to:

$$\mathbf{p} \approx \sum_{j=1}^{n} \mathbf{N}_{ij}^{\mathbf{T}} \mathbf{f}_j \Delta A \tag{3.2}$$

where the subscript i has been retained as a reminder that for each ΔA, the element it lies within must be determined, and $\mathbf{N}_{ij}$ is the usual matrix of shape functions for the i^{th} element evaluated at the the j^{th} point. Again, Σ implies both assembly and summation.

Determination of the i^{th} element within which the j^{th} point lies is accomplished with an efficient grid searching algorithm developed for use with the multigrid solution strategies. The grid search relies on grouping all elements in the finite element mesh according to their location in the model, greatly reducing the number of elements that must be searched to determine which element any (x, y, z) point lies within. Calculation of the local element coordinates corresponding to the j^{th} point is done using Newton's method at the element level. Details may be found in Chapter 6 and Appendix A.

It should be noted that another approach to the evaluation of 3.1 would be to determine which elements are fully loaded, integrate that portion of Eq. 3.1 by conventional integrations over entire element faces, and approximately evaluate the remainder of the integral over the partially loaded elements. This approach was recently outlined by other researchers in [34].

Temperature and Self-Weight Loading

Temperature gradients through the thickness of the slab are treated as general prestrains on an element-by-element basis [98]. This allows an exact mathematical treatment of linear variations in temperature through each element, as the 20-noded brick captures linear variations in strain. Note that a model with multiple elements through the slab thickness allows the approximation of a nonlinear temperature gradient as a piecewise linear function. While nonlinear temperature gradients are not considered in this study, several researchers have noted their occurrence [60], and the ability to model this phenomenon may prove useful in future studies.

openings.

The implementation of nodal contact modeling within a finite element model introduces inequality constraints, requiring a complex solution strategy. The complexity is heightened by the use of iterative solvers, as will be employed in this study. Details of the implementation are thus deferred until Chapter 6, where a comprehensive treatment of the nonlinear solution strategies employed in this study is presented.

Ideally the slab boundary conditions would include the effect of friction between the slab and subgrade. However, for the purposes of joint shear transfer modeling, simple displacement boundary conditions are sufficient. The appropriate boundary conditions are the minimum required to keep the model stable, i.e. prevent transverse displacements and rotation about the vertical axis. The models developed in this study use a single (x, y) displacement restraint on one side of each slab and a single x direction displacement constraint on the other side. The same constraints are applied to the base layers and subgrade as a unit; friction between the slab and base is not considered in the analyses.

3.3 Summary

The need for better finite element modeling of dowel and aggregate interlock joint shear transfer and more efficient solution strategies has been identified. Addressing these issues requires the development of specific finite element techniques appropriate for the modeling of rigid pavement systems. This Chapter has covered modeling of the slab and subgrade, incorporation of boundary conditions, slab-subgrade loss of contact, and methods for applying both temperature and wheel loadings. The next three Chapters focus individually on dowel joint shear transfer, aggregate interlock shear transfer, and nonlinear solution strategies.

More recent dowel models have also been proposed which more rigorously incorporate the effect of dowel-slab interaction in addition to the beam deformation of the dowel between adjacent slabs; a detailed description of the formulations and limitations of the more recent models is given by Guo [31]. Guo developed a component dowel bar model that consistently incorporates a Winkler foundation model for embedded portions of finite length and a discrete shear beam element spanning the joint into a single element.

Of course, the Winkler foundation modulus can be reduced to account for gaps between the dowel and the slab. While this is computationally attractive, it is not always clear what modulus to use to model the interaction of the slab and the dowel. Similar models that reduce the Winkler modulus nonlinearly in a more rational manner, such the approach developed by Sittipunt [79] for the modeling of reinforcement at the base of concrete shear walls, require the determination of several parameters in addition to the spring stiffness which may not be readily determined.

As noted in Chapter 2, 3D finite element models generally employ beam elements meshed explicitly with the solid elements comprising the pavement slab and do not attempt to model dowel-slab interaction. An approach designed to remove the difficulty of meshing beam elements with plate or solid elements was developed by Ioannides and Korovesis [45], where a uniform joint shear stiffness is used to replace the individual dowels. This approach was employed by Hammons [33] in the development of 3D finite element models of scale model laboratory tests on doweled pavements. Implicit in the derivation of the joint stiffness, however, is the common assumption that the embedded portion of the dowel may be represented as a beam with a Winkler foundation sandwiched between it and the surrounding concrete. Again, the difficulty lies in determining an appropriate modulus of reaction for the Winkler foundation that properly accounts for both dowel/slab interaction and any dowel looseness that may exist. This model also assumes uniformly spaced dowels along the joint, which is common for newly constructed pavements but rarely the case for retrofitted joints where dowels are often located only in the wheelpaths. No 3D finite element models have explicitly considered the effect of dowel looseness on joint performance.

In this Chapter, a new technique for modeling dowel load transfer is proposed and developed which relies on an embedded formulation of the dowel, and allows the explicit and rigorous consideration of gaps between the dowel and the slab through nodal contact modeling. The necessary details for the inclusion of a general bond-slip law are also presented, as the dowel element has potential application in the modeling of many reinforced concrete

ing axial-only reinforcement in finite element models of reinforced-concrete structures have been employed by several researchers [21, 95, 78]. However, these formulations typically require special integration techniques to compute the stiffness matrices of elements containing embedded reinforcing members.

Clearly, it is desirable to use an embedded formulation for the dowel elements similar to that developed for axial-only reinforcing, allowing the meshing of the slabs to be independent of the dowel locations. One of the major goals of this study is the development of a general formulation for an arbitrarily oriented, embedded, quadratic bending element. Provisions are made for axial debonding of the dowel, which is typical in rigid pavement slabs. Further, the formulation is extended to model gaps between the dowel and the surrounding slab which occur due to damage of the slab concrete under repeated loading. To model the portion of the dowel between the two slabs, a conventional two-noded shear beam is used that is constrained at its ends to displace compatibly with the elements it spans between.

The remainder of this Chapter is dedicated to the presentation of the dowel modeling techniques employed in this study. A brief description of the dowel element is presented in Section 4.3. In Section 4.4, the stiffness matrix of the embedded dowel is developed for three specific conditions: perfectly bonded and transversely constrained, debonded and transversely constrained, and debonded with gaps between the embedding element and the dowel. Section 4.5 examines how the dowel element could be extended to include a general bond-slip law in lieu of an explicit consideration of dowel looseness. This is followed in Section 4.6 by the development of the stiffness matrix of a shear beam element spanning the joint and compatible with the elements on either side of the joint. Section 4.7 details the constraint updating strategy required when dowel looseness is considered. Verification of the element formulation is achieved with a simple model problem in Section 4.8. Section 4.9 summarizes the dowel modeling techniques developed in this Chapter.

4.3 The Quadratic Beam Element

4.3.1 Element Definition

Higher order shear and bending elements have been in use for many years [40, 6], with more recent applications focusing on the modeling of curved structures [48]. Initially, the use of these elements was limited by their tendency to "lock", or fail to converge with increasing levels of mesh refinement. An excellent explanation of this phenomenon and proposed solutions are given by Prathap and Bhashyam [72]. It is demonstrated that the

torsional rotation, and bending rotations can be written as:

$$SE_{du} = \frac{1}{2}\int_0^l EA\left(\frac{du}{ds}\right)^2 ds \tag{4.3}$$

$$SE_{dv} = \frac{1}{2}\int_0^l GA_v\left(\theta_w - \frac{dv}{ds}\right)^2 ds \tag{4.4}$$

$$SE_{dw} = \frac{1}{2}\int_0^l GA_w\left(\theta_v + \frac{dw}{ds}\right)^2 ds \tag{4.5}$$

$$SE_{tu} = \frac{1}{2}\int_0^l GJ(\theta_u)^2 ds \tag{4.6}$$

$$SE_{bv} = \frac{1}{2}\int_0^l EI_v\left(\frac{d\theta_v}{ds}\right)^2 ds \tag{4.7}$$

$$SE_{bw} = \frac{1}{2}\int_0^l EI_w\left(\frac{d\theta_w}{ds}\right)^2 ds \tag{4.8}$$

Evaluation of these integrals is most easily performed with respect to the dowel local coordinate, η. Referring to Fig. 4.2, we may write an incremental vector along the bar, $\mathbf{ds}$, as:

$$\mathbf{ds} = dx\mathbf{i} + dy\mathbf{j} + dz\mathbf{k} = \frac{dx}{d\eta}d\eta\mathbf{i} + \frac{dy}{d\eta}d\eta\mathbf{j} + \frac{dz}{d\eta}d\eta\mathbf{k} \tag{4.9}$$

where $(\mathbf{i}, \mathbf{j}, \mathbf{k})$ refer to the usual unit vectors in the global coordinate system. The incremental distance along the bar is then computed as:

$$ds = \sqrt{\left(\frac{dx}{d\eta}\right)^2 + \left(\frac{dy}{d\eta}\right)^2 + \left(\frac{dz}{d\eta}\right)^2}\, d\eta = h d\eta \tag{4.10}$$

Using Eqs. 4.1 to 4.2, the required derivatives of the global coordinates with respect to the dowel local coordinate may be computed as:

$$\begin{bmatrix} \frac{dx}{d\eta} \\ \frac{dy}{d\eta} \\ \frac{dz}{d\eta} \end{bmatrix} = \begin{bmatrix} x_1 & x_2 & x_3 \\ y_1 & y_2 & y_3 \\ z_1 & z_2 & z_3 \end{bmatrix} \begin{bmatrix} \frac{dN_1}{d\eta} \\ \frac{dN_2}{d\eta} \\ \frac{dN_3}{d\eta} \end{bmatrix} \tag{4.11}$$

Note that for a straight bar with a centrally located third node, the value of h is constant and equal to half the length of the dowel.

The vector of nodal displacements and rotations may be written as:

$$\mathbf{U}^d = \begin{bmatrix} \mathbf{d}_1 & \Theta_1 & \mathbf{d}_2 & \Theta_2 & \mathbf{d}_3 & \Theta_3 \end{bmatrix}^{\mathbf{T}} \tag{4.12}$$

where $\mathbf{d}_i$ and Θ_i refer to generalized nodal displacement and rotation vectors; the superscript $\mathbf{T}$ denotes a transpose. Using the displacement and rotation basis functions developed in the previous section, the generalized displacement and rotation vectors at any point may

$$SE_{bv} = \frac{1}{2}\mathbf{U}^{d\mathbf{T}}\left[\int_{-1}^{1}\frac{EI_v}{h}\left(\frac{d\mathbf{\Phi}^{\mathbf{T}}}{d\eta}\right)\left(\frac{d\mathbf{\Phi}}{d\eta}\right)d\eta\,(\mathbf{s}\otimes\mathbf{s})\right]\mathbf{U}^{d} \tag{4.31}$$

$$SE_{bw} = \frac{1}{2}\mathbf{U}^{d\mathbf{T}}\left[\int_{-1}^{1}\frac{EI_w}{h}\left(\frac{d\mathbf{\Phi}^{\mathbf{T}}}{d\eta}\right)\left(\frac{d\mathbf{\Phi}}{d\eta}\right)d\eta\,(\mathbf{t}\otimes\mathbf{t})\right]\mathbf{U}^{d} \tag{4.32}$$

Taking the first variation of the strain energy with respect to $\mathbf{U}^d$ gives the total dowel stiffness matrix, $\mathbf{K}^d$, as the sum of the symmetric bracketed expressions and the symmetric part of the unsymmetric bracketed expressions. The integrals are computed numerically using two-point Gaussian quadrature, which is exact for a straight element.

4.4 Embedment of the Dowel

In this section, a procedure for embedding a dowel element within a solid, quadratic, isoparametric element is developed. In the following discussion, *bonding* will refer to axially constraining the dowel to the embedding element, and *constraining* will refer to the constraint of transverse dowel displacements to the embedding element. Three types of embedment are considered: (1) the case of a bonded, constrained embedded dowel is developed first to illustrate the embedding procedure; (2) the case of a debonded, constrained dowel, which has great practical applicability to the doweled systems being studied is then presented; and (3) the geometrically nonlinear case where gaps exists between the dowel and the embedding element is developed. Embedding the dowel requires that the locations of the dowel nodes in terms of the embedding element local coordinates be known. Procedures for determining the element local coordinates (ξ, η, ζ) from the nodal (x, y, z) coordinates using Newton's method are presented in [21] and [5]; a similar technique is used in this study. Details of the implementation may be found in Appendix A.

4.4.1 The Bonded, Constrained Case

Constraining the i^{th} node of a bonded dowel to an embedding element requires that the dowel nodal displacements be identical to the corresponding displacements of the embedding element at the node. Using the embedding element basis functions and nodal displacements, the i^{th} node of an unbonded dowel can be constrained to an embedding element in the following manner:

$$\mathbf{d}_i = \mathbf{N}_i^e\mathbf{U}^e \tag{4.33}$$

where $\mathbf{U}^e$ is the vector of nodal displacements of the embedding element, and $\mathbf{N}_i^e$ is the array of embedding element basis functions evaluated at the i^{th} dowel node.

the fact that the dowel has lost its independent nodal displacement degrees of freedom. In the actual implementation of the element, these zero rows and columns can be retained, and values of one placed on the diagonal to avoid singularity. The dowel nodal displacements are then computed as zero during the solution of the system stiffness equations. Alternatively, the rows and columns of $\mathbf{K}^{de}$ that consist entirely of zeros can be eliminated, resulting in a reduced number of degrees of freedom for the debonded, constrained dowel. The dowel nodal displacements can of course be recovered using Eq. 4.35.

4.4.2 The Debonded, Constrained Case

The development of this case follows in the same manner as the previously presented bonded, constrained case. The i^{th} node of an unbonded dowel can be constrained to an embedding element in the following manner:

$$\mathbf{d}_i \cdot \mathbf{q} = \mathbf{d}_i \cdot \mathbf{q} \tag{4.42}$$

$$\mathbf{d}_i \cdot \mathbf{s} = (\mathbf{N}_i^e \mathbf{U}^e) \cdot \mathbf{s} \tag{4.43}$$

$$\mathbf{d}_i \cdot \mathbf{t} = (\mathbf{N}_i^e \mathbf{U}^e) \cdot \mathbf{t} \tag{4.44}$$

Physically, at a debonded node the dowel retains its independent axial degree of freedom, but displaces compatibly with the embedding element in any transverse direction. The displacement vector at the i^{th} dowel node can then be expressed as:

$$\mathbf{d}_i = (\mathbf{q} \otimes \mathbf{q})\, \mathbf{d}_i + (\mathbf{s} \otimes \mathbf{s} + \mathbf{t} \otimes \mathbf{t})\, (\mathbf{N}_i^e \mathbf{U}^e) \tag{4.45}$$

The transformation matrix, $\mathbf{T}$ is still defined by Eq. 4.36, but $\mathbf{a}_i$ and $\mathbf{b}_i$ are now given by:

$$\mathbf{a}_i = \mathbf{q} \otimes \mathbf{q} \tag{4.46}$$

$$\mathbf{b}_i = \mathbf{s} \otimes \mathbf{s} + \mathbf{t} \otimes \mathbf{t} \tag{4.47}$$

As in the bonded case, the unembedded dowel element stiffness matrix and nodal force vector can be transformed according to Eqs. 4.40 and 4.41. Note that the only difference between the debonded and bonded cases lies in the definition of the submatrices $\mathbf{a}_i$ and $\mathbf{b}_i$. Also note that no consideration has been given to friction between the dowel and the embedding element.

4.4.3 The Debonded Case with a Gap

The inclusion of a gap, γ, between the dowel element and the surrounding slab is of particular interest (see Fig. 4.3). Unlike the previously considered cases, this situation presents a

expressed as:

$$\mathbf{d}_i = \mathbf{a}_i \mathbf{d}_i + (\mathbf{N}_i^e \mathbf{U}^e \cdot \mathbf{s} + \gamma_i)\,\mathbf{s} + (\mathbf{t} \otimes \mathbf{t})\,(\mathbf{N}_i^e \mathbf{U}^e) \tag{4.48}$$

where $\mathbf{a}_i$ is given by Eq. 4.46. In Eq. 4.48, the term $\mathbf{a}_i \mathbf{d}_i$ is the axial displacement of the dowel, the term $(\mathbf{N}_i^e \mathbf{U}^e \cdot \mathbf{s} + \gamma_i)\,\mathbf{s}$ represents the displacement in the local $\mathbf{s}$ direction, and $(\mathbf{t} \otimes \mathbf{t})\,(\mathbf{N}_i^e \mathbf{U}^e)$ gives the displacement in the local $\mathbf{t}$ direction; the sum of the three is the dowel nodal displacement vector. Note that γ_i is a signed quantity: when the magnitude of the dowel transverse displacement exceeds that of the embedding element, γ_i is positive; otherwise, γ_i is negative.

Assuming that $\mathbf{N}_i^e \mathbf{U}^e$ has a component in the direction of $\mathbf{s}$ gives:

$$\mathbf{s} = \frac{\mathbf{N}_i^e \mathbf{U}^e\,(\mathbf{s} \otimes \mathbf{s})}{\|\mathbf{N}_i^e \mathbf{U}^e\,(\mathbf{s} \otimes \mathbf{s})\|} \tag{4.49}$$

If m_i is defined according to:

$$m_i = \|\mathbf{N}_i^e \mathbf{U}^e\,(\mathbf{s} \otimes \mathbf{s})\| \tag{4.50}$$

Substitution of Eqs. 4.49 and 4.50 into Eq. 4.48 gives:

$$\mathbf{d}_i = \mathbf{a}_i \mathbf{d}_i + \left(\left(1 + \frac{\gamma_i}{m_i}\right)(\mathbf{s} \otimes \mathbf{s}) + (\mathbf{t} \otimes \mathbf{t})\right) \mathbf{N}_i^e \mathbf{U}^e \tag{4.51}$$

This gives a new definition for the tensor, $\mathbf{b}_i$, at a constrained, debonded node with a gap of any magnitude:

$$\mathbf{b}_i = \left(\left(1 + \frac{\gamma_i}{m_i}\right)(\mathbf{s} \otimes \mathbf{s}) + (\mathbf{t} \otimes \mathbf{t})\right) \tag{4.52}$$

The tensor $\mathbf{b}_i$ reverts to its previous definition for the debonded, constrained case if $\gamma_i = 0$. The transformation matrix, $\mathbf{T}$, follows the same definition given by Eq. 4.36, and now encapsulates the contact nonlinearity. Several points must be noted, however:

1. $\mathbf{T}$ as defined by Eq. 4.36 when using Eq. 4.52 is valid only for transforming displacements. Nodal forces must be computed using $\mathbf{b}_i$ as defined by Eq. 4.47, and then applying Eq. 4.41.

2. The stiffness matrix of the embedded dowel is still computed according to Eq. 4.40. However, computation of a tangent stiffness, appropriate for use in a Newton iteration, requires that $\mathbf{b}_i$ be defined by Eq. 4.47.

Inclusion of the embedded dowel with gaps in a general nonlinear solution strategy requires that a constraint updating scheme be employed; this is the topic of Section 4.7.

where $\mathbf{Q}$ is a 3×3 matrix whose rows are the dowel element local unit vectors $\mathbf{q}$, $\mathbf{s}$, and $\mathbf{t}$.

The stiffness contribution due to bond-slip is formulated using virtual work principles. Writing the *incremental* internal virtual work, $d\Pi^e$, yields:

$$d\Pi^e = \int_l d\mathbf{f}' \cdot d\boldsymbol{\Delta}' dl \tag{4.60}$$

Using Eqs. 4.53, 4.54, and 4.59, and transforming the variable of integration to the local element coordinate, η, Eq. 4.60 can be written as:

$$d\Pi^e = d\mathbf{U}^{de\mathrm{T}} \left(\int_{-1}^{1} \mathbf{B}^{\mathrm{T}} \left(\mathbf{Q}^{\mathrm{T}} \mathbf{D} \mathbf{Q} \right) \mathbf{B} h d\eta \right) d\mathbf{U}^{de} \tag{4.61}$$

The stiffness contribution due to bond-slip, $\mathbf{K}^{db}$, is then given by:

$$\mathbf{K}^{db} = \int_{-1}^{1} \mathbf{B}^{\mathrm{T}} \left(\mathbf{Q}^{\mathrm{T}} \mathbf{D} \mathbf{Q} \right) \mathbf{B} h d\eta \tag{4.62}$$

which may be easily evaluated. The total dowel stiffness matrix, $\mathbf{K}^{dt}$ is then:

$$\mathbf{K}^{dt} = \mathbf{K}^{de} + \mathbf{K}^{db} \tag{4.63}$$

and is of size 78×78. Note again that in this case $\mathbf{K}^{de}$ has non-zero values only in the rows and columns pertaining to the dowel element's degrees of freedom, and only $\mathbf{K}^{d}$ need be calculated and added to the upper 18×18 portion of $\mathbf{K}^{db}$. The vector of nodal forces due to bond at the dowel-concrete interface, $\mathbf{F}^b$, is computed as:

$$\mathbf{F}^b = \int_{-1}^{1} \mathbf{B}^{\mathrm{T}} \mathbf{f} h d\eta \tag{4.64}$$

4.6 Shear Beam Spanning the Joint

Modeling the portion of the dowel spanning the joint can be achieved using a conventional shear beam [73]. To enforce displacement compatibility between the shear beam and the embedded dowels on either side of the joint, the end nodes of the shear beam must be constrained to the solid elements between which it spans. This is easily done in the same manner that the dowel element was constrained to an embedding element. Following the development of the matrix $\mathbf{T}$ given in Eq. 4.36 for the embedded dowel, we can specify the expanded vector of nodal displacements as:

$$\mathbf{U}^{be} = \left[\begin{array}{cccccc} \mathbf{d}_1 & \Theta_1 & \mathbf{d}_2 & \Theta_2 & \mathbf{U}_1^e & \mathbf{U}_2^e \end{array} \right]^{\mathrm{T}} \tag{4.65}$$

Physically, the inequality in (2) is false if $\mathbf{F}_i$ has a component opposite the direction of the transverse relative nodal displacement, i.e. the dowel is compressing the surrounding slab in the s direction at the point of contact.

The simplest constraint updating algorithm follows directly from this criteria for maintaining/releasing constraints. Based on the current displacements and constraints, the transverse nodal forces, $\mathbf{F}_i$, acting on the dowels are found. For currently unconstrained nodes, if the relative displacements exceed the gap, the node is constrained. The currently constrained i^{th} node is released if $\mathbf{F}_i$ does not oppose the relative displacement.

This simple node-by-node updating scheme can be improved upon, however. At the end of an iteration in the global solution scheme, the displaced shape of the model has just been incremented, and is fixed while constraints are checked. We can treat all quadratic dowel and cubic beam elements as a single substructure within the model that has enforced non-zero displacement constraints at all points of contact with the slabs. Defining:

$\mathbf{U}^t$ = nodal displacement vector for dowel/beam substructure

$\mathbf{U}^c$ = enforced displacements at contact nodes for dowel/beam substructure

$\mathbf{U}^u$ = vector of unknown displacements at free dowel/beam nodes

$\mathbf{K}^t$ = assembled stiffness matrix for dowel/beam substructure

$\mathbf{P} = \mathbf{K}^t\mathbf{U}^c$

$\mathbf{F}$ = reactions at enforced displacement nodes

we can solve $\mathbf{K}^t\mathbf{U}^u = -\mathbf{P}$ for $\mathbf{U}^u$; the total displacement vector for the dowel/beam substructure is $\mathbf{U}^t = \mathbf{U}^u + \mathbf{U}^c$. After computing the reactions at the constrained nodes, $\mathbf{F}$, the direction of the individual reaction at each enforced displacement node, $\mathbf{F}_i$, may be dotted with the corresponding relative displacement, Δ_i, and released if required. This process is then applied repeatedly until no more constrained nodes are released ($n_f = 0$) or a maximum number of times, max_f, whichever occurs first.

Of course, we must also update constraints based on relative displacements at the free nodes. This is performed in an outer loop within which the previous iteration is contained. As with the inner loop where constraints are maintained/released based on nodal forces, the outer loop terminates when no more constraints are updated based on relative displacements ($n_d = 0$) or the maximum iteration limit, max_d, is reached. This leads to an updating

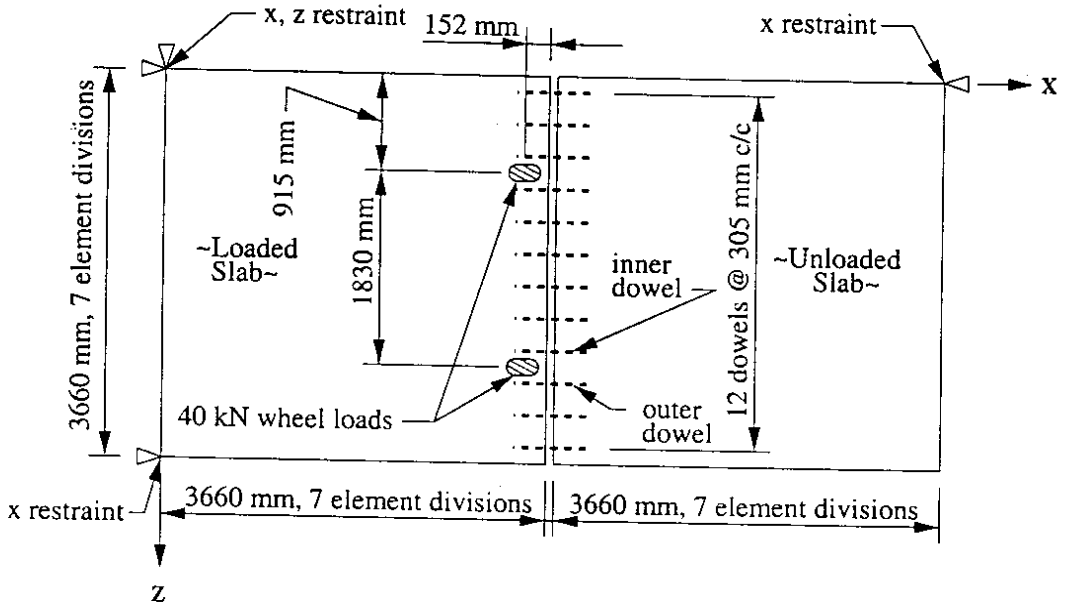

Figure 4.4: Plan View of Two Slab Model Problem

32 mm, and its modulus of elasticity taken as 200 kN/mm^2. The subgrade was modeled as a dense liquid foundation with a modulus, k, of 0.0407 N/mm^3. The value of k is known to vary with the magnitude and velocity of the wheel loading as well as the subgrade type [16, 54]; the value chosen here is considered representative for an untreated gravel subgrade. The only loading considered in this study was an equivalent single axle load (ESAL) of 80 kN applied as point loads near the joint as shown in Fig. 4.4. The slab boundary conditions are displacement constraints sufficient to prevent rigid body displacements and rotations as shown in Fig. 4.4.

The gap between the embedded dowels and the slab was assumed to be concentric, varying parabolically in magnitude along half the dowel length for both the loaded and unloaded slabs as shown in Fig. 4.5. Each dowel was considered to be debonded along its length, except at a single end node as required to prevent rigid body displacement of the dowel in its axial direction. The zero gap between the slab and the dowel near the dowel ends ensures that the dowel is constrained to the slab at these nodal locations, providing sufficient transverse dowel restraint. The magnitude of the gap at the joint was varied between 0 mm and 0.3 mm, as larger values had little effect on pavement response. Note that laboratory studies have indicated that the magnitude of the gaps formed under cyclic damage vary from about 0.3 mm to 0.6 mm, although no information about the variation in magnitude along the dowel length is known [10, 81]. The parabolic variation was assumed

Fig. 4.6. From these plots, it is clear that the LTE values and dowel shears converge with increasing numbers of dowel elements. Over the number of dowel elements considered, the LTE varies less than 3% for both the the inner and outer dowels, and the dowel shears vary approximately 2.5% in magnitude. Based on this convergence study, six elements per dowel line in each slab were used to discretize the dowels in the remaining runs. Note that this corresponds to three elements over the region of the gap.

Further studies examine the effect of the magnitude of the gap on the LTE and dowel shears. Figure 4.7 shows, for the outer dowel, the effect of the gap on LTE and dowel shears. Note that a gap of 0.3 mm reduces the LTE by over 50%, and that the outer dowel shear is reduced by approximately 500%. The variation in LTE is is in good agreement with measured values reported in [10], which showed a loss in LTE of over 50%. These results indicate that even relatively small gaps may have a large effect on the ability of the dowels to effectively transfer loads from the loaded slab to the unloaded slab.

4.9 Summary

An embedded formulation for a quadratic beam element incorporating both bending and shear deformations suitable for modeling dowel action in rigid concrete pavements has been proposed and developed. The embedded formulation has significant practical advantages over a discrete formulation, allowing both an exact mathematical representation of the dowels and regular meshes for the slabs. The specific advantages of the embedded formulation are as follows:

- Slab mesh divisions are not restricted to coincide with dowel lines.
- The element may be debonded at selected nodes.
- The nonlinear effect of gaps between the dowel and surrounding slab concrete may be explicitly modeled.
- The element stiffness is easily computed using a matrix transformation, and does not require special integration techniques. Both the effects of debonding and gaps are incorporated in this transformation.
- The dowel element permits the incorporation of a general bond-slip law, making it appropriate for modeling reinforcement in conventional reinforced concrete structures.

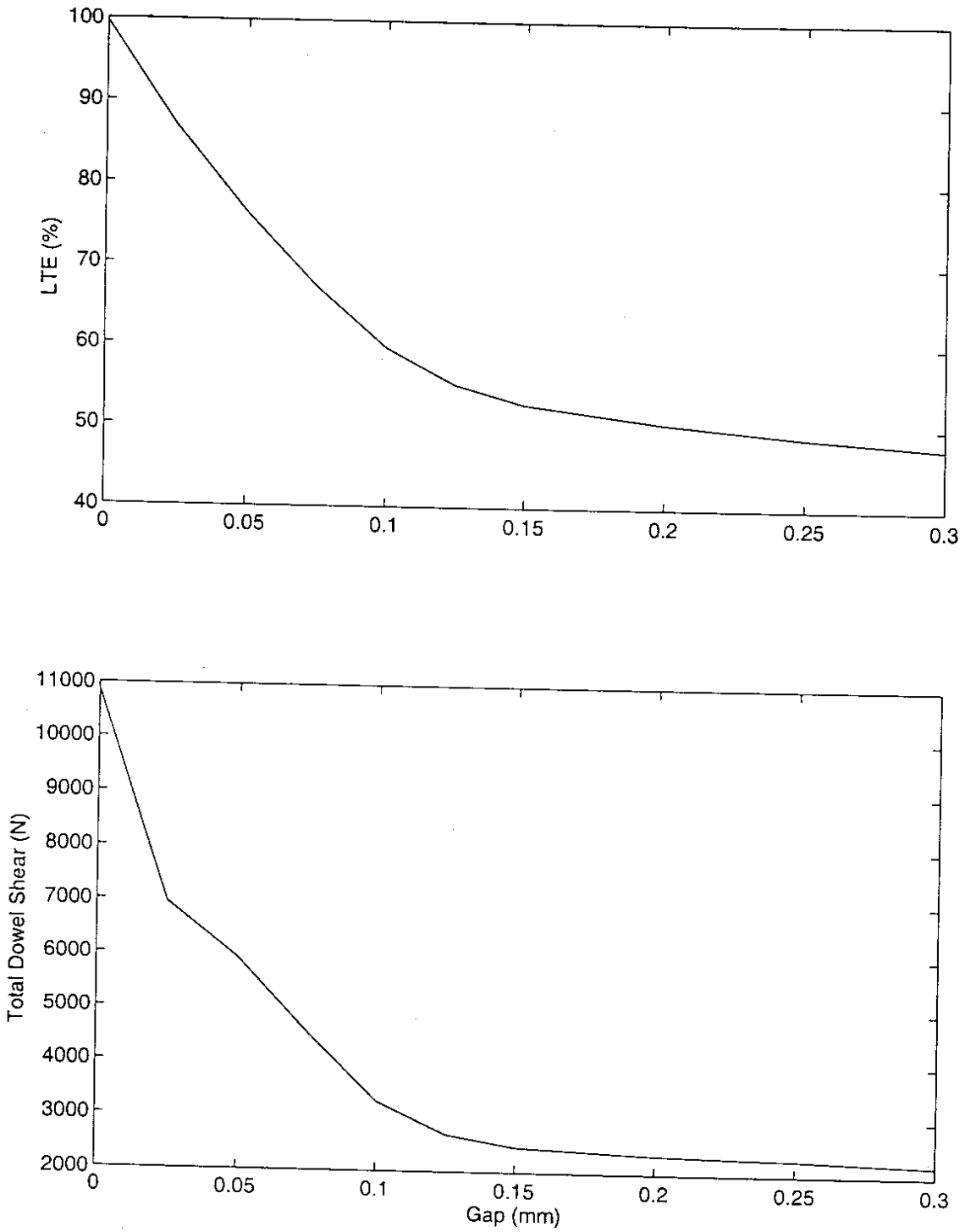

Figure 4.7: LTE and Joint Shear vs. Gap for Outer Dowel

Chapter 5

Aggregate Interlock

5.1 Introduction

Early experimental studies on aggregate interlock shear transfer in rigid pavements demonstrated that joint shear transfer effectiveness and endurance depend on many factors including joint width, slab thickness, load magnitude, foundation type, subgrade modulus, and aggregate shape [15].

Research into the more general problem of shear transfer across discrete cracks in concrete has shown the mechanics of aggregate interlock shear transfer to be highly complex. In addition to contact between asperities on joint surfaces, there may be localized crushing of both the cement paste and the aggregate (see Fig 5.1) [7, 91]. The amount of crushing

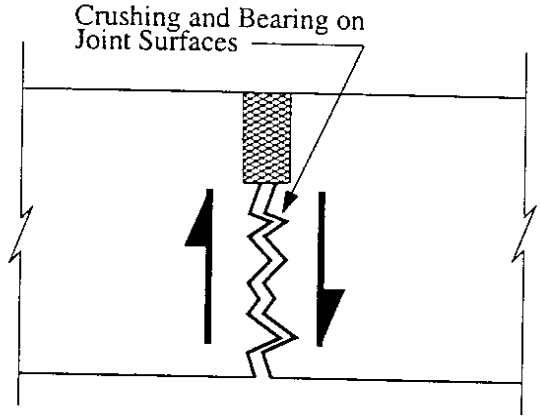

Figure 5.1: Aggregate Interlock Shear Transfer

and the bearing area of the surfaces depends on the joint opening, normal restraint of the joint, the strength of the concrete (both the paste and the aggregate), and the size and distribution of the aggregate particles [91]. A predictive model of aggregate interlock shear transfer at rigid pavement joints should take all of these factors into consideration. The

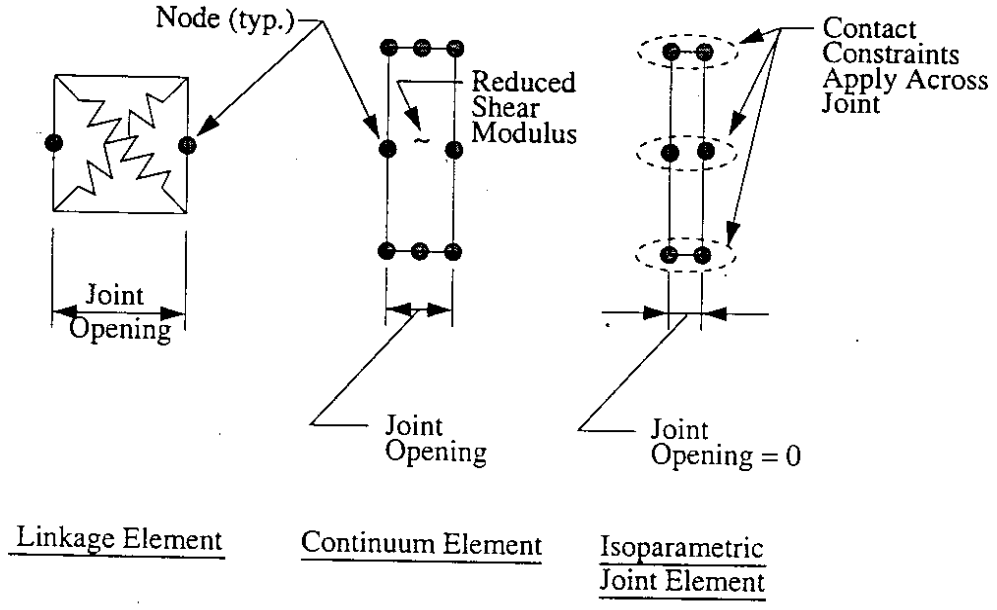

Figure 5.2: Common Elements for Modeling Aggregate Interlock Shear Transfer

Linkage elements have the obvious advantage of simplicity and ease of implementation, and are often used in finite element models of rigid pavement systems. However, it has been shown [7] that linkage elements are incapable of modeling joint shear transfer because of the indefiniteness of the constitutive relations. The error induced by this approach depends on the magnitude of the normal forces at the joint; as long as these normal forces are small, discrete springs may be acceptable. The use of a continuum finite element with a reduced shear stiffness is also unable to model the normal forces occuring at the joint. In addition, large relative tangential displacements at the joint may induce large element strains, violating small strain theory and requiring that higher-order strain approximations be employed. The third approach, while more complex, is desirable since any constitutive relations based directly on (δ_n, δ_t) may be incorporated [36]. This also avoids any potential difficulties that may arise from large strains occuring at the joint.

Attempts to rigorously incorporate complex aggregate interlock constitutive models within finite element models are uncommon, but this issue was tackled by Feenstra et al. [25, 26]. In these studies, various aggregate interlock constitutive models, including those developed by Walraven [91, 74] and Bazant [7], were implemented using isoparametric joint elements. Several significant computational difficulties were noted: (1) the element constitutive relations are quite complex, and (2) the incremental constitutive matrix is not symmetric (discussed in detail in the following Section). As shown by Feenstra et al. [25, 26], this lack of symmetry can result in unstable and/or poorly conditioned systems that require

5.3 Mechanics of Aggregate Interlock

5.3.1 Background

Early research on the empirical development of shear stress–displacement relationships was often conducted in relation to the design of nuclear containment structures. A summary of proposed shear stress–displacement relationships may be found in [11]. These models are largely empirical, relying on laboratory test data for determination of appropriate parameters, and generally apply to reinforced concrete structures. They may be divided into two broad categories:

- Isolated crack stiffness models that provide an interface shear stiffness per unit area given parameters such as concrete strength and the initial crack opening. These models are generally derived from fitting curves to experimental data of shear stress-displacement, and are limited to constant crack openings and/or crack restraint.
- Crack stiffness models that may be incorporated directly in element constitutive relations. These models may be analytical or based on extensions of isolated crack stiffness models. They are generally applicable for use with continuum elements, and involve reduction of the shear modulus based on crack width and stress.

More recent research on the mechanics of aggregate interlock has highlighted physical phenomena that these early models are not capable of rationally capturing. One of the most important and earliest studies of this type was that of Bazant [7], who examined the mechanical aspects of shear and normal stress transfer across cracks in plain concrete as part of a study on shear stress transfer across rough cracks in reinforced concrete. This work is significant since it represents an early attempt to comprehensively and rationally incorporate micromechanics and the effect of crack asperities in an aggregate interlock model.

Bazant [7] noted that shear slip across a crack requires an increase of the crack opening, which will increase the normal compressive stresses across the crack if it is restrained. Based on this observation, the incremental stress-strain relations for rough cracks were formulated in the context of monotonic loading using total displacements as follows:

$$\sigma_n = f(\delta_n, \delta_t) \tag{5.2}$$

$$\sigma_t = f(\delta_n, \delta_t) \tag{5.3}$$

$$d\boldsymbol{\sigma} = \mathbf{D}d\boldsymbol{\delta} \tag{5.4}$$

specimens with both internal restraint (conventional reinforcing bars intersecting the crack plane) and external restraint were conducted. The effects of concrete strength and aggregate gradation and maximum particle size were considered. In addition, bilinear curves were fitted to the experimental shear stress–shear displacement curves, with the main parameters being crack opening and concrete strength. Some conclusions of the experimental study related to plain (externally restrained) specimens are:

- For externally restrained cracks, crack opening path (relation between δ_t and δ_n) is influenced by the external restraining stiffness.
- High restraining stiffness keeps the crack opening small, giving a large total contact area and high shear resistance.
- The shear resistance depends on contributions from all aggregate particles with diameters larger than the crack width.

Millard and Johnson (1984)

This study [65] examined both aggregate interlock shear transfer and dowel shear transfer through a series of experiments. The primary goal of the aggregate interlock tests was comparison with previously developed theoretical models, including that developed by Walraven [91] (reviewed later in this Chapter).

A total of 19 aggregate interlock specimens were tested, with the main parameters being initial crack width (0.063 mm – 0.75 mm), concrete strength (29 N/mm^2 – 52 N/mm^2 cube strength), and specimen stiffness normal to the crack plane (1.2 N/mm^3 – ∞). One test was conducted with constant crack opening (infinite restraining stiffness). Tensile loading, inducing axial tension in the reinforcing bars, was applied through flexible straps to minimize the stiffness of the test rig. The specimens consisted of two concrete blocks with a pre-formed crack. Crack restraining stiffness was provided by two reinforcing bars extending through the specimen that were sleeved to prevent any contributing stiffness due to dowel action. All tests were monotonic, and loading was applied until failure.

The test results gave relationships between crack width, relative shear displacement, and normal and shear stresses on the crack. The following general trends were observed:

- Nominally identical specimens showed nearly identical behavior.
- Shear stiffness and ultimate shear stress decrease with increasing initial crack width. Cracks widen (open further) with increasing shear regardless of the initial value of the

- Due to the smoothing of the interfaces during cycling, there is a large drop in shear stiffness, and the force-response degradation is large. Further, the maximum crack dilatancy decreases with cycling, and the residual shear slip after unloading is nearly equal to the maximum shear slip for each loading cycle.

Tassios and Vintezeleou also presented empirical expressions which were developed to fit the shear hysteresis loops for both smooth and rough interfaces. The details of these expressions will not be repeated here. The authors caution that scale effects may be significant.

Divakar, Fafitas, and Shah (1987)

Divakar et al. [19] performed a series of monotonic shear tests on pre-cracked plain concrete specimens. The concrete strength of all specimens was 35 MPa, and the maximum aggregate size was 12.7 mm. Measured data for shear stress versus slip and slip versus dilation were taken at four different values of constant normal stress.

The test results and data previously published by other researchers were then used to develop analytical models to predict crack stiffness using total deformation theory in a manner similar to that of Bazant [7]. Empirically determined factors for crack shear stiffness, coefficient of friction, dilatancy, and normal stiffness were proposed. These factors were incorporated into expressions relating incremental displacements and stresses assuming that shear stress, σ_t, and normal displacement, δ_n, were functions of δ_t and σ_n. Expressions for the coefficients D_{nn}, D_{nt}, D_{tn}, and D_{tt} were then derived; the resultant matrix relating incremental displacements and stresses, D, was not symmetric positive definite, which is consistent with previous work by others [7]. The parameters defining the coefficients of D were optimized with respect to the author's and other published test data using nonlinear least squares. The accuracy of these analytical expressions was tested by comparison with published test data from several other sources that incorporated different degrees of crack normal restraint stiffness. Agreement with the test data was generally good, with the model somewhat overpredicting shear stress vs. slip in most cases.

5.3.3 Micromechanics-Based Models

Several models that allow prediction of crack stiffness and response based on a theoretical micromechanics-based approach have been developed. These models are reviewed in detail in this section.

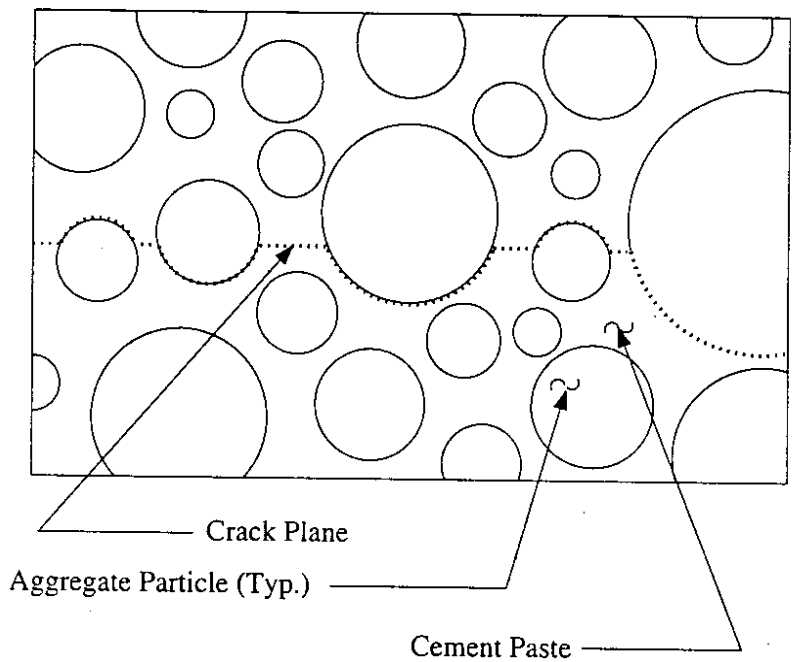

Figure 5.4: Distribution of Aggregate Particles

assumptions, the crack may be reduced to a two-dimensional problem of finite width. The shear and normal stresses at the crack result from the tangential and normal projections of the stresses produced when the cement paste deforms plastically as it bears on the aggregate particles (see Fig. 5.5). These stresses are related by assumption that the contact areas are about to slip, and thus:

$$\tau_{pu} = \mu\sigma_{pu} \tag{5.8}$$

where μ is the coefficient of friction between the paste and the aggregate, and σ_{pu} is the ultimate strength of the paste. The equilibrium of the crack plane requires that the net forces be balanced as follows:

$$\sigma_n = \sigma_{pu}(\overline{A}_x - \mu\overline{A}_y) \tag{5.9}$$

$$\sigma_t = \sigma_{pu}(\overline{A}_y + \mu\overline{A}_x) \tag{5.10}$$

where:

$\overline{A}_x$ = x-projection of the sum of the most probable contact areas

$\overline{A}_y$ = y-projection of the sum of the most probable contact areas

The determination of $\overline{A}_x$ and $\overline{A}_y$ is based on the statistical distribution of the aggregate in the concrete matrix, and the geometry of the spherical aggregate particles intersecting the crack plane at a given tangential and normal displacement.

with experimental data described in the literature.

- The resistance to shear deformations is governed by the concrete strength, with the diameter of the aggregate playing a secondary role.
- The aggregate grading curve does influence the shear transfer characteristics at larger crack widths. The influence of the grading curve on the normal stresses is minimal.
- The behavior of the cracks subjected to cyclic loading can be qualitatively described by the model.

Li, Maekawa, and Okamura (1989)

The work by Li et al. [56] represents a unique approach to the fundamental analysis of aggregate interlock shear transfer. The crack is assumed to be a rough surface with a number of areas, or contact units, having various angles of inclination, θ, that vary from $-\pi/2$ to $\pi/2$. A probability density function $\Omega(\theta)$ is assumed to give the probability of occurrence of any θ. The crack surface is shown schematically in Fig. 5.6. The second major assumption of the theory is that the direction of contact is fixed, and assumed normal to the initial contact direction, θ.

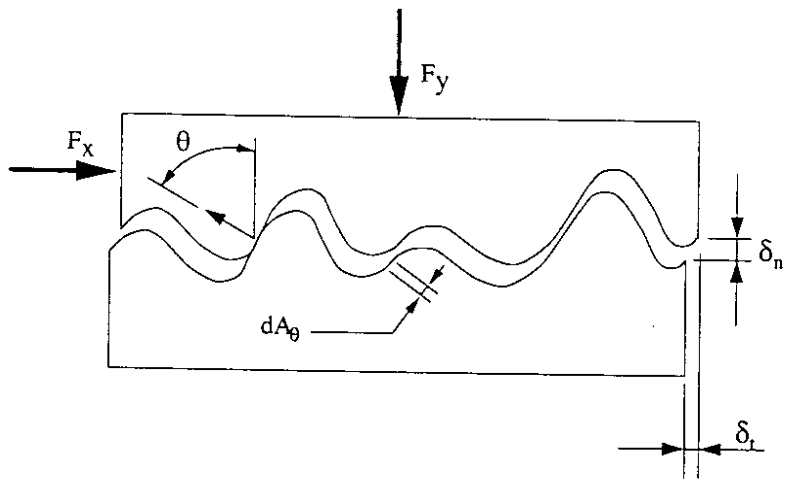

Figure 5.6: Surface Roughness – Model of Li et al.

A series of experiments were conducted at fixed crack widths. Based on the histogram of the measured surface profile of the crack, the following analytical form for $\Omega(\theta)$ was proposed:

$$\Omega(\theta) = 0.5cos(\theta) \tag{5.11}$$

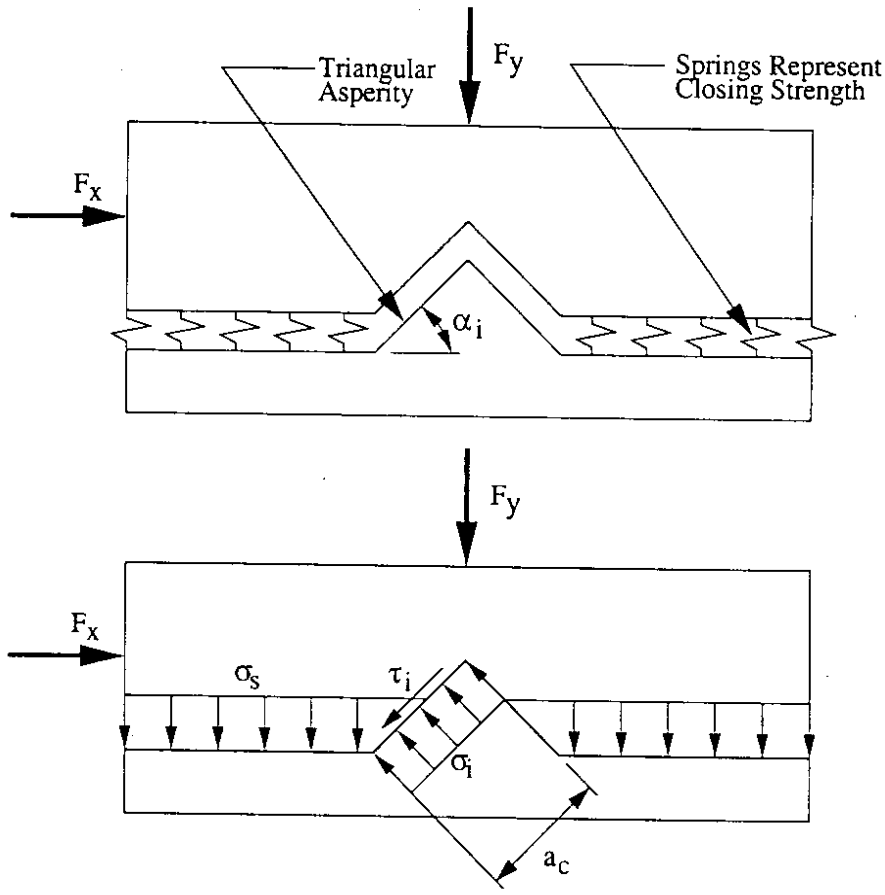

Figure 5.7: Equivalent Micromechanical Model of Crack (Divakar, 1992)

Writing the equations of equilibrium across the crack plane for a unit crack area gives

$$\sigma_t = \sigma_i a_c(\sin\alpha_i + \mu\cos\alpha_i) \tag{5.12}$$

$$\sigma_n = \sigma_i a_c(\cos\alpha_i - \mu\sin\alpha_i) - \sigma_s \tag{5.13}$$

where σ_n and σ_t represent the normal and tangential crack stresses corresponding to F_y and F_x acting over unit crack areas in Fig. 5.7.

Following this formal statement of the model, Divakar performed several regression analyses based on experimental data to determine expressions for α_i and a_c. The resulting equations were then verified by comparing computed values with existing constant normal stress and variable normal stress test data. In general, the model performed well, accurately predicting monotonic stress-displacement response.

be computed using Eqs. 16 and 17.

The normal stresses generated across the crack are balanced by the springs assumed to cross the crack plane as shown in Fig. 5.8. These springs may represent some external restraint mechanism, or reinforcing bars intersecting the crack plane. The discretization of the cement paste also allows the damage to the cement paste to be updated throughout the loading history by tracking the geometry of the paste layers for each particle diameter/embedment depth combination. A simple program may be written to perform simulations of both monotonic and cyclic loading for different parameters such as initial crack opening, restraining spring stiffness, etc. Another further addition to the theory as initially presented in the context of monotonic loading is the inclusion of the fracture index, C_f. This is used to proportionally reduce both the shear and normal stress transferred across the crack, and accounts for the fracturing of aggregate particles. Walraven notes that the value of C_f is characteristic of the specific concrete mixture, and must be determined from monotonic testing of a specimen and curve-fitting the resulting data.

Verification of the theory was accomplished by comparing computed shear stress vs. displacements with those from existing laboratory tests found in the literature [55]. In general, agreement between the tests and the theory was very good, and the simulations accurately capture the significant physical phenomena observed from testing. In contrast with the model of Li et al [56], Walraven's model is capable of predicting different loading/unloading paths for adjacent cycles.

5.4 Proposed Modeling Technique

5.4.1 Choice of Aggregate Interlock Constitutive Model

Due to the generality and extensibility of the micromechanics-based constitutive models, they are the best choice for modeling aggregate interlock shear transfer. The model of Fardis [23] is the least physically defensible of the micromechanics-based constitutive models, and is also computationally complex. Its resolution of aggregate interlock shear transfer into global shear and normal forces and a moment acting on the entire crack plane is not ideal for rigid pavement modeling.

The remaining models are all viable for the modeling of aggregate interlock shear transfer in rigid pavements. However, the two-phase constitutive model developed by Walraven [91, 92] has been chosen to model aggregate interlock shear transfer. The model was selected for several reasons:

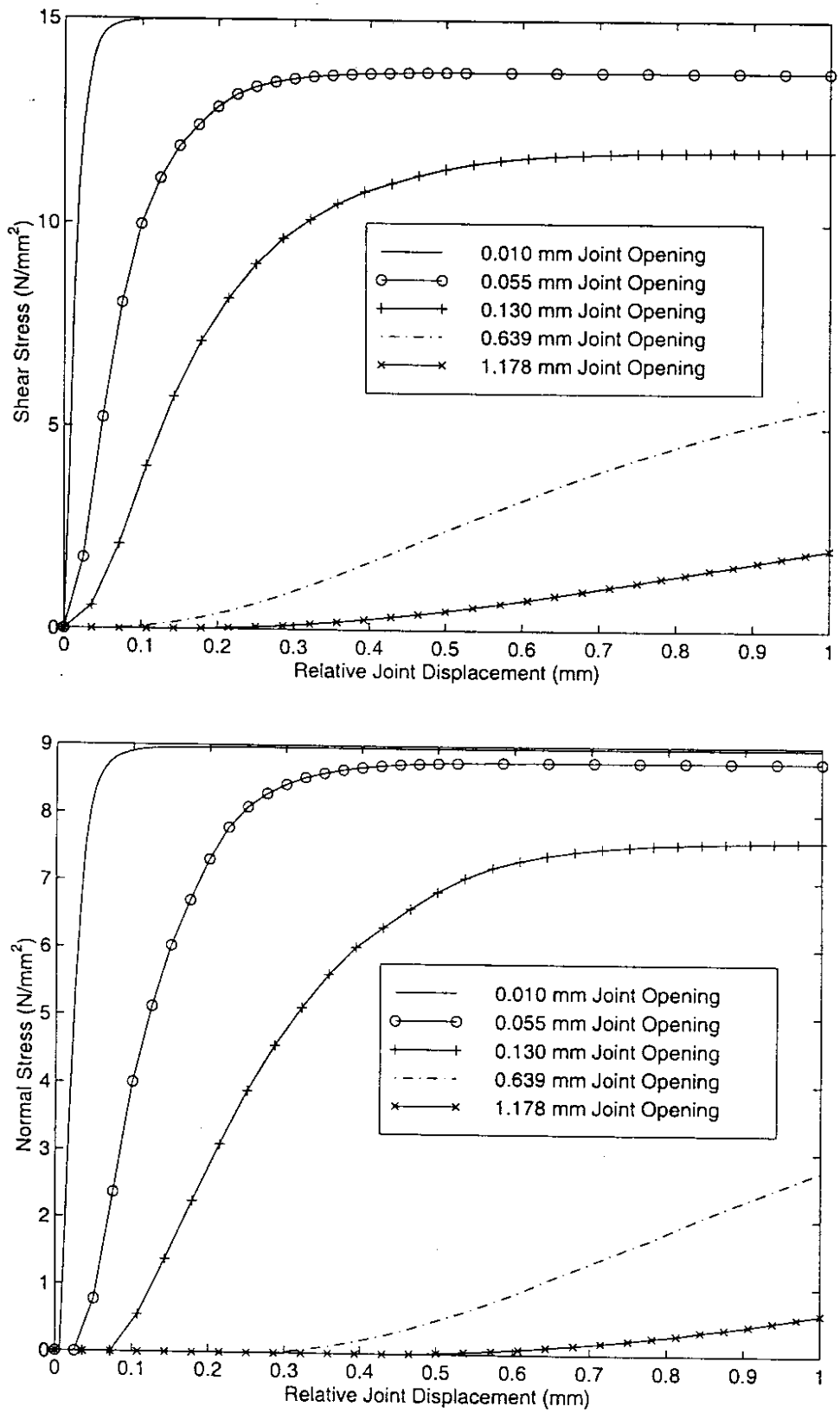

Figure 5.9: Shear and Normal Stresses vs. δ_t for Varying Crack Widths

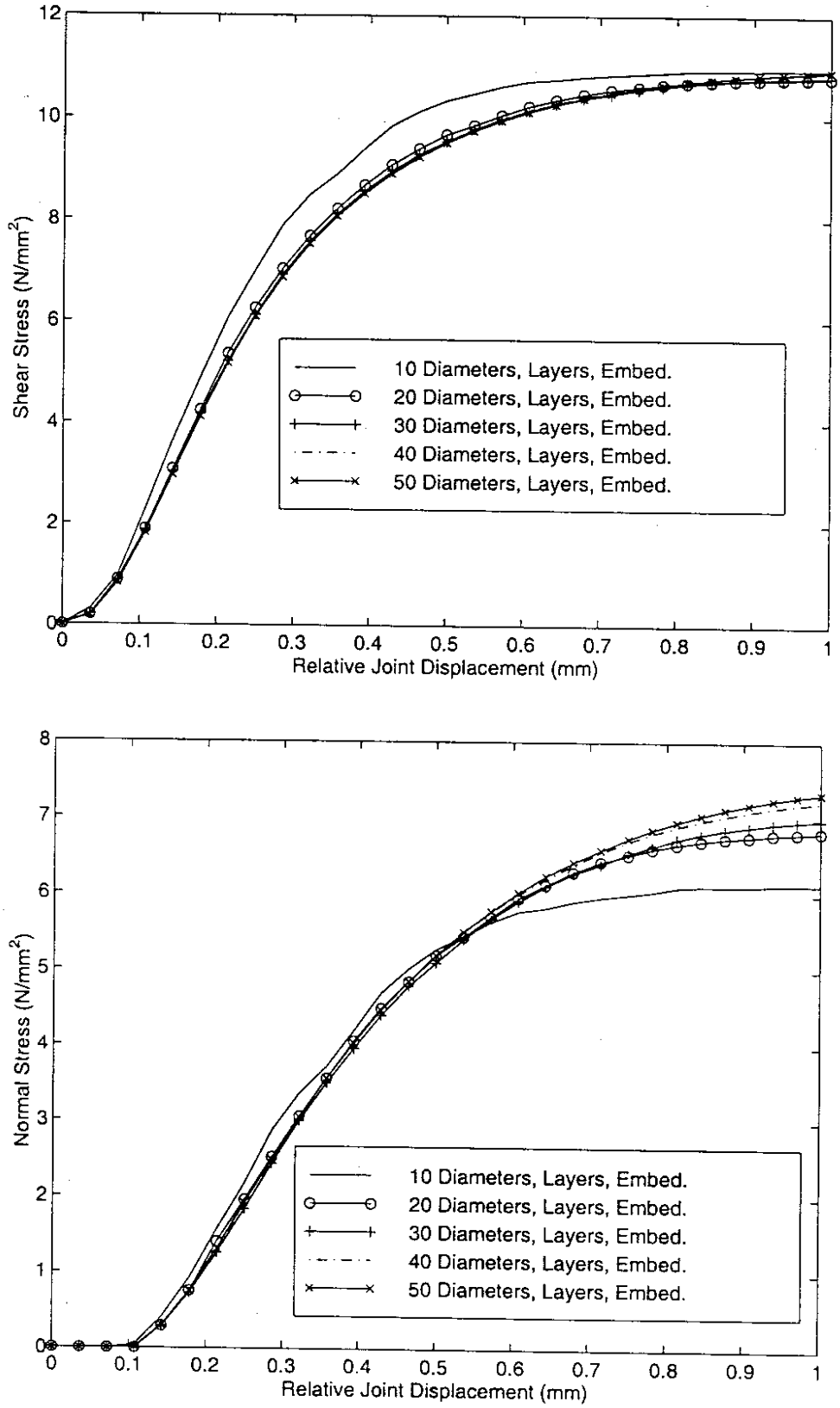

Figure 5.10: Normal and Shear Stress vs. δ_t for Varying Levels of Discretization

coordinate mapping [98]. The values of σ_n and σ_t are updated and stored at each integration point to allow the computation of the element nodal forces, $\mathbf{f}^e$ by the following integral:

$$\mathbf{f}^e = \int_A \mathbf{B}^{\mathrm{T}} \left[\mathbf{n}\sigma_n + \mathbf{v}\sigma_t\right] dA \tag{5.23}$$

5.4.4 Symmetry and Computational Issues

The final issue which must be addressed is the non-symmetry of the constitutive matrix predicted by Walraven's model. As noted in [25, 26], this may pose computational difficulties. Further, the efficient multigrid-preconditioned conjugate gradient solution techniques used in this study (see Chapter 6) may only be used with symmetric positive definite systems. The details of the proposed approach to overcoming this difficulty are presented in the remainder of this Section.

Consider the general form of the equilibrium statement for a finite element model:

$$\mathbf{P} - \mathbf{F} = 0 \tag{5.24}$$

where $\mathbf{P}$ is a constant vector of applied forces, and $\mathbf{F}$ is the vector of nodal forces determined by:

$$\mathbf{F} = \sum_{elements} \int_V \mathbf{B}^{\mathrm{T}} \sigma dV + \int_{A_j} \Gamma dA_j = \mathbf{F}_e + \mathbf{F}_j \tag{5.25}$$

The contribution to the nodal force vector, $\mathbf{F}$, by summation/assembly over the elements includes the slab, subgrade, and dowel elements. The contribution to $\mathbf{F}$ by joint shear and normal stress transfer is accounted for in $\mathbf{F}_j$, computed by separately integrating the tractions on the joint surfaces predicted by Walraven's model, Γ, over the area of the joint, A_j. The evaluation of $\mathbf{F}_j$ is accomplished by numerically integrating Eq. 5.23 for each joint element and summing/assembling.

The nonlinear solution strategy developed in Chapter 6 is similar to Newton's method in that it requires the formation of the Jacobian, $\mathbf{J}$, which is simply the tangent stiffness matrix:

$$\mathbf{J} = \frac{\partial \mathbf{F}_e}{\partial \mathbf{U}} + \frac{\partial \mathbf{F}_j}{\partial \mathbf{U}} = \mathbf{K}_e + \mathbf{K}_j \tag{5.26}$$

Strict evaluation of Eq. 5.26 results in an unsymmetric stiffness matrix, where $\mathbf{K}_e$ and $\mathbf{K}_j$ are the symmetric and unsymmetric contributions, respectively. However, we need not evaluate $\mathbf{J}$ exactly; in fact, approximations to $\mathbf{J}$ are often employed in quasi-Newton methods, and in modified Newton approaches $\mathbf{J}$ is not updated at every iteration. In the present study, a symmetric approximation to $\mathbf{K}_j$ will be used, denoted by $\mathbf{K}'_j$, which is computed by

Chapter 6

Solution Strategies

6.1 Introduction

In Chapter 3, a finite element modeling strategy for rigid pavement systems was outlined and the following three major goals of this study were identified:

- Develop better methods for modeling dowel load transfer.
- Improve techniques for modeling aggregate interlock shear transfer.
- Develop computationally efficient solution strategies for solving 3D finite element models of rigid pavement systems.

Discretization of the slab and subgrade, constitutive properties, and application of loads were also addressed in Chapter 3; Chapters 4 and 5 covered dowel and aggregate interlock modeling, respectively. At this point, all aspects of the proposed finite element models of rigid pavement systems have been defined. Fig. 6.1 shows a typical system of two rigid pavement slabs with all components of the system identified; Fig. 6.2 illustrates a typical finite element mesh of such a system.

The focus of this Chapter is on achieving the third major goal of this study: the development of efficient and robust solution strategies for finite element models of rigid pavement systems. This is a particularly challenging undertaking for several reasons:

- *Material nonlinearities.* The proposed aggregate interlock constitutive relations are nonlinear. In addition, while gaps between the dowels and the slabs give rise to contact nonlinearities, this phenomenon is actually treated as a material nonlinearity due to the embedded formulation of the dowel element.

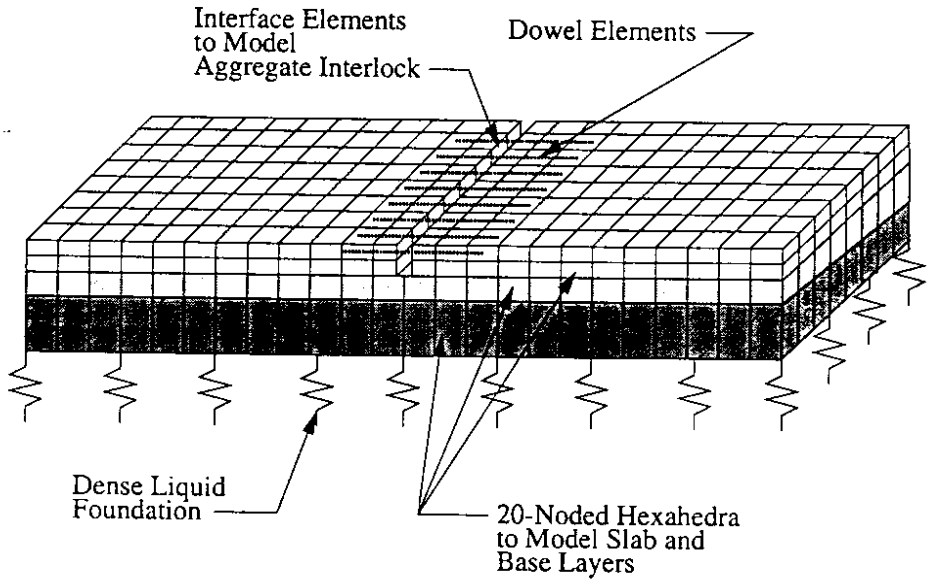

Figure 6.2: FE Mesh of System of Two Rigid Pavement Slabs

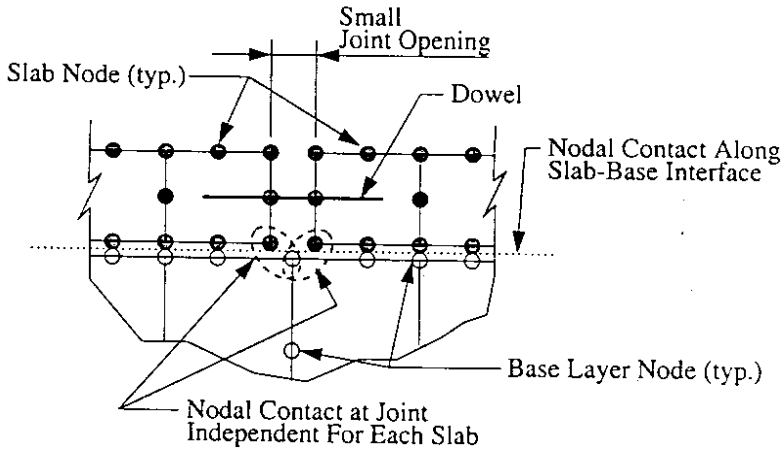

Figure 6.3: Detail of Mesh Near Joint Showing Double Nodes at Slab-Base Layer Interface

global solution strategy is evaluated using a model of a typical rigid pavement system incorporating several base layers and slab-subgrade separation. Section 6.7 presents a summary of this Chapter.

6.2 Global Solution Strategy

The global solution strategy must account for both material and contact nonlinearities. Here, an algorithm is developed that is analogous to a full Newton iteration: it is based on successive linearizations of the constrained system that employ a tangent system stiffness matrix and solution for a displacement increment at each iteration. Slab/subgrade

k:

$$\mathbf{K}^k \delta\mathbf{U}^k = \mathbf{r}^k \tag{6.3}$$

$$\text{s.t. } \mathbf{G}^{k\mathrm{T}}\mathbf{U} = \mathbf{c}^k \tag{6.4}$$

where:

$$\begin{aligned} \delta\mathbf{U}^k &= \text{displacement increment to be solved for} \\ \mathbf{r}^k &= \text{the current residual} \end{aligned}$$

The tangent system stiffness matrix, $\mathbf{K}^k$, constraint matrix, $\mathbf{G}^k$, and $\mathbf{c}^k$ are superscripted as they change at each iteration due to material nonlinearity and constraint updating. Recognizing that the current solution vector, $\mathbf{U}$, may be written as:

$$\mathbf{U}^k = \mathbf{U}^0 + \delta\mathbf{U}^1 + \ldots + \delta\mathbf{U}^k \tag{6.5}$$

the constraints may be expressed as:

$$\mathbf{G}^{k\mathrm{T}}\left(\mathbf{U}^{k-1} + \delta\mathbf{U}^k\right) = \mathbf{c} \tag{6.6}$$

or:

$$\mathbf{G}^{k\mathrm{T}}\delta\mathbf{U}^k = \mathbf{c}^{*k} \tag{6.7}$$

where:

$$\mathbf{c}^{*k} = \mathbf{c}^k - \mathbf{G}^{k\mathrm{T}}\mathbf{U}^{k-1} \tag{6.8}$$

The constrained system given by Eqs. 6.3 and 6.4 may now be rewritten with the constraints expressed in terms of the displacement increment as:

$$\mathbf{K}^k \delta\mathbf{U}^k = \mathbf{r}^k \tag{6.9}$$

$$\text{s.t. } \mathbf{G}^{k\mathrm{T}}\delta\mathbf{U}^k = \mathbf{c}^{*k} \tag{6.10}$$

6.2.2 Solving the Constrained System

Several alternatives are available for enforcing constraints, the most common of which are penalty parameters and Lagrange multipliers [6]. Application of penalty parameters to Eqs. 6.9 and 6.10 leads to the following system:

$$\left(\mathbf{K}^k + \alpha\mathbf{G}^k\mathbf{G}^{k\mathrm{T}}\right)\delta\mathbf{U}^k = \mathbf{r}^k + \alpha\mathbf{G}^k\mathbf{c}^{*k} \tag{6.11}$$

To circumvent these problems, a block iteration will be used that reduces the problem one step further to the solution of a symmetric positive definite system at each iteration. In particular, an adaptation of Uzawa's method will be employed as detailed in [77, 99]. Note that $\mathbf{K}^k$ itself is singular, since the only vertical support provided to the slab is through contact with the upper base layer, and methods based on the Schur complement of $\mathbf{K}^k$, $\mathbf{G}^{\mathbf{T}}(\mathbf{K}^k)^{-1}\mathbf{G}$ are not feasible. The variation of Uzawa's method employed here requires that Eq. 6.12 be modified by the following perturbation:

$$\begin{bmatrix} \mathbf{K}^k + \mathbf{K}' & \mathbf{G}^k \\ \mathbf{G}^{k\mathbf{T}} & \mathbf{0} \end{bmatrix} \begin{bmatrix} \delta\mathbf{U}^k \\ \delta\boldsymbol{\lambda}^k \end{bmatrix} = \begin{bmatrix} \mathbf{r}^k + \omega\mathbf{G}^k\mathbf{c}^{*k} \\ \mathbf{c}^{*k} \end{bmatrix} \tag{6.13}$$

where $\mathbf{K}' = \omega\mathbf{G}^k\mathbf{G}^{k\mathbf{T}}$ is a perturbation to the system stiffness matrix ($\mathbf{K}^k + \mathbf{K}'$ is nonsingular). Note that once the constraints are satisfied, the perturbation does not modify the original system. The scalar perturbation parameter, ω, is mathematically equivalent to a penalty parameter, and may be interpreted as a spring stiffness. However, it is typically chosen to be a relatively small value so as not to cause numerical difficulties. The perturbed system is then solved iteratively as follows:

$$\mathbf{y} = \mathbf{G}^{k\mathbf{T}}\delta\mathbf{U} - \mathbf{c}^{*k} \tag{6.14}$$

$$\delta\boldsymbol{\lambda} = \delta\boldsymbol{\lambda} + \omega\mathbf{y} \tag{6.15}$$

$$\delta\mathbf{U} = (\mathbf{K}^k + \mathbf{K}')^{-1}\left((\mathbf{r}^k + \omega\mathbf{G}^k\mathbf{c}^{*k}) - \mathbf{G}^k\delta\boldsymbol{\lambda}\right) \tag{6.16}$$

For convergence, ω must be sufficiently small [99]; numerical studies indicate that if ω is the same order as $avg(\mathbf{K}^k_{ii})$, convergence is not impaired and is fairly rapid. More complex perturbations can be employed in an attempt to speed convergence, but in general the simple approach presented is sufficient.

Algorithm 6.1 gives the global solution strategy employed in this study. Note that it employs three levels of iteration: (1) at the outer level, the nodal constraints and tangent system stiffness matrix (appropriate for use in a Newton iteration) are updated; (2) the constrained problem is solved using Uzawa's method; and (3) the innermost kernel requires

the number of unknowns, making factorization techniques inefficient for large problems. To circumvent these problems, iterative solution techniques must be employed.

One of the most effective iterative solution techniques for symmetric positive definite (SPD) systems such as Eq. 6.17 is the conjugate gradient method. Details of the development and basis of the conjugate gradient algorithm will not be presented here, but may be found in many sources [29, 77]. The basic preconditioned conjugate gradient algorithm is given in Algorithm 6.2.

The effectiveness of the conjugate gradient method is largely dependent on preconditioning the original system of equations, which is accomplished on line 12 of Algorithm 6.2. Note here that the matrix M is an approximation to the system stiffness matrix, K. Many alternatives are available for preconditioning; the simplest rely on standard iterations, such as Jacobi or symmetric SOR. However, these are generally not effective for large problems [77]. Another alternative is to use an incomplete factorization for the system stiffness matrix, i.e. compute M as:

$$\mathbf{M} = \mathbf{L}'\mathbf{U}' \tag{6.18}$$

where $\mathbf{L}'$ and $\mathbf{U}'$ have been determined assuming some specified degree of fill-in relative to K, often fixed at zero. Incomplete LU factorization (or Choleski factorization for symmetric positive definite systems) is a viable preconditioner for large problems, although it requires extra memory for the storage of $\mathbf{L}'$ and $\mathbf{U}'$. The effectiveness of zero fill-in incomplete Choleski preconditioned conjugate gradient (ILU-PCG) will be briefly examined later in

6.4 Multigrid Methods

6.4.1 Review of Multigrid Methods

To solve a SPD system of equations such as that of Eq. 6.17 (or equivalently, precondition a linear system within a MG-PCG iteration), the multigrid (MG) method relies on a few applications of a standard iterative technique, called smoothing, which is intended to reduce the high frequency components of the solution error, $\mathbf{e}$, coupled with coarse grid approximations to the smoothed error [8].

The error in the solution, $\mathbf{e} = \mathbf{U}^* - \mathbf{U}$, is related to the residual, $\mathbf{r}$, by $\mathbf{r} = \mathbf{Ke}$. Here $\mathbf{U}^*$ denotes the exact (unknown) solution and $\mathbf{r}$ is computed as:

$$\mathbf{r} = \mathbf{P} - \mathbf{KU} \tag{6.19}$$

Using these these definitions, the general, recursive multigrid algorithm is as shown in Algorithm 6.3 [47]:

```
multi_grid(level, r, e)
 1  if level = 1
 2    then ▷direct solution at coarsest level
 3         e = K^{-1} r
 4    else for i = 1, ..., β
 5         do
 6            e = smooth(e, r)  ▷ pre-smoothing
 7            r = r − K_level e
 8            r_{level−1} = R_level r
 9            ▷recursive call to next coarsest level
10            e = multi_grid(level − 1, r_{level−1}, e_{level−1})
11            e = T_level e_{level−1}
12            e = smooth(e, r)  ▷ post-smoothing
13            end for
14         end if
15  return
```

Algorithm 6.3: General Recursive Multigrid Algorithm

In the above algorithm, the operator $\mathbf{R}$ restricts from the fine mesh to the coarse mesh, and $\mathbf{T}$ interpolates the coarse mesh error to the fine mesh. This subroutine is placed in an outer loop, and called repeatedly until an appropriate convergence criteria is met. If the inner loop limit, β, is greater than one, the algorithm corresponds to a 'W-cycle', where multiple processes of smoothing/restricting and interpolating/smoothing at coarser levels

Despite the progress in developing multigrid methods for 3D finite element modeling of structures and solid mechanics problems, there are still many issues which must be addressed before they can be used routinely and reliably for the solution of complex structures such as the rigid pavement systems of interest in this study.

- Multigrid methods should be generalized to allow multiple element types and varying numbers of nodal degrees of freedom within the same model. This is clearly of interest in the present study which requires that dowel elements be meshed with solid elements.

- The use of unstructured sequences of meshes should be allowed. It is often impractical in 3D to generate nested sequences of meshes due to constraints on element aspect ratios and limits on the problem size. When local mesh refinement is required or complex geometries are considered, this problem becomes even more difficult as automatic mesh generation codes do not readily generate nested sequences of meshes.

- Multigrid methods need to be generalized to handle nonlinear problems with contact constraints. Contact constraints cause difficulties because of the need for defining appropriate intergrid restriction and interpolation operators for them.

- There is a need for multigrid methods that can be conveniently integrated with conventional, displacement-based finite element methods to avoid expensive replication of existing FE codes.

This section presents the development of multigrid methods that fulfill these needs. Only V-cycle multigrid will be used ($\beta = 1$ in Alg. 6.3); as shown by Parsons and Hall [70], there is not a significant difference in computational effort between the V-cycle and the W-cycle for well-conditioned problems without singularities. Point-wise symmetric Gauss-Seidel smoothing will be employed in all analyses – note that a symmetric smoother is required when using multigrid as a preconditioner within a conjugate gradient iteration. Coarse grid solutions are achieved using SuperLU [17, 57], a state-of-the-art sparse direct solver. General methods for the intergrid transfer of information are developed, including restriction and interpolation operators and techniques for handling spatially varying materials. Details of the searching algorithms required to allow the efficient implementation of these techniques are also discussed. Finally, the incorporation of contact nonlinearities required for the present problem is presented.

The Interpolation Operator

A natural way of determining **T** when using the finite element method is to use the element shape functions to interpolate the displacements from the coarse to the fine mesh. This also guarantees that the interpolation has the same degree of accuracy as the solution. Considering the general case, defining **T** for two unstructured meshes then involves the following as illustrated in Fig. 6.5:

- For every fine mesh node, the coarse mesh element it is located within is determined.
- The natural (local) coarse mesh element coordinates corresponding to the physical fine mesh nodal coordinates are computed for each node/element pair.
- The element shape functions evaluated at these local coordinates allow interpolation from the coarse mesh nodal values to the value at the fine mesh node.

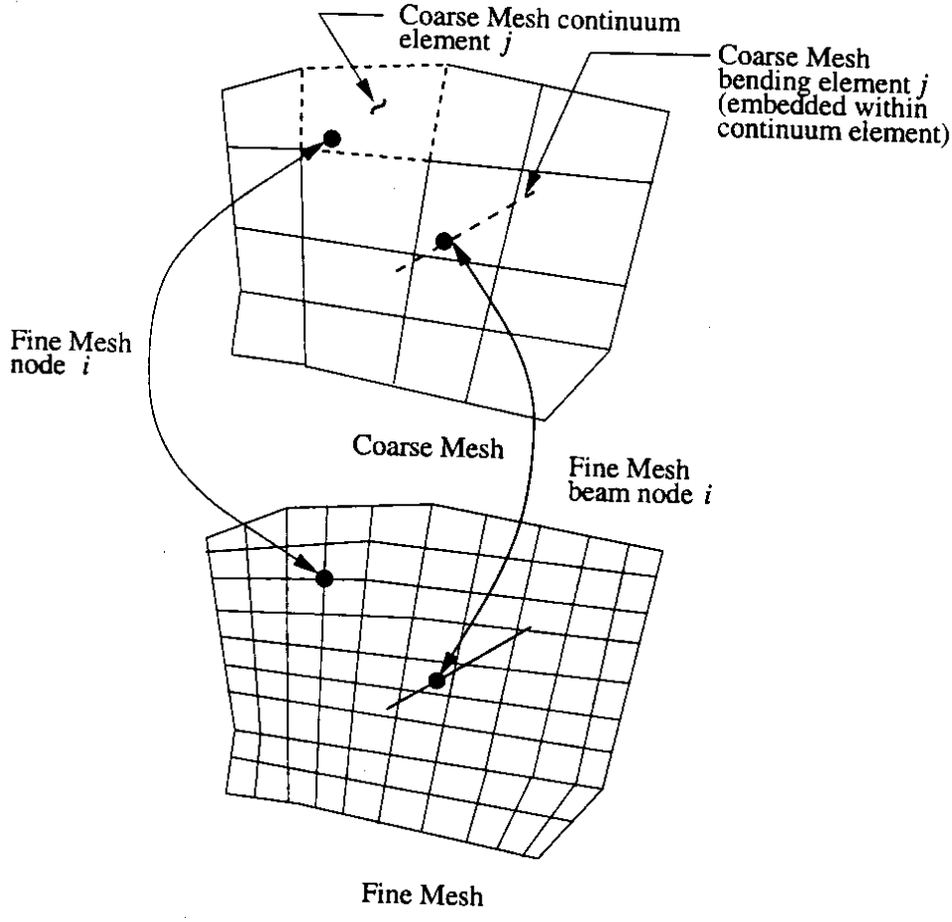

Figure 6.5: Interpolation and Restriction

Searching Algorithm

A difficulty with the proposed definitions of $\mathbf{R}$ and $\mathbf{T}$ is the determination of the node/element pairs for general unstructured meshes. A naïve search would require $\mathcal{O}(n^f n^c)$ operations and be prohibitively expensive. To maintain the linear proportionality between n^f and solution time, this information must be determined with computational effort proportional to n^f. To achieve this goal, a searching algorithm based on a grid projection technique similar to that described in [58] is employed, which also proves useful for the intergrid transfer of material properties as shown later in this Section. Only elements with straight edges/surfaces are considered.

To illustrate the method with a 2D example, consider Fig. 6.6 which shows fine and coarse meshes, $\mathcal{M}^f$ and $\mathcal{M}^c$, discretizing the same physical domain. Superimposed over $\mathcal{M}^f$ and $\mathcal{M}^c$ is a rectangular grid, $\mathcal{G}$, defined by the maximum dimensions of the domain. For any element of $\mathcal{M}^c$ with straight edges, it is simple matter to determine what cells of $\mathcal{G}$

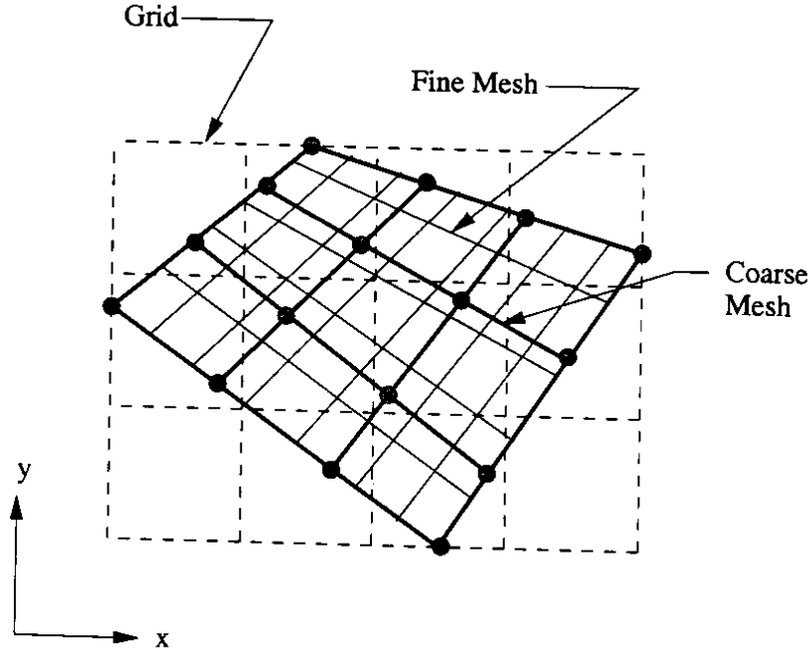

Figure 6.6: Grid Search

it overlaps by checking its maximum and minimum coordinates against the bounds of the cells. Given a list of elements of $\mathcal{M}^c$ for each cell in $\mathcal{G}$, the coarse mesh element containing any (x, y) point may be found by searching only the list of coarse mesh elements associated with the cell that the point lies within. The determination of whether or not a point lies within an element involves simple vector operations for an element with straight edges/faces;

which the constitutive relations are defined. The computation of the strain increments and subsequent updating of the stress states at the coarse element integration points is then performed by the appropriate fine mesh elements. One potential problem with this technique must be noted: if the coarse mesh is not defined appropriately in regions where large changes in material properties occur, $\mathbf{K}^c$ may not provide a sufficiently accurate coarse grid approximation. This issue will be explored numerically with a model problem in the next Section.

Incorporation of Contact Conditions

In this study, MG-PCG methods are used in the solution of the linear system in Algorithm 6.1. However, since constraint imposition and updating are done only for the fine mesh where a solution is achieved, the perturbation, $\mathbf{K}'$, must be restricted from the fine mesh to all coarser meshes. This poses a difficulty: since the constrained fine mesh nodes do not necessarily coincide with the coarse mesh nodes, a fine mesh nodal contribution to the perturbation cannot be merely added to the coarse mesh stiffness. This may be overcome by forming the coarse mesh perturbations as:

$$\mathbf{K}^{tc} = \mathbf{K}^c + \mathbf{R}\mathbf{K}'\mathbf{R}^{\mathbf{T}} \tag{6.26}$$

where $\mathbf{K}^{tc}$ refers to the total coarse mesh stiffness and $\mathbf{K}^c$ is assembled from the coarse mesh stiffness matrices as detailed previously. The term $\mathbf{R}\mathbf{K}'\mathbf{R}^{\mathbf{T}}$ represents the coarse mesh perturbation that is consistent with the virtual work requirement that the fine and coarse mesh strain energies be equal; this term will be denoted as $\mathbf{K}'^c$ for the remainder of this discussion.

To simplify the calculation of $\mathbf{K}'^c$, it is computed separately for each pair of constrained nodes. Refer to Fig. 6.4, which shows the fine mesh nodes i and j as being constrained; the nodal contribution to the fine mesh perturbation is represented by a spring, whose stiffness may be expressed as:

$$\omega(\mathbf{n} \otimes \mathbf{n}) \tag{6.27}$$

Using the searching algorithm detailed previously, the coarse mesh elements within which these fine nodes lie may easily be determined. Defining $\mathbf{N}_i$ and $\mathbf{N}_j$ as the usual arrays of shape functions of the coarse mesh elements that the fine mesh nodes i and j lie in, the coarse mesh perturbation corresponding to the constraint at nodes i and j is easily

β (defined previously) must be less than κ, a parameter denoting a uniform level of mesh refinement (typically $\kappa = 2^3$ in 3D); and (3) the total number of meshes, m, is a function of $\frac{\beta}{\kappa}$. Implicit in item (3) is that the level of discretization of the finest mesh must be chosen so that m is large enough.

The requirements for linearity between N_{ops} and n when using sequences of unstructured, unnested meshes are not so easily defined. For example, when automatic mesh generation is used to generate a sequence of meshes, refinement is often done only in selected regions of the mesh where solution errors are high. Further, complex geometry often requires the use of distorted elements or different element types, making it impossible to define a general level of refinement. For these reasons, the relationship between N_{ops} and n is studied numerically using different discretizations of the domain shown in Fig. 6.7.

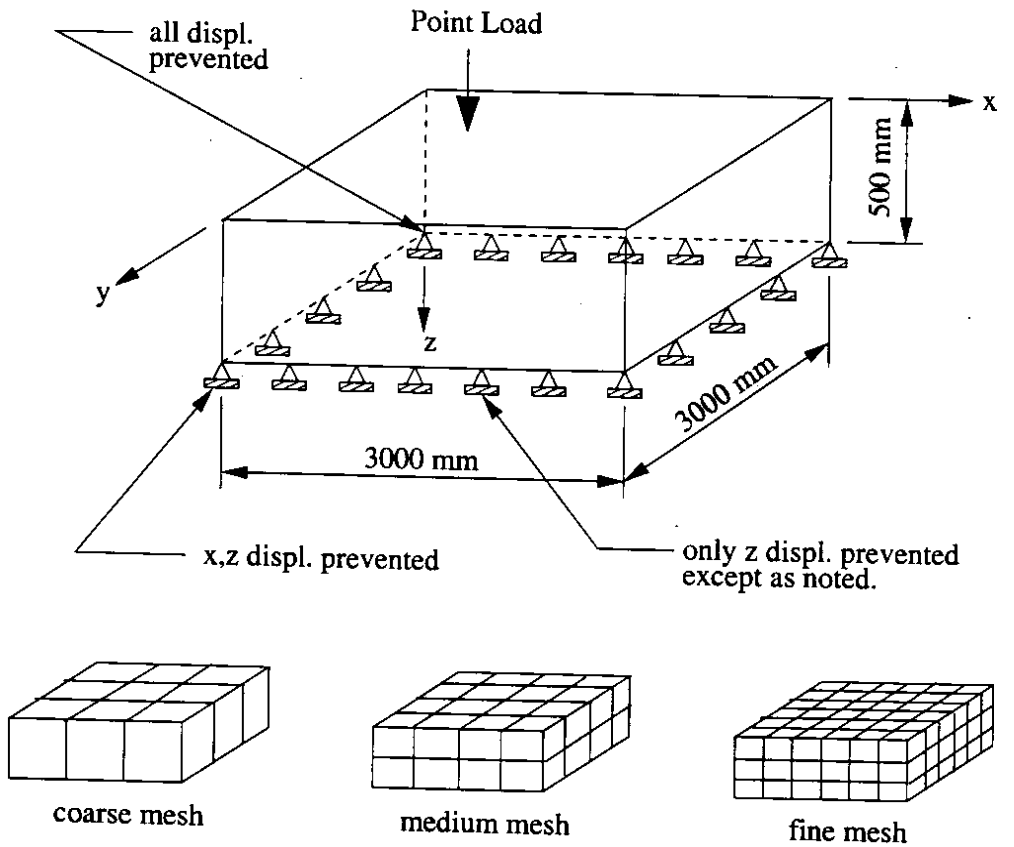

Figure 6.7: Thick Plate Model and Typical Mesh Sequence

Table 6.1 defines the sequences of meshes used to study convergence, along with the number of degrees of freedom, n, for each mesh. Uniform meshes with reasonable element aspect ratios are used to minimize numerical effects on convergence. The modulus of elasticity, E, was fixed at 100, and $\nu = 0.20$ for all cases.

The chosen mesh sequences have the following characteristics:

1. The number of meshes, m, is fixed at three for each sequence.
2. The coarsest mesh is identical for each sequence of meshes.
3. The level of discretization of the intermediate mesh is approximately midway between the finest and coarsest meshes.
4. Although the discretizations at the finest mesh level are regular, the mesh sequences are unnested, and general definitions of the interpolation and restriction operators are required.
5. No attempt was made to optimize the mesh sequences.

Fig. 6.8 shows the real time required for each aspect of the MG and MG-PCG solutions. All runs were done on a Sun UltraSparc 1/200 with 256 MB of RAM, using only core memory. The number of MG or MG-PCG iterations required to achieve convergence is taken as the first iteration where

$$\epsilon = \frac{\| \mathbf{r} \|_2}{\| \mathbf{P} \|_2} \leq 10^{-05} \tag{6.29}$$

$\mathbf{P}$ is defined as the vector of applied nodal forces and $\mathbf{r}$ is the vector of fine mesh residual forces. The following observations can be made from Fig. 6.8:

- MG-PCG clearly outperforms MG for all levels of discretization, and exhibits a nearly linear increase in solution time as the mesh is refined.
- MG suffers fairly severe performance losses as the mesh is refined, with a superlinear relationship between solution time and n.
- The amount of computational effort required to build the auxiliary data structures, which include $\mathbf{R}$, $\mathbf{T}$, and the coarse mesh stiffness matrices, is about half that required to assemble $\mathbf{K}$.

Fig. 6.9 compares the total solution times for MG-PCG, ILU-PCG, and sparse direct factorization. For the direct sparse solution [17], minimum-degree reordering was employed, but no pivoting was used as it is not required for well-conditioned symmetric positive definite systems. The largest problem which could be factored in-core corresponded to a mesh with $15 \times 15 \times 3$ elements and 11136 nodal DOF.

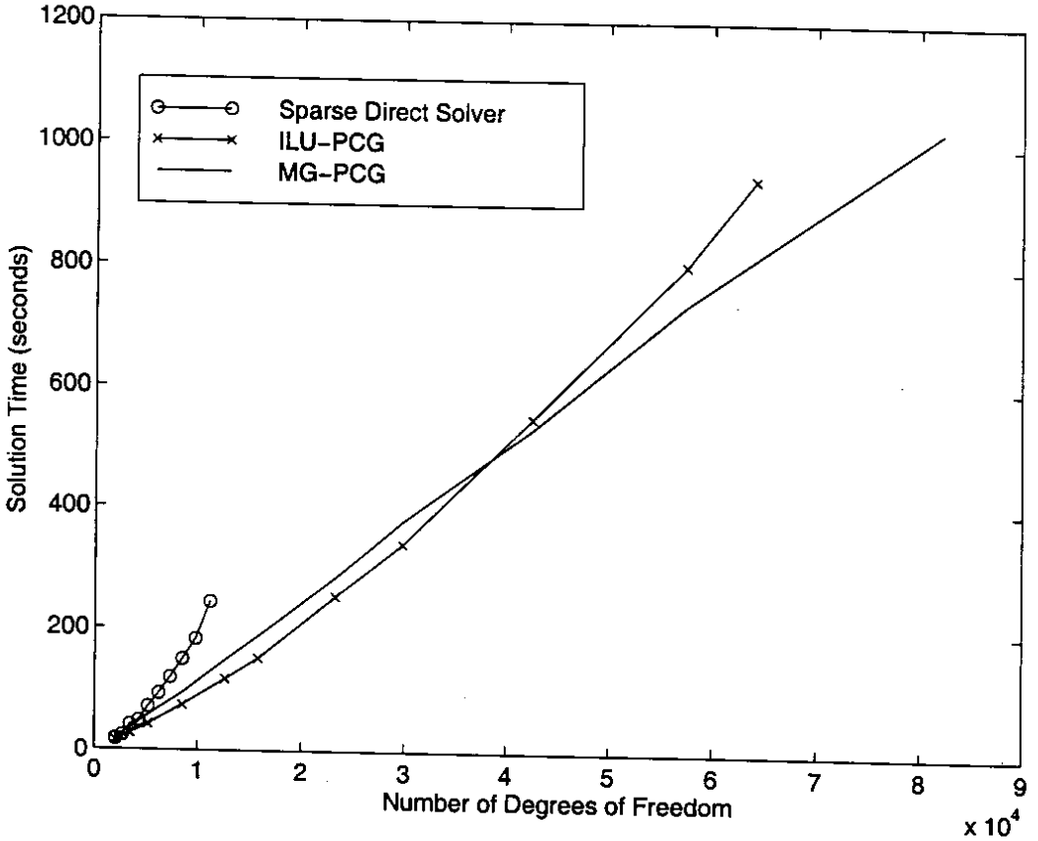

Figure 6.9: Relative performance of MG, MG-PCG, ILU-PCG, and Sparse Direct Solver

analyzed thick plate, but the fine mesh is refined over the center 750 mm by 750 mm region as shown in Fig. 6.10. The total number of elements is 960, and $n = 14949$, which nearly equal the values for the fine mesh in sequence (6). The coarse and medium meshes used in the refined mesh solution are the same as those in sequence (6), and are shown in Fig. 6.10.

The amount of time required to achieve a solution using MG-PCG was 185 seconds. Comparing this value with the total solution times in Fig. 6.9 indicates that there is effectively no loss in efficiency for MG-PCG when compared to regular mesh solutions with the same number of unknowns. We note here that regular coarse meshes were used to achieve a solution on an irregularly refined mesh with no difficulty.

The second model problem is an equilateral triangular plate discretized as shown in Fig. 6.11. All the meshes in the multigrid hierarchy are irregular (generated using the automatic mesh generator QMG [66]). The boundary conditions consist of vertical supports on one edge and at the opposite vertex, and horizontal supports sufficient to prevent rigid body motion. A point load is applied near the center of the plate where the mesh is refined. The total time required to solve this problem using the MG-PCG method was approximately

the coarse mesh element stiffness matrices, $\mathbf{k}$, by the usual Gaussian integration of:

$$\mathbf{k} = \int_V \mathbf{B^T D B} dV \tag{6.30}$$

where $\mathbf{B}$ is a matrix of linear operators and $\mathbf{D}$ is the constitutive matrix. Gaussian integration is exact for polynomials, the order of which depends on the number of integration points used. In this study, $3 \times 3 \times 3$ Gaussian integration is used to evaluate Eq. 6.30, which is exact for a quadratic, hexahedral element with uniform, linearly elastic material properties. If a coarse mesh element covers a region with more than one applicable constitutive law, a sharp "jump" in $\mathbf{D}$ may occur, possibly introducing significant error in the evaluation of $\mathbf{k}$. This is studied with the following model problem, which has been purposely constructed to introduce significant errors due to sharp material boundaries.

Consider the mesh shown in Fig. 6.12, which follows the same pattern as the refined mesh presented in the previous section, but with fewer elements. The center $4 \times 4 \times 2$ block of rectangular elements is assumed to have a modulus of elasticity, E_c, differing from the remainder of the domain, where E = 100 N/mm^2. To solve the problem using MG or MG-PCG, a single coarse mesh consisting of 9 elements is used. Fig. 6.12 shows that if the regular, 9 element coarse mesh presented previously (denoted by $\mathcal{M}_c$) is used, only three of the 27 center element integration points lie within the center 750 mm$\times$ 750 mm refined region of the fine mesh, which can be expected to introduce significant error in the evaluation of $\mathbf{k}$. However, if the coarse mesh element boundaries coincide with the material property boundary, the evaluation of $\mathbf{k}$ is exact (see Fig. 6.12); this mesh is denoted by $\mathcal{M}_e$.

Fig. 6.13 shows the effect of using $\mathcal{M}_e$ as opposed to $\mathcal{M}_c$. Note that no results are presented for MG with $\mathcal{M}_c$ and $E_c/E > 20$, as it diverges (convergence can be achieved for $E_c/E > 20$, but only by increasing the number of Gauss-Seidel smoothing operations within each MG cycle). The following observations are based on the results presented in Fig. 6.13:

- When using $\mathcal{M}_e$, the solution times for both MG and MG-PCG are essentially constant, verifying that the only source of error is the variation in the coarse mesh element boundaries.

- MG-PCG appears to be stable even if significant errors are introduced by the use of $\mathcal{M}_c$, and the increase in solution time is only doubled for $E_c/E = 100$.

- The performance of both MG and MG-PCG is improved by the use of $\mathcal{M}_e$ as opposed to $\mathcal{M}_c$, indicating that errors in integrating the coarse mesh stiffness can have

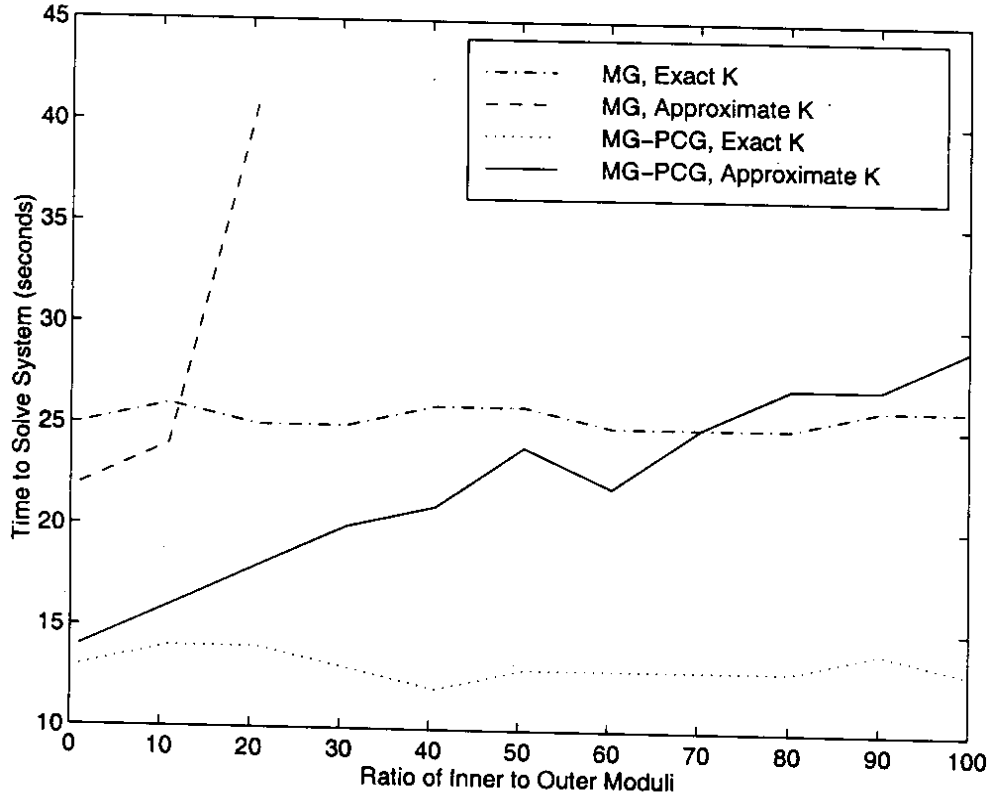

Figure 6.13: Spatially Varying Material Properties and Element Integration Error

6.6 Rigid Pavement Model Problem

In this Section, a typical model of a rigid pavement system will be solved to illustrate the applicability of the global nonlinear solution strategy to problems involving multiple element types and nodal contact.

6.6.1 Model Description

The system to be modeled is typical, consisting of two doweled, 254 mm thick rigid pavement slabs resting on two 300 mm thick base layers above the natural subgrade – similar to the system illustrated in Fig. 6.1. The slabs are 3350 mm long by 3660 mm wide and are separated by a transverse construction joint skewed at an angle of 10°. Three 485 mm long, 32 mm diameter dowels spaced at 300 mm are located in each wheelpath at the mid-thickness of the slabs. The slabs and base layers are meshed with 20-noded quadratic brick elements. The dowels are modeled using the embedded dowel element developed in Chapter 4. The natural soil below the solid elements is treated as a dense liquid foundation, and meshed with 8-noded quadratic interface elements that share nodes with the elements

The left-most slab was subjected to a single axle load of 80 kN near the joint. The axle was centered transversely on the slab with a wheel spacing of 1830 mm, and each wheel load was distributed over a 500mm×250mm area. In addition, the slabs were subjected to a linear temperature gradient through their thickness corresponding to a -5°C temperature change at the top of the slab and a +5°C temperature change at the bottom. This temperature differential required that the loss of contact between the unbonded upper base layer and the slab be modeled using the nodal contact approach presented in the previous Section. This dictated that the slab and upper base layers be meshed independently; details near the transverse joint are depicted in Fig. 6.3. The value of the parameter ω required for the Uzawa iteration was computed at run-time as the average value for all constrained nodes of $\mathbf{K}_{ii}$ corresponding to the constraint direction, $\mathbf{n}$. To illustrate the analysis results, a 3D perspective of the displaced shape is shown in Fig. 6.15 (displacements are scaled by factor of 500); note the slab lifting off the base layer due to the temperature gradient.

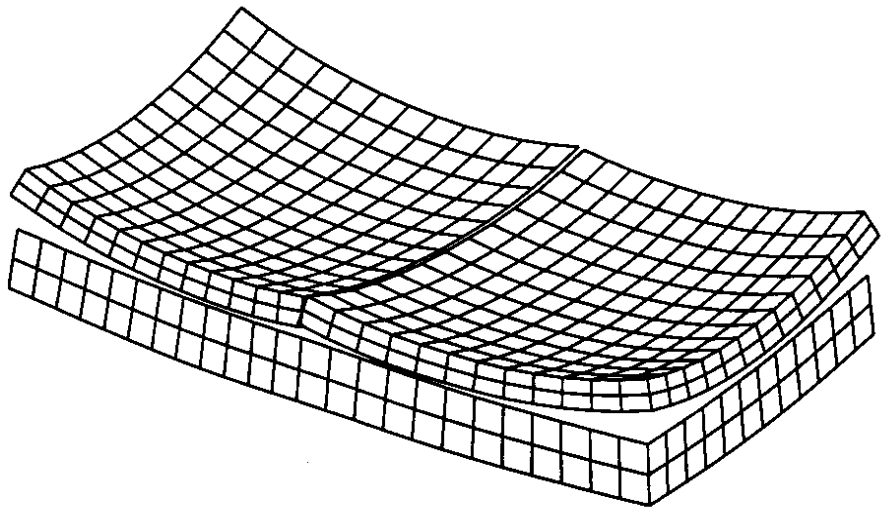

Figure 6.15: Displaced Shape of Rigid Pavement System

6.6.2 Performance of Solver

The iterative nonlinear solution strategy presented in Section 2 was used to solve the model problem. Both the global convergence tolerance, ϵ, and the constraint tolerance, ϕ were fixed at 10^{-05}. The solution required 12 global iterations and 2731 seconds of CPU time to solve on a Sun UltraSparc 1/200 workstation, and was achieved using only core memory. The following table gives a breakdown of the solution components. Note that the total number of Uzawa iterations required to achieve convergence for the constrained system

level is an iterative solution of the constrained system for increments of displacement and Lagrange multipliers, and the the inner kernel requires the iterative solution of a linearized, symmetric positive definite system.

To minimize the computational effort required in the inner kernel of the global solution algorithm, appropriate multigrid (MG) and multigrid-preconditioned conjugate gradient (MG-PCG) methods have been developed. These methods are quite general, relying on definitions for the interpolation and restriction operators that allow multiple element types and the meshing of bending members with solid elements within a single model. Spatially varying material properties are handled in a manner that relies on similar principles used to develop the restriction and interpolation operators. The MG and MG-PCG methods have also been extended to handle difficulties in forming the coarse mesh perturbations to the system stiffness matrices required by the nonlinear solver when modeling problems involving contact nonlinearities.

Baseline performance studies were conducted, providing comparisons between MG and MG-PCG methods vs. a state-of-the-art sparse direct solver and ILU-PCG. The MG-PCG method was shown, as expected, to be significantly more efficient than direct solution methods for large problems and exhibits a nearly linear increase in solution time with the number of unknowns. When compared with ILU-PCG, MG-PCG is more efficient for well-conditioned linear problems with more than approximately 40000 unknowns, and ILU-PCG exhibits a superlinear increase in solution time with the number of unknowns. Memory requirements beyond the storage of the stiffness matrix (or the element stiffness matrices) are small. The effectiveness of the proposed intergrid transfer techniques was demonstrated in the presence of mesh irregularities, local refinement, spatially varying material properties, and sharp material boundaries that may not be captured by all grids in the multigrid hierarchy. Further, the ability to precondition problems involving inequality constraints via restriction of the required fine mesh perturbation to unnested coarse meshes was shown to be effective in the general nonlinear solution strategy.

Lastly, a model problem of a rigid pavement system was solved that incorporated multiple element types, spatially varying materials, and nodal contact conditions to illustrate the application of the nonlinear solution strategy employing MG-PCG.

length. Of the six tests completed, the first two (LSM-1A and LSM-1B) had an undoweled joint and were essentially tests of a single slab. Test LSM-2 consisted of two doweled slabs resting directly on the rubber pad; tests LSM-3 through LSM-5 employed a cement-treated base. For further details on all tests, see the report by Hammons [33].

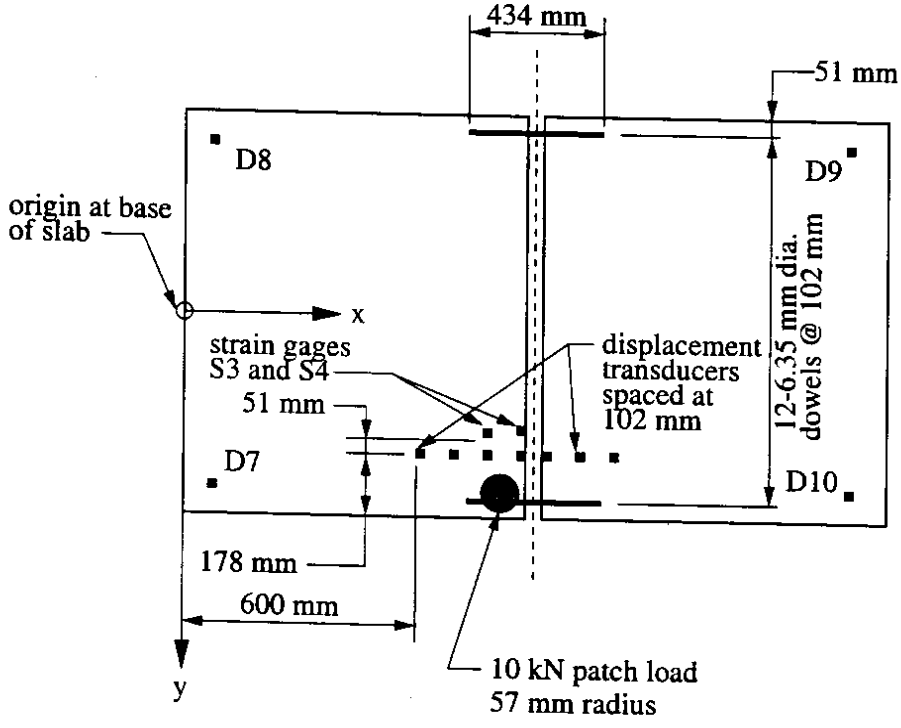

Figure 7.2: Dowel Locations, Loading, and Instrumentation [33]

Hammons also conducted finite element analyses for comparison with his experimental data using the commercially available program ABAQUS. Material properties of the slab and treated base were determined by testing specimens taken when the models were constructed in accordance with ASTM specifications. For analytical purposes, the rubber pad was idealized as a dense liquid. Its modulus, k, was based on the value back-calculated by Hammons using the laboratory data from the first two tests, LSM-1A and LSM-1B. Test LSM-1A consisted of a single slab resting directly on the rubber pad and subjected to an edge load; back-calculation using a finite element model yielded a value of $k = 0.070$ MPa/mm for best-fit displacements. It must be noted that the value of k is a secant stiffness that is dependent upon the configuration and loading of the system. This was experimentally observed by back calculating $k = 0.09$ MPa/mm for the same single slab resting on the rubber block when subjected to a corner load (test LSM-1B). The higher value of k for LSM-1B may be attributed to the higher and more localized stresses applied to the rubber

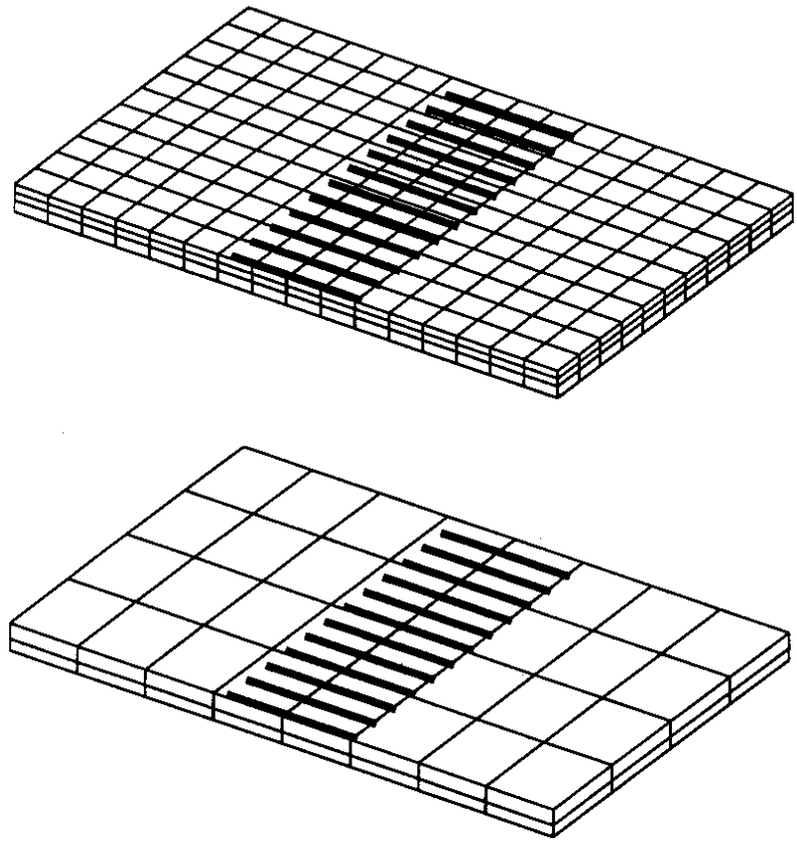

Figure 7.3: Mesh Sequence for Test LSM-5

calculated by Hammons using a 3D finite element model developed using ABAQUS to give good deflection profile comparisons with tests of a single undoweled slab founded directly on the rubber pad and subjected to corner loading. The moduli of the slab and subgrade are representative of the mean values determined from cylinder tests of specimens taken when the slabs and base layer were cast. All material properties are identical to those used by Hammons in his finite element verification studies [33].

7.2.2 Model Boundary Conditions

The model boundary conditions were chosen to reflect those of the laboratory tests. The reaction box in which the slabs were cast and tested was designed to prevent displacement of the ends of the slabs, increasing their effective length. On the sides of the slabs perpendicular to the joint, the reaction box was coated with a form release agent, and the slabs were poured against the box. Displacement transducers D7 through D10 near the slab corners (see Fig. 7.2) were monitored throughout the tests to check displacements near the slab ends.

and the loaded slab as shown in Fig. 7.4. Note that four dowel elements were located near the joint to better capture potential contact, with two more dowels used to discretize the remaining embedded portions of the dowel. This gives a total of 13 potential contact points for each dowel. The odd dimension of 114.25 mm is necessary since each dowel element must be completely embedded within a single solid element, and the hexahedra used to discretize the slabs have a dimension of 114.25 mm in the x-direction.

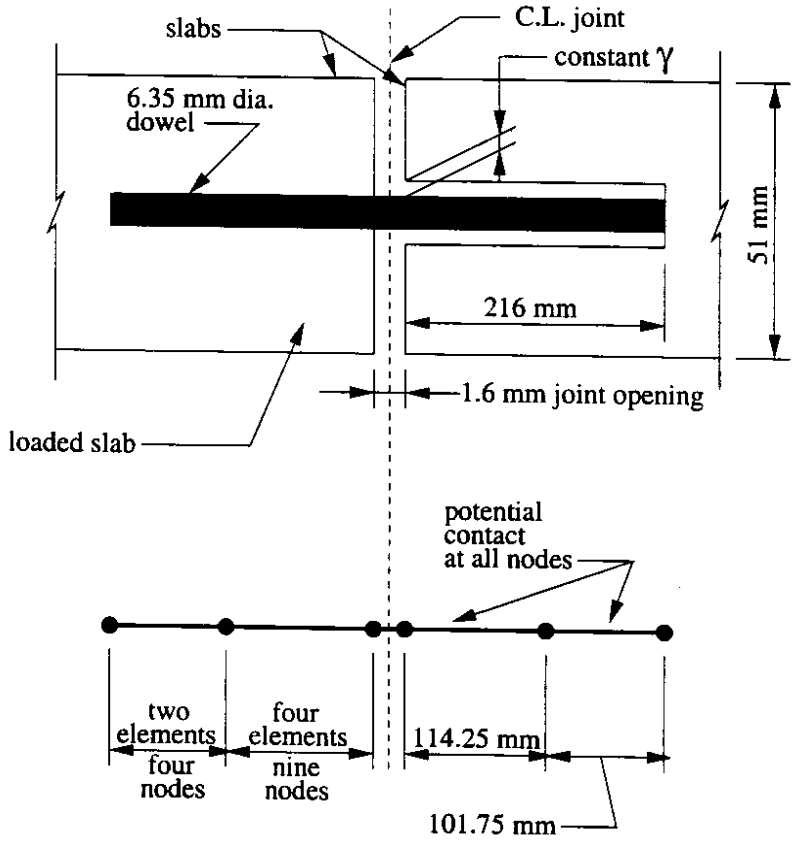

Figure 7.4: Assumed Profile of Gap around Dowels

7.3 Model Results

7.3.1 Results for LSM-2

Two different finite element analyses were run for LSM-2: the first assumed no dowel looseness; the second run assumed that a uniform gap, γ, of 0.08 mm existed between the dowel and the unloaded slab. This value of γ was chosen to give a relative vertical displacement between the two loaded and unloaded slabs that closely matches the experimentally measured values. Note that the measured wall thickness of a typical drinking straw is about

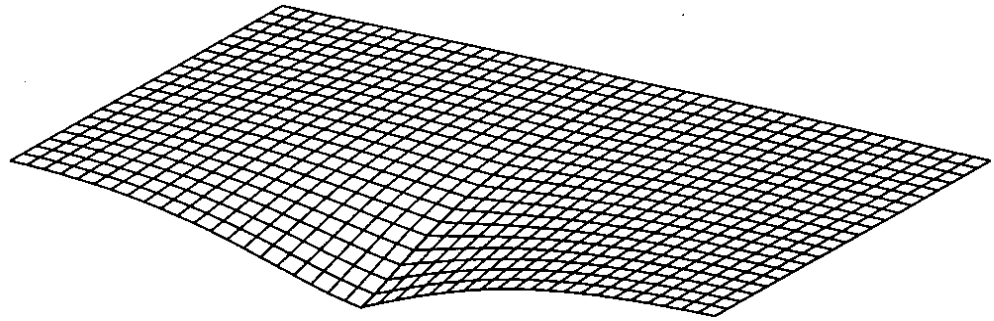

Gap = 0.00 mm

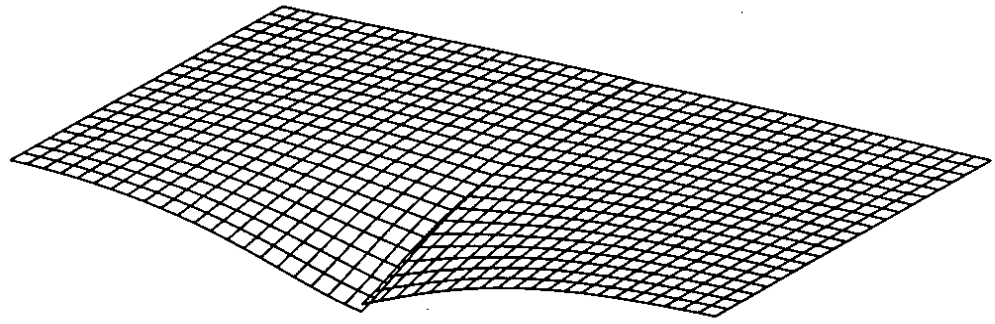

Gap = 0.08 mm

Figure 7.5: Displaced Shape of Top of Slab for LSM-2

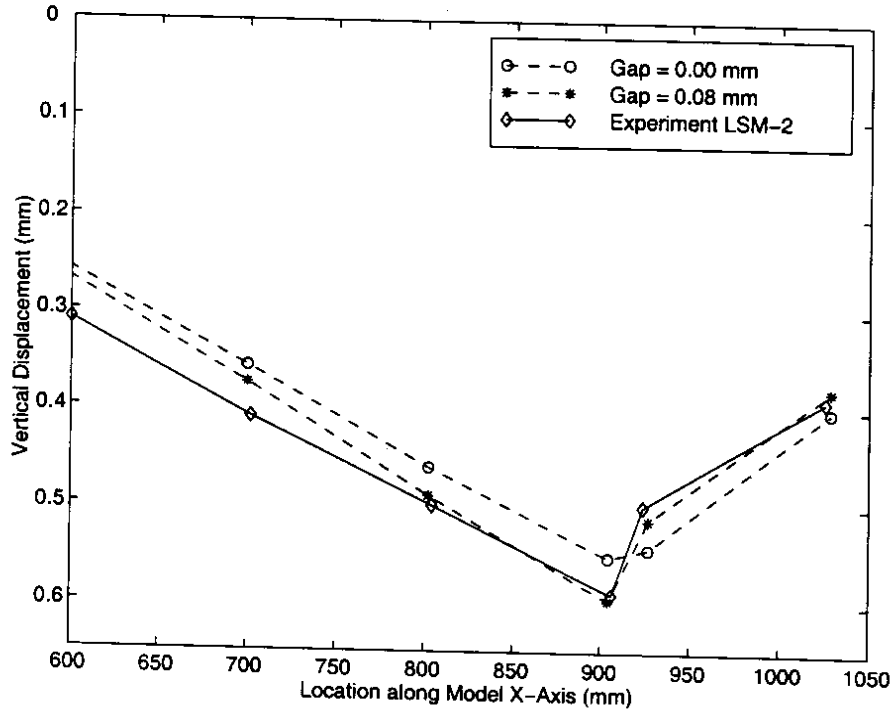

Figure 7.6: Deflection Basin Comparison for LSM-2 at $y = 432$ mm

7.3.2 Results for LSM-5

As for LSM-2, two different finite element analyses were run for LSM-5. However, in both analyses, the value of γ was fixed at 0.08 mm based on the results of LSM-2. The first analysis was conducted with an assumed modulus of subgrade reaction for the rubber pad, k, of 0.09 MPa/mm. The second analysis assumed $k = 0.070$ MPa/mm. This reduction is plausible: the value $k = 0.09$ MPa was determined from comparison with a test of a single corner loaded slab resting directly on a dense liquid. Lack of a treated base layer will increase the stresses applied to the rubber pad; since it is a strain-hardening material, the stiffness back-calculated from this test will be too high for case LSM-5, where the stresses are smaller and more uniformly distributed to the rubber pad by the cement-treated base. Figure 7.8 shows the displaced shape of the top surface of the slabs predicted by both finite element models.

Figure 7.9 compares the predicted and experimental deflection basins. Note that for both finite element models, the predicted relative displacement at the joint is quite accurate, validating the 0.08 mm gap determined from the analysis of LSM-2. Fig. 7.9 shows significantly better prediction of displacements when $k = 0.070$ MPa/mm is assumed, in particular near the joint region. However, the maximum error observed is about 17%, larger than that for LSM-2. Also note that the predicted slope of the deflection basin is significantly steeper than that observed experimentally. Possible factors for this include inaccurate modeling of boundary conditions as well as nonlinear and creep response of the rubber block not accounted for in the finite element model. In particular, since the rubber is a strain-hardening material, it will be softer further away from the load and stiffer nearer the load, tending to decrease the predicted slope of the deflection basin.

Figure 7.10 compares the strain (ϵ_{yy}) measured at gages S3 and S4 with the values computed by the finite element model. These results assume a k of 0.070 MPa/mm for the rubber pad. The experimental strain traces are plotted as reported by Hammons, and show compressive strain. This is inconsistent with the observed failure mode, however, which was the development of several corner cracks near the gage locations that would clearly result in tensile strain at gages S3 and S4. This is also inconsistent with the results of LSM-2 which showed measured tensile strains at gages S3 and S4. It is not known if the measured compressive values were actually tensile and were incorrectly reported due to experimental error, or if another explanation exists for this anomaly. If the measured strains are actually tensile, the computed strains are reasonably accurate at the maximum load of 10.2 kN,

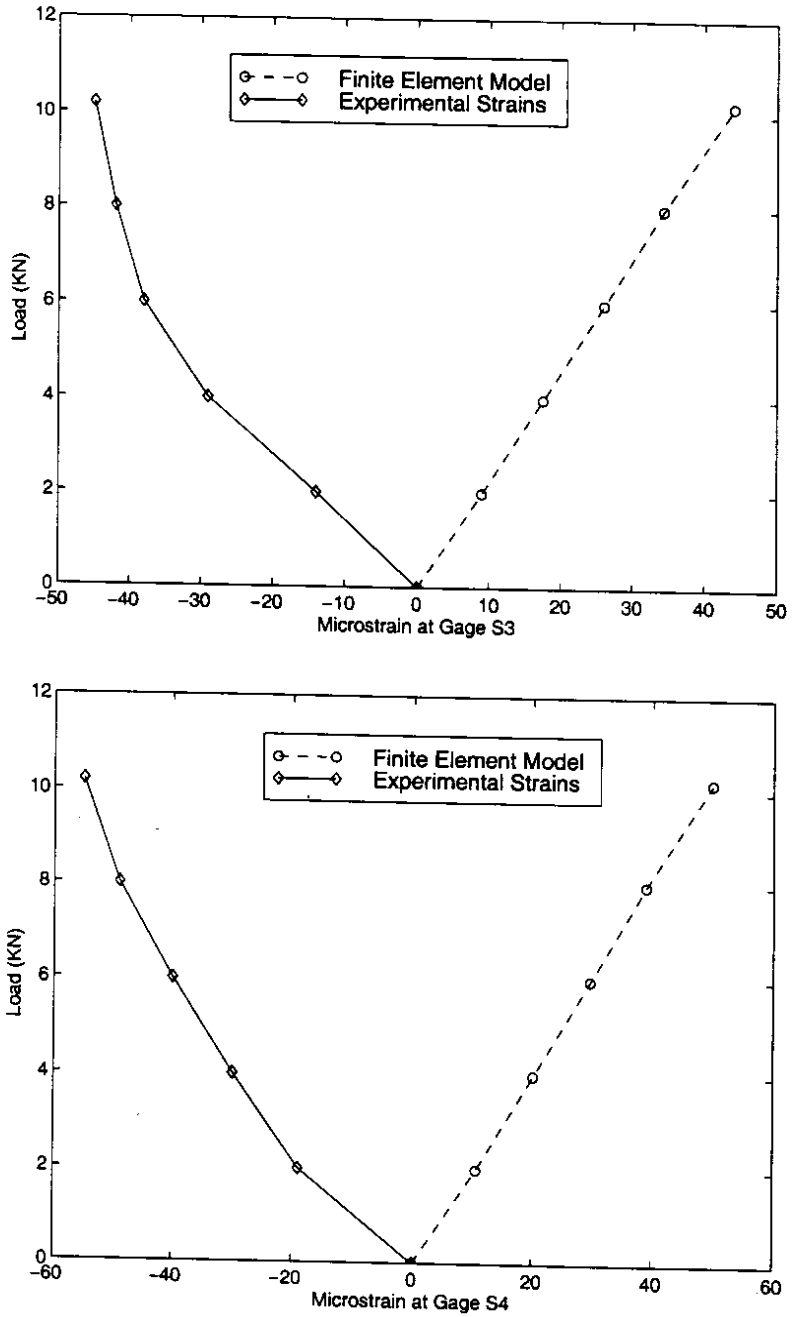

Figure 7.10: Strain Comparison for LSM-5

Chapter 8

Parametric Studies

8.1 Introduction

This Chapter presents two parametric studies on joint shear transfer effectiveness. The first study examines the effect of dowel looseness on pavement response; the second focuses on the changes in aggregate interlock shear transfer efficiency and pavement response due to variations in contraction joint opening. The intent of these studies is three-fold: (1) they illustrate the effectiveness of the proposed techniques for modeling dowel and aggregate interlock shear transfer; (2) they provide valuable information on the response of rigid pavements under applied wheel and thermal loadings due to realistic variations in joint shear transfer efficiency; (3) they indicate what future research needs are required to more completely model rigid pavement systems.

8.2 Description of Parametric Studies

8.2.1 Idealized System and Loads

Both the dowel and aggregate interlock parametric studies employ the same basic system shown in Fig. 8.1. For simplicity, the joint is not skewed, and the boundaries of the subgrade have not been extended beyond the edges of the slabs. The 150 mm thick base layer is assumed to be a compacted gravel, below which 300 mm of natural soil are modeled as a linearly elastic continuum. A dense liquid is used to represent the remaining natural soil with a modulus of 0.054 MPa/mm. The elastic material properties of the slab and soil are given in Table 8.1, where α is the coefficient of thermal expansion and ρ is the mass density. These values are typical of many designs [64].

Fig. 8.2 shows the layout of the dowels, which is consistent with a typical retrofit design by the Washington State Department of Transportation (WSDOT) and similar to those

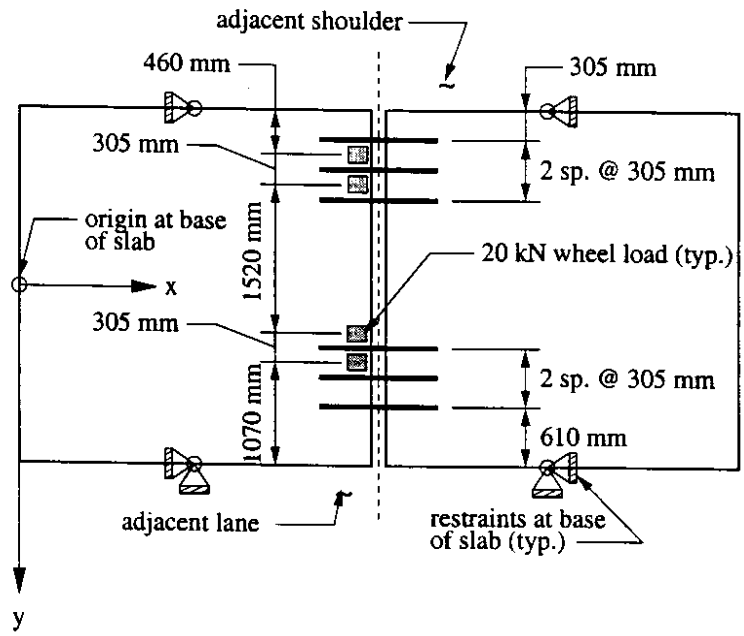

Figure 8.2: Plan View of Slabs Showing Dowels and Wheel Loads

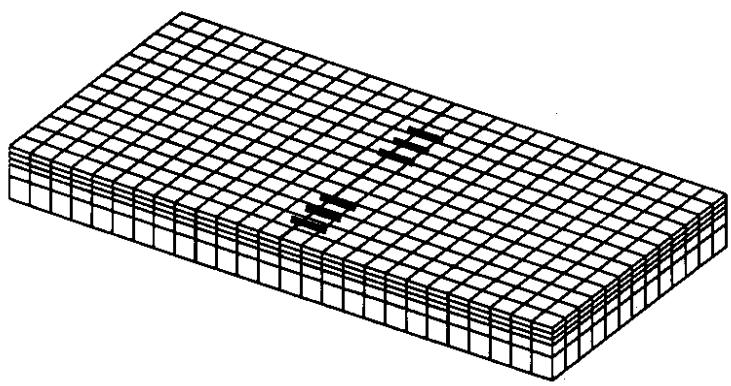

Mesh with 29721 degrees of freedom

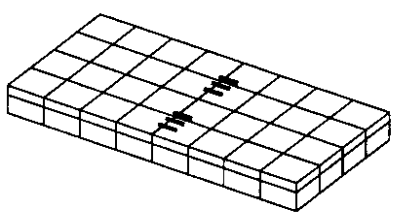

Mesh with 2439 degrees of freedom

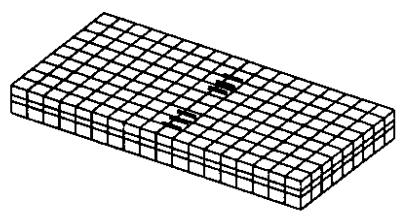

Mesh with 10617 degrees of freedom

Figure 8.3: Finite Element Meshes used in Parametric Study

magnitude of the gap at the joint face varies from 0 mm up to the value beyond which there is no significant effect on the pavement response. The number of elements in the region of the gap is fixed at three, giving six potential points of contact – note the nodal locations shown in 8.4. Recall that the convergence studies presented in Chapter 4 indicated that a total of six dowel elements in each slab, corresponding to three elements in the region of the gap, was sufficient to ensure convergence of displacements and dowel shears.

8.2.3 Model Details: Aggregate Interlock

This study examines the effect of initial joint opening, w, on aggregate interlock shear transfer. This is a very practical concern, as seasonal temperature changes can cause significant variations in w. The constitutive relations used to model aggregate interlock shear transfer across the joint are developed using a discretized version of Walraven's model as detailed in Chapter 5. The value of σ_{pu} was set at 45 N/mm^2, and $\mu = 0.4$. The fraction of aggregate particles in the concrete was fixed at 0.75, and a maximum particle diameter of 20 mm was assumed. The number of different embedments and diameters assumed in the analysis was 30. A total of 50 curves, each defined by 31 discrete points, was generated for constant crack openings of between 0.05 mm and 3.2 mm, with each curve capturing relative shear displacements between 0 mm and 1.0 mm. Plots of the shear and normal stresses corresponding to five selected values of crack opening are given in Fig. 8.5.

One modeling detail which must be addressed is the effect of the sawcut used to form rigid pavement contraction joints. As shown in Fig. 8.6, the upper quarter to third of the slab thickness is sawcut and filled with a joint sealant; as a result, there is no interlock shear transfer between slabs in this region. To properly model this phenomenon, the 16-noded interface element spanning the joint between the upper slab elements (covering the upper third of the slab thickness) is assigned a large initial joint opening and zero strength. Note that the 12.7 mm joint opening is artificial, and is only used to provide separation of the mesh between the slab faces.

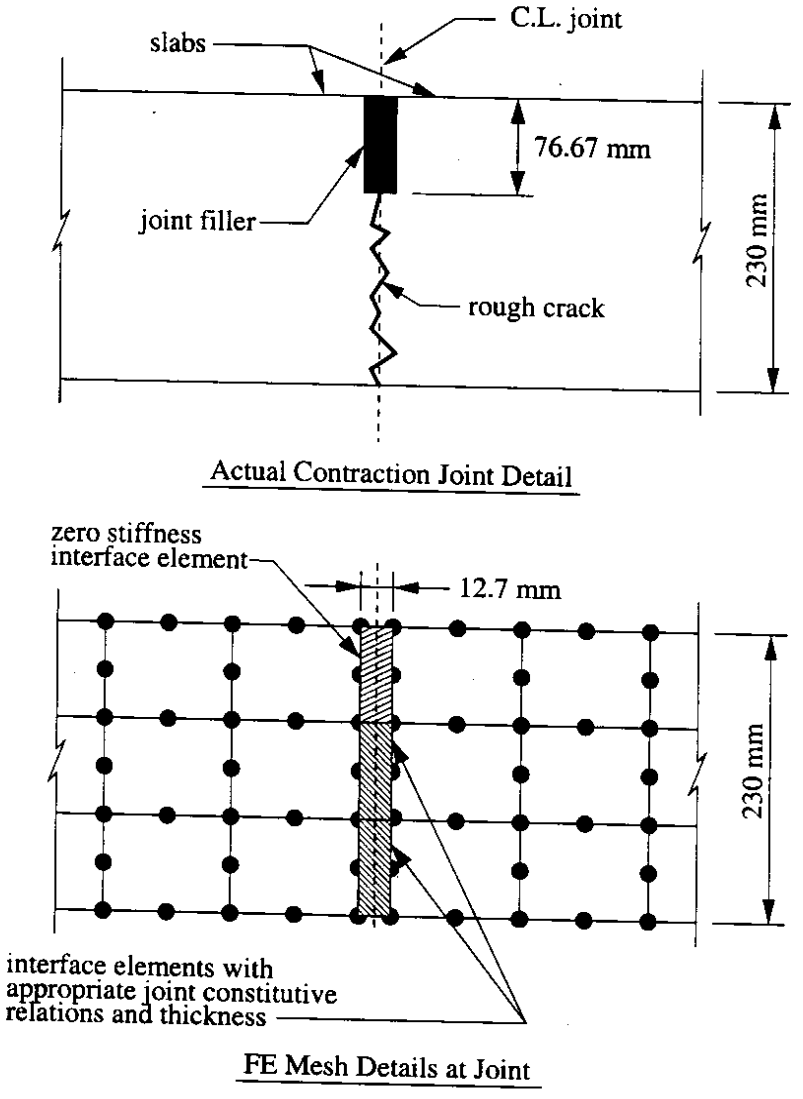

Figure 8.6: Aggregate Interlock Parametric Study: Detail of Joint

previously, so a smaller gap is required to produce the maximum decrease in LTE. Also note that the maximum reduction in LTE is about 37%, as opposed to 52% determined in Chapter 4. This difference can also be attributed to the different subgrade models. In the present model, as the loaded slab contacts the subgrade and displaces it downward, there is a loss of support under the unloaded slab. With a dense liquid directly below the slab as used in Chapter 4, the subgrade under the unloaded slab provides continuous support that is independent of the displacement of the loaded slab, tending to increase relative vertical displacements between the two slabs.

Figure 8.8 shows the displaced shape of the top surface of the slabs for selected values of the gap; the vertical displacement component has been scaled by a factor of 1000. Note the larger vertical displacements of the slab on the side where the wheel loads are closer to the edge. The vertical displacement of the loaded slab at $(x, y, z) = (3660, -1266.9, -230)$ varies from 0.56 mm for a gap of 0.00 mm to 0.64 mm for a gap of 0.12 mm; the corresponding vertical displacements at $(3660, 563.1, -230)$ vary from 0.48 mm to 0.55 mm.

8.3.2 Dowel Shears and Contact Forces

The loss in load transfer efficiency with gap is naturally paralleled by decreasing shear transfer due to dowel action. Fig. 8.9 details the change in shear transmitted across the joint for each dowel. Note the ineffectiveness of the dowel at $y = 1220$ mm, which is 610 mm from the nearest wheel load. For smaller gaps, the largest shears are transmitted by the dowel at $y = 610$ mm, which is centered between two wheels. This illustrates the localized nature of dowel shear transfer also noted by other researchers [41]. At larger values of γ, the dowel shears converge to nearly constant values with magnitudes ranging between about 0.7 kN and 2 kN.

It is also worthwhile to examine the nodal forces applied to the dowels by the surrounding slab for various values of γ. Figs. 8.10 through 8.13 provide this information for each dowel at selected values of γ; refer to Fig. 8.4 for the nodal locations corresponding to the x axis coordinates in Figs 8.10 through 8.13.

For $\gamma = 0.00$ mm, the largest contact forces occur at the joint face, and decrease rapidly in an oscillatory manner similar to a beam on elastic foundation. When $\gamma = 0.04$ mm, the point of contact is at the joint face for the loaded slab, but it has decreased significantly in magnitude; the portion of the dowel in the loaded slab sees more uniformly distributed contact along its length with smaller nodal forces. At $\gamma = 0.08$ mm, the contact forces are distributed over the dowel within both the unloaded and loaded slabs. As the gap increases

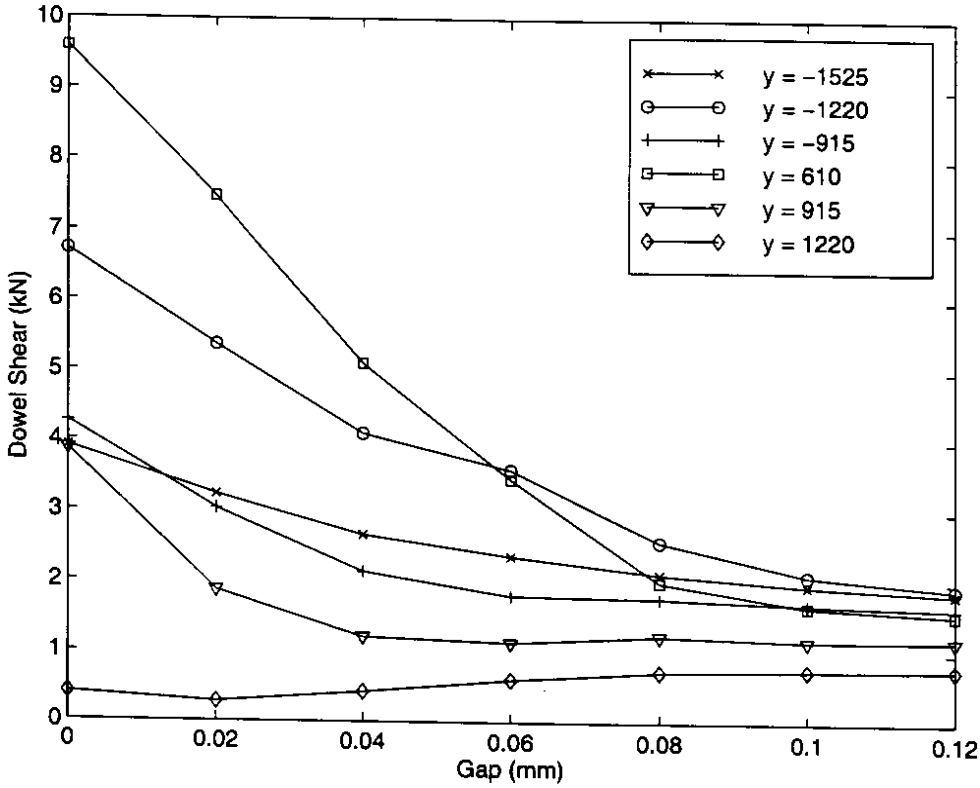

Figure 8.9: Dowel Shear vs. Gap – Axle Loading

to 0.12 mm, the points of contact are fewer and further back from the joint face, but the contact forces increase in magnitude vs. $\gamma = 0.08$ mm.

It must be noted that different shapes for the gap profile (i.e. linear, cubic, etc.) could be expected to produce significantly different contact patterns and forces. However, assuming that the formation of the gaps is due to degradation of the concrete surrounding the dowels under cyclic loading, and that the degradation is a function of the magnitude of the compressive stresses between the dowel and the slab, the assumption of a parabolic gap is not unreasonable given the oscillatory decrease in contact forces predicted when $\gamma = 0$ mm.

8.3.3 Slab and Subgrade Stresses

Given that increasing γ significantly decreases the dowel shears, we would expect an increase in subgrade stresses under the loaded slab adjacent to the joint with a concomitant decrease in subgrade stresses under the unloaded slab. Fig. 8.14 shows the magnitude of the vertical stress between the slab and subgrade for selected values of γ. Note the localized high stresses under the edge of the loaded slab for all values of the gap. As γ increases, the unloaded slab transfers less load to the subgrade, and the region of separation between the unloaded

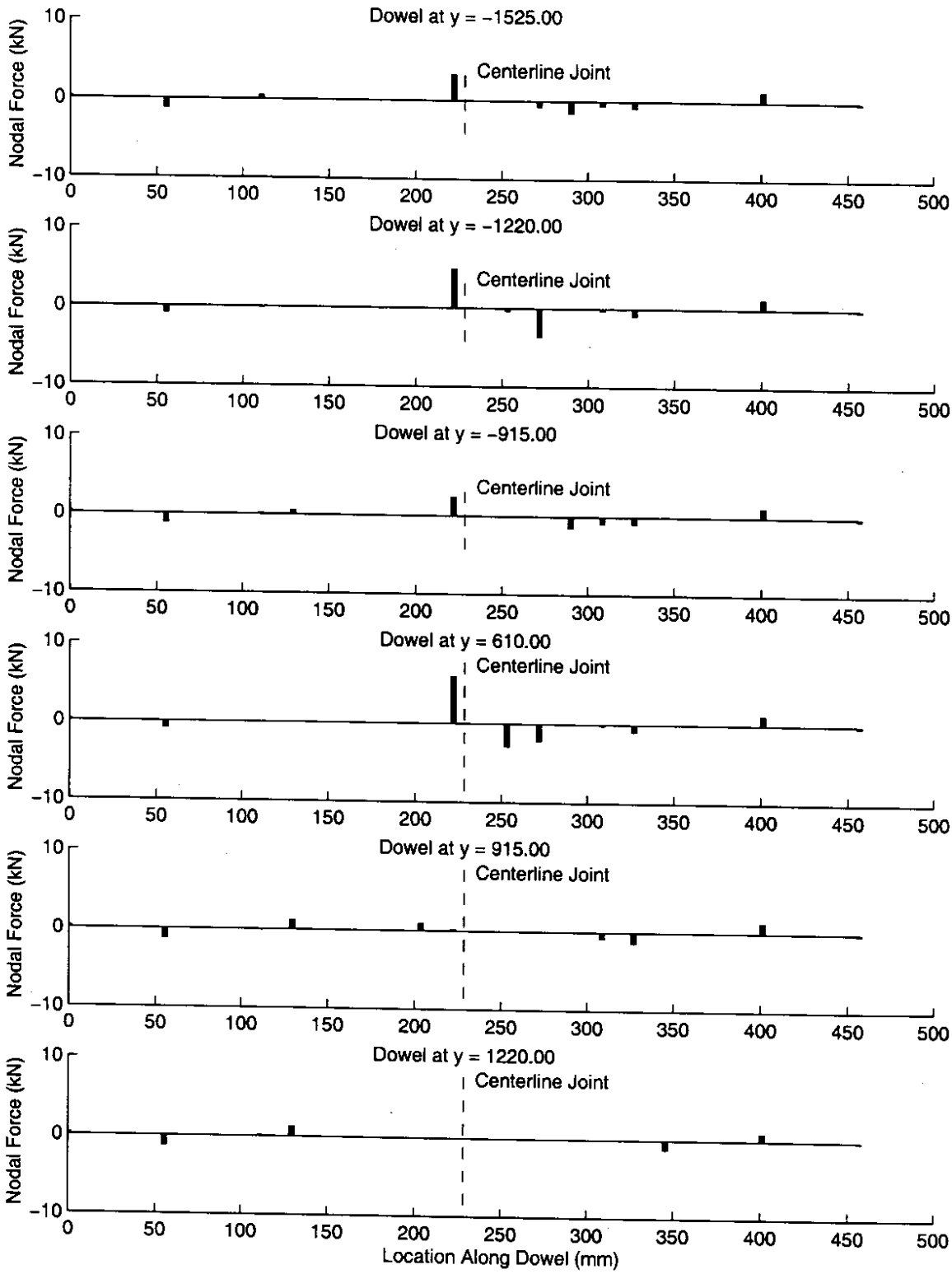

Figure 8.11: Nodal Forces on Dowels for 0.04 mm Gap – Axle Loading

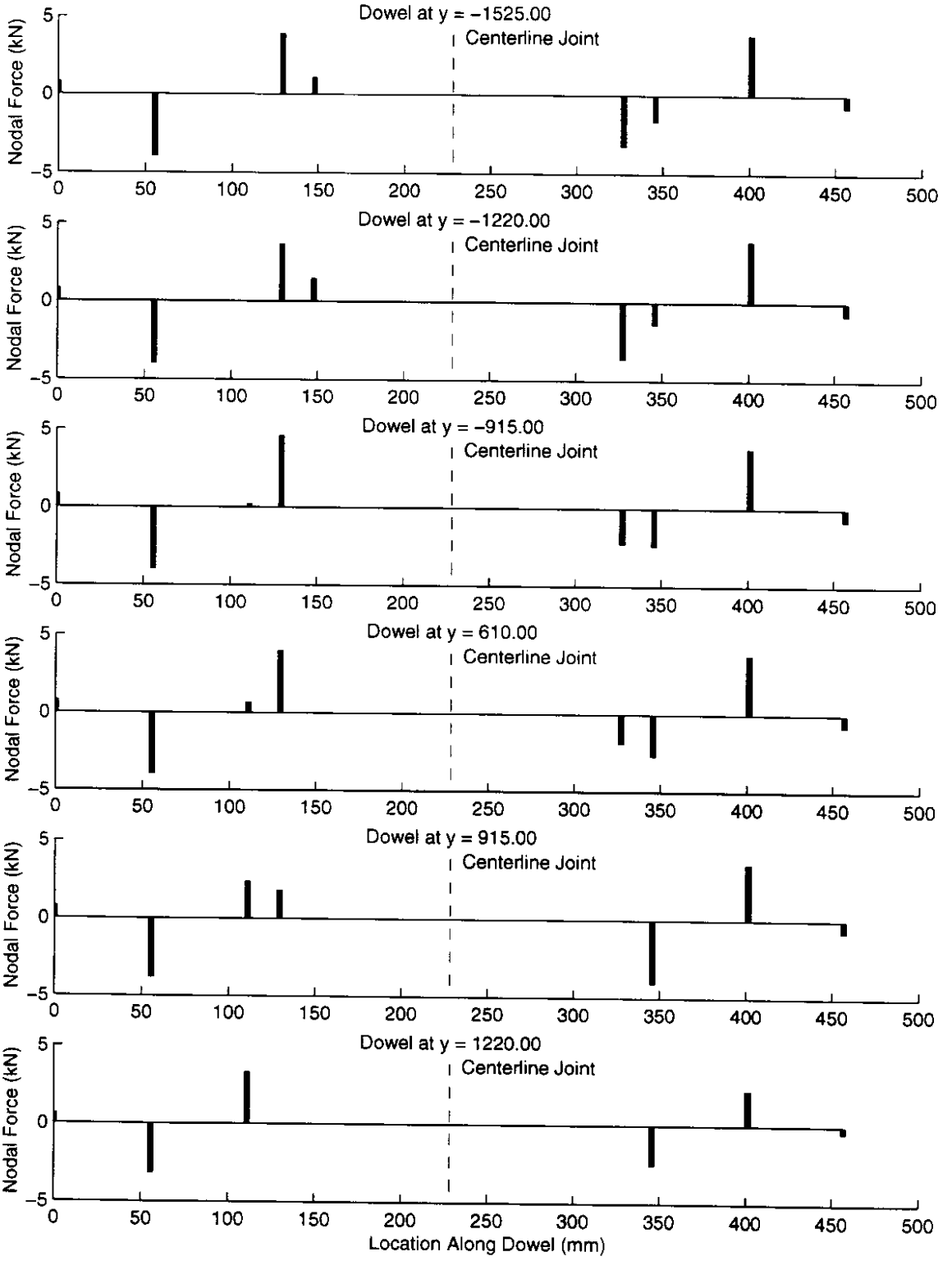

Figure 8.13: Nodal Forces on Dowels for 0.12 mm Gap – Axle Loading

slab and subgrade increases as evidenced by larger regions of zero or near-zero stresses. The maximum stress applied to the subgrade by the loaded slab varies from 107 kPa to 180 kPa as the gap varies from 0.00 mm to 0.12 mm - an increase of 68%. It must be noted that these stress values are somewhat unrealistic due to the likelihood of subgrade yielding which is not captured by the linearly elastic model. However, the fact that they increase dramatically with the presence of small values of γ is significant: as detailed in Chapter 1, loss of subgrade support and strength due to pumping action and subgrade deterioration under high stresses is suspected of being a significant component of many joint failures [46].

It is also illuminating to examine the principal tensile stresses in the bottom of the slab, as they increase significantly with increasing gaps. Figure 8.15 shows the maximum principal stresses on the bottom of the slab, with the maximum values occuring under each dual wheel at the joint face. The maximum values vary from 667 kPa to 1037 kPa with gaps of between 0.00 mm and 0.12 mm, an increase of 55%. The orientation of the maximum principal stress is in the y direction (transverse): effectively, as γ grows and the unloaded slab provides less support to the loaded slab, the stresses in the loaded slab approach those due to an unprotected edge loading condition.

8.4 Results: Aggregate Interlock, Axle Loading

8.4.1 Displacement Response

A similar relationship between LTE and joint opening, w, for an undoweled joint with aggregate interlock exists as between LTE and γ for a doweled joint. As w increases, the effectiveness of aggregate interlock as a shear transfer mechanism is reduced, leading to smaller LTEs as shown in Fig. 8.16. The values of w observed in practice do not typically reach 3.20 mm (the maximum value assumed in this study). The following equation is often used to predict joint opening, ΔL [60, 93]:

$$\Delta L = DL(\alpha \Delta T + \epsilon) \tag{8.1}$$

where D = adjustment factor for slab-subgrade friction (0.8 for gravel base layers), L = the transverse joint spacing (3660 mm), ΔT = the uniform change in temperature, and ϵ = strain due to drying shrinkage (typically 1.5×10^{-04}). For the present study, assuming a reasonable value for ΔT of 35°C, Eq. 8.1 gives ΔL = 1.6 mm. Fig. 8.16 indicates that a maximum seasonal change in LTE would be approximately 50%.

The global displacement response of the undoweled system is illustrated in Fig. 8.17,

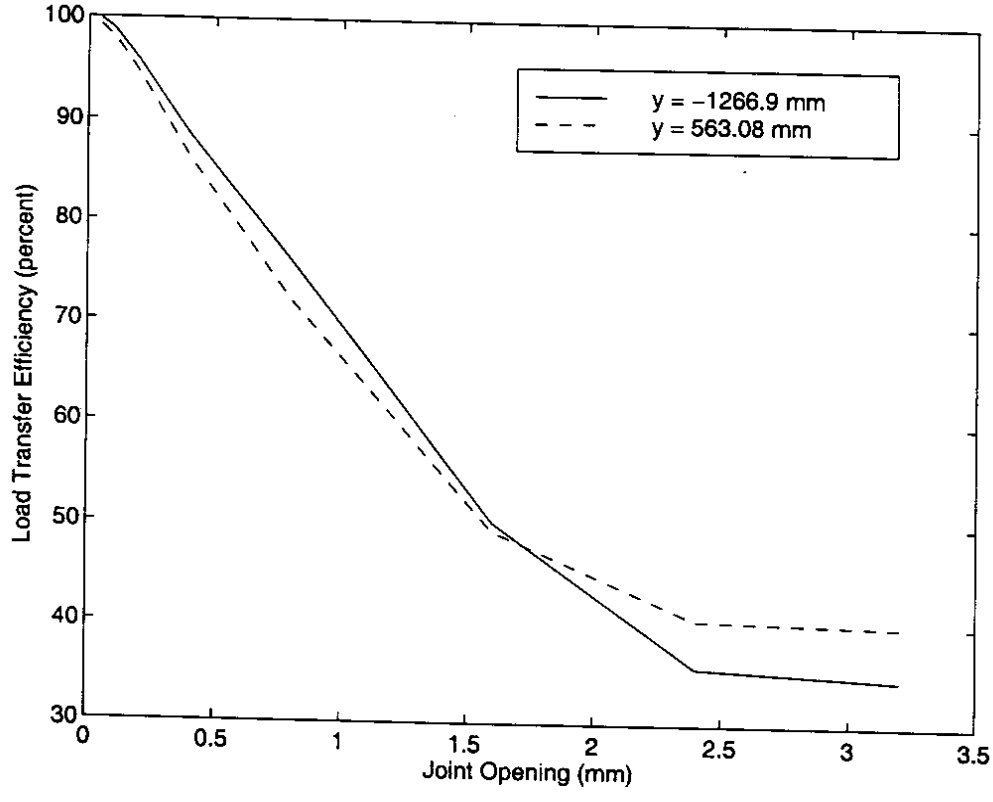

Figure 8.16: Load Transfer Efficiency vs. Joint Opening – Undoweled Joint, Axle Loading

which depicts the displaced shape of the top surface of the slabs for selected values of w. Note the growing discrepancy between the vertical displacements of the loaded and unloaded slabs at the joint with increasing w.

8.4.2 Aggregate Interlock Stresses on Joint Faces

It is particularly interesting to examine the distribution of shear stresses on the joint faces arising from aggregate interlock as shown in Fig. 8.18 for different values of w. The shear stresses are negative, as they are shown acting on the vertical joint face of the loaded slab; of course, identical stresses in the opposite direction exist on the face of the unloaded slab. Note the region of zero and near-zero stresses in the upper third as required by the sawcut detailed in Fig. 8.6; the small non-zero stresses are artifacts of the smoothing and nodal averaging of stresses and subsequent quadratic interpolation within elements. As with dowel joint shear transfer, aggregate interlock shear transfer is a highly localized phenomenon, with only the portions of the joint faces nearest the wheels seeing significant stress. At large joint openings, the shear stresses acting on the joint face are effectively zero, and the unloaded slab provides no support for the loaded slab as shown in Fig. 8.17. The

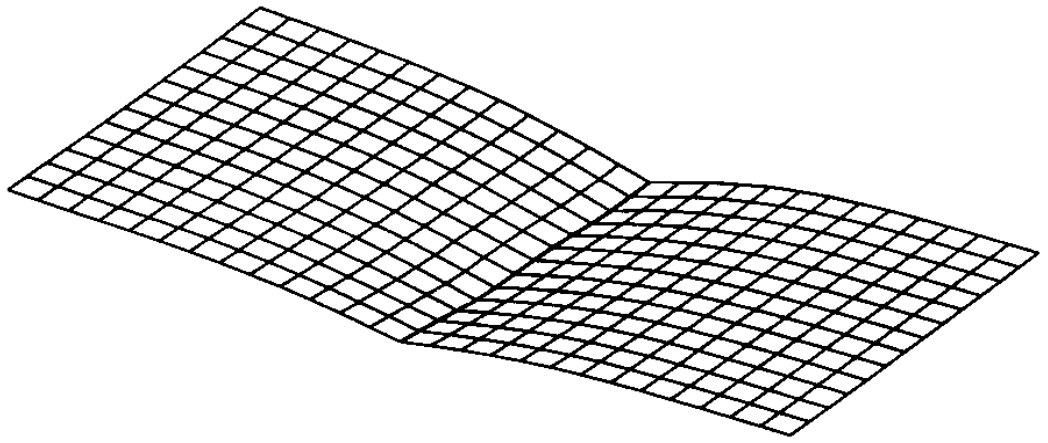

Joint Opening = 0.05 mm

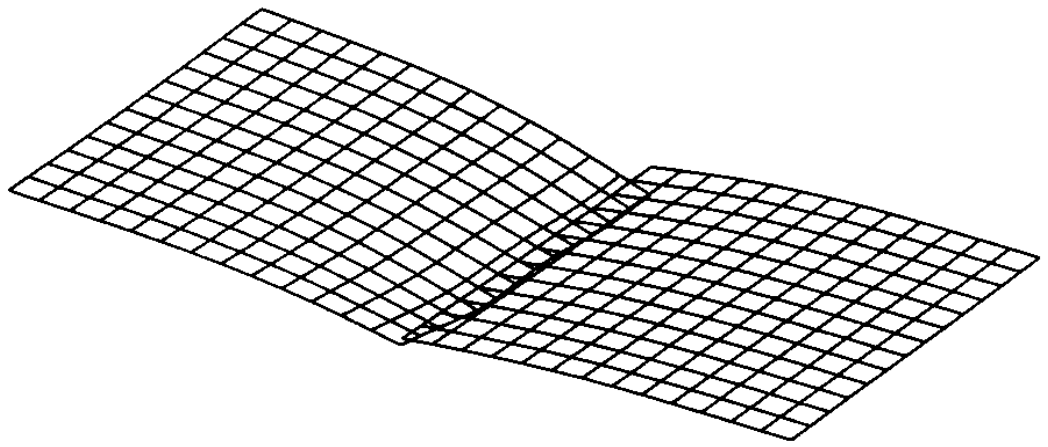

Joint Opening = 1.60 mm

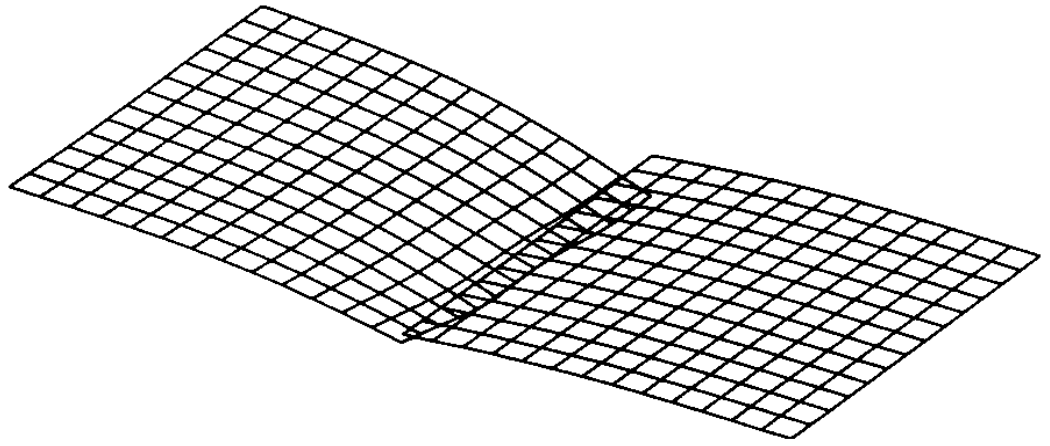

Joint Opening = 3.20 mm

Figure 8.17: Displaced Shape of Top of Slab – Undoweled Joint. Axle Loading

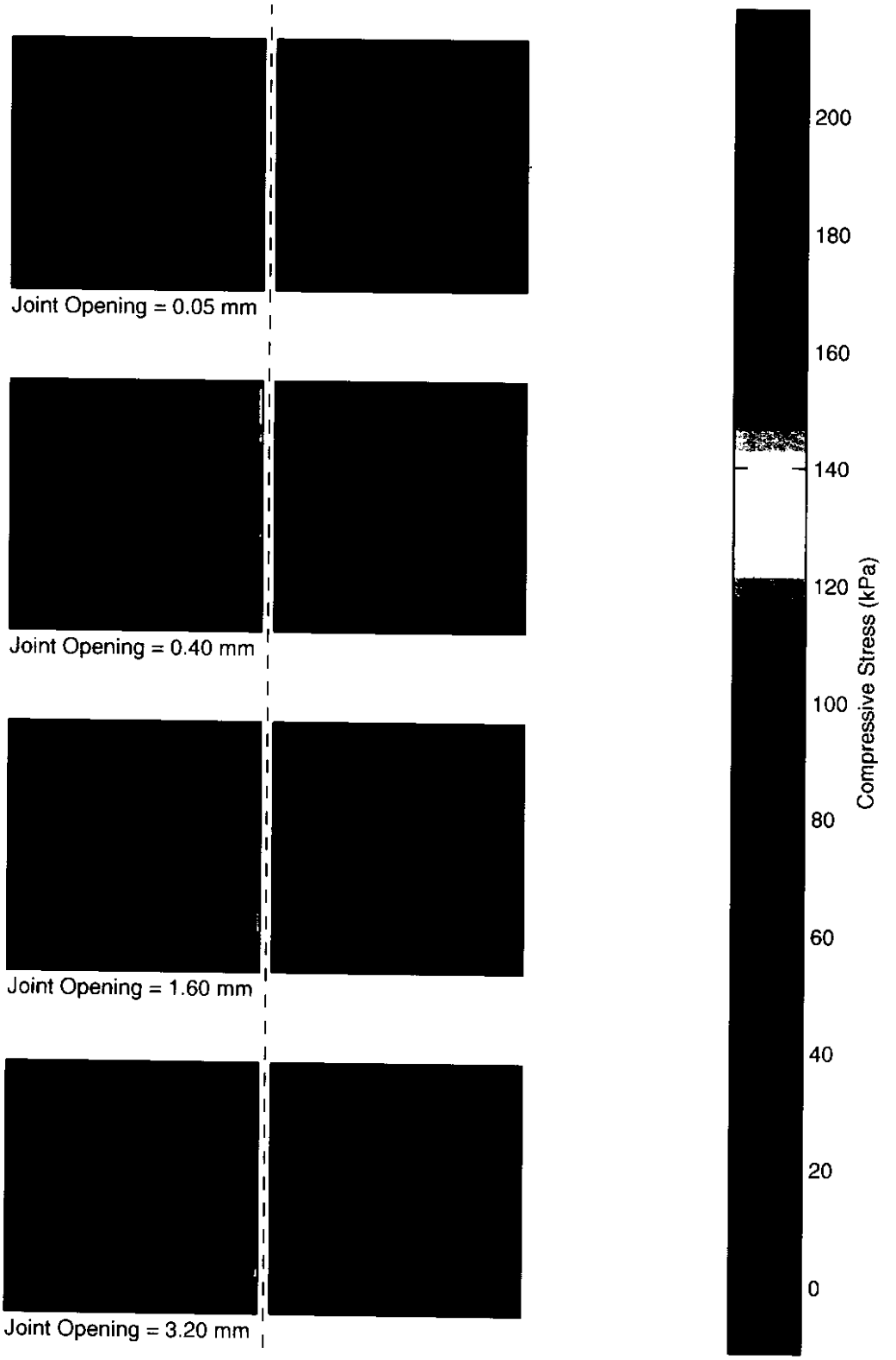

Figure 8.19: Vertical Stress on Top of Base Layer – Undoweled Joint, Axle Loading

8.5 Results: Doweled Joint, Axle and Temperature Loading

8.5.1 Displacement Response

Similar to the case of axle loading only, the relative vertical displacements of the two slabs near the joint grow with increasing γ. The maximum value assumed for γ was 0.24, beyond which there is not a significant change in the model response. When computing the LTE, the displacements due to temperature and self-weight alone were determined from separate analyses and subtracted from the displacements due to self-weight, temperature, and axle loading. As for axle loading alone, the LTE has been plotted at $(x, y, z) = (3660, -1266.9, -230)$ and $(3660, 563.1, -230)$, which correspond to the nodes closest to the center of each dual wheel load (see Fig. 8.21). Figure 8.22 shows the displaced shape of the top surface of the slabs for selected values of the gap; the vertical displacement component has been scaled by a factor of 1000.

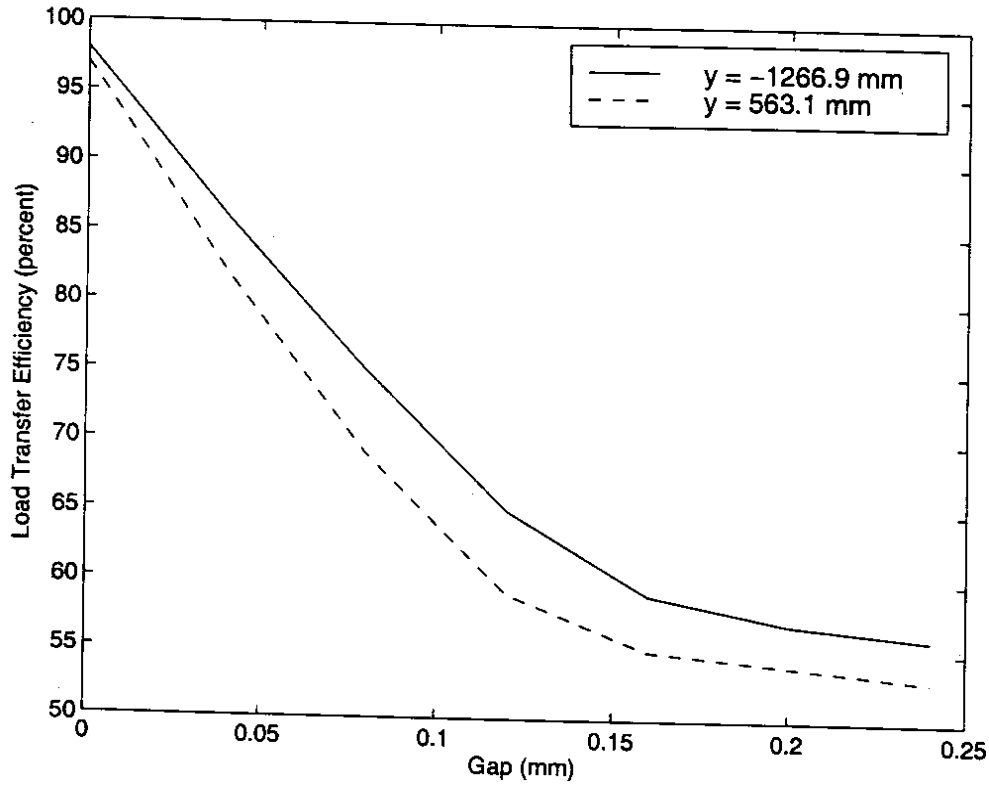

Figure 8.21: Load Transfer Efficiency vs. Gap – Axle and Temperature Loading

8.5.2 Dowel Shears and Contact Forces

The dowel shears follow much the same pattern with respect to dowel location observed for axle loading only, but with increased magnitudes as shown in Fig. 8.23. This increase in dowel shears is due to the fact that under temperature loading, the slab and base separate and less of the axle load is transferred to the subgrade in the immediate vicinity of the wheels. These larger dowel shears translate into generally larger contact forces between the

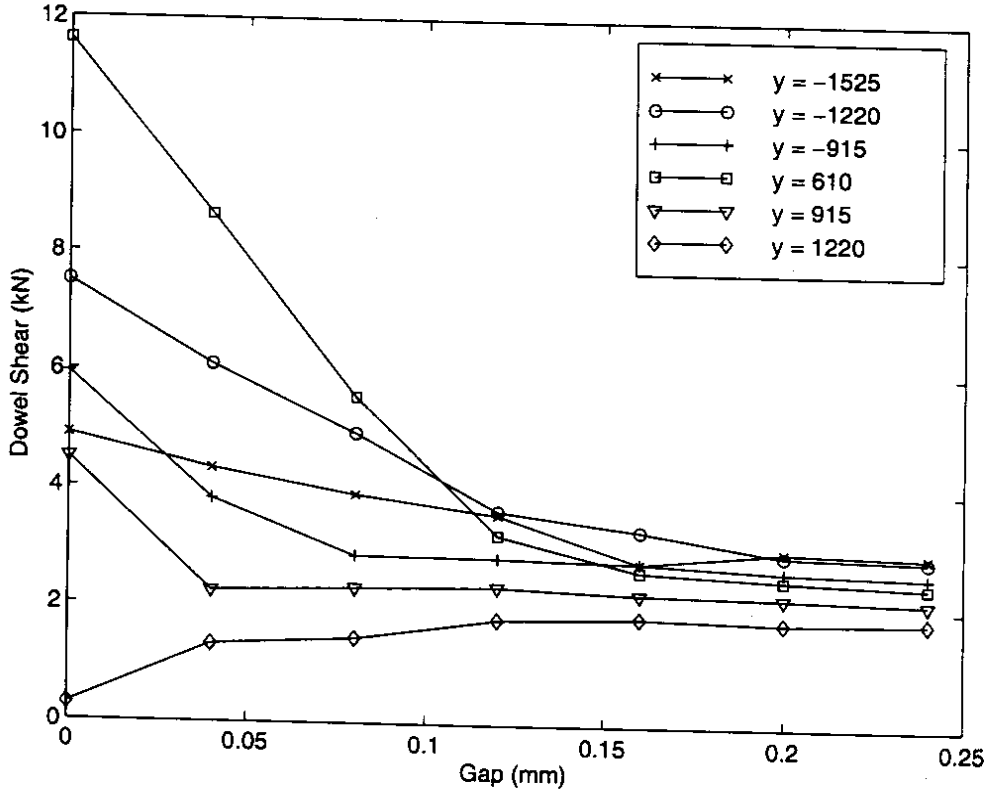

Figure 8.23: Dowel Shear vs. Gap – Axle and Temperature Loading

dowel and the surrounding slab as illustrated in Figs. 8.24 through 8.27.

8.5.3 Slab and Subgrade Stresses

Fig. 8.21 shows increasing LTE with increasing γ, and Fig. 8.22 illustrates the tendency of the loaded slab to "tip" in the direction of the joint for larger values of γ. This results in different contact regions between the slab and subgrade and increasing contact stresses as illustrated in Fig. 8.28. In fact, the maximum stress applied to the base layer varies from 34 kPa to 104 kPa as γ increases from 0.00 mm to 0.24 mm, an increase of 206%. These stresses are still significantly lower than those observed for axle loading only, however.

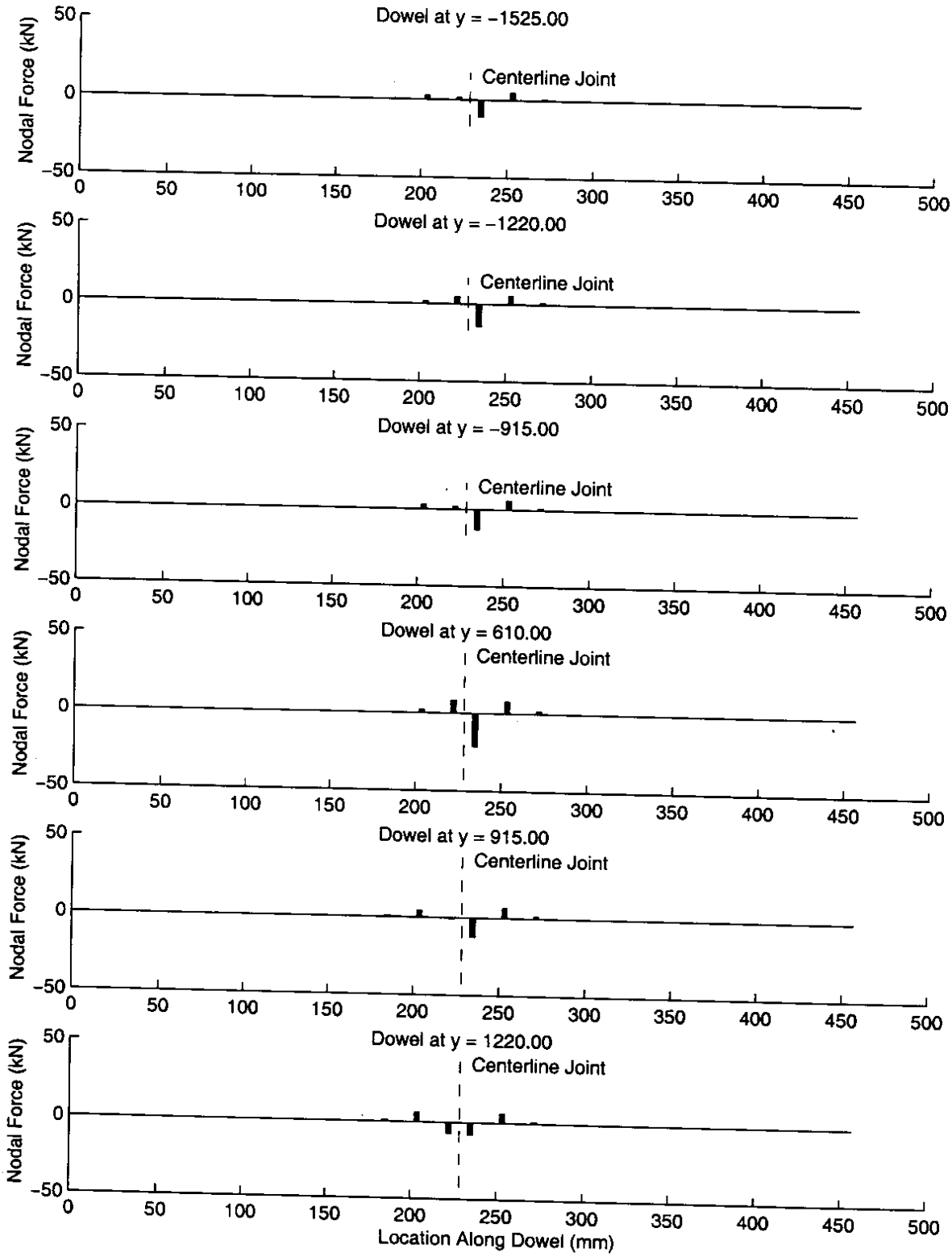

Figure 8.24: Nodal Forces on Dowels for 0 mm Gap - Axle and Temperature Loading

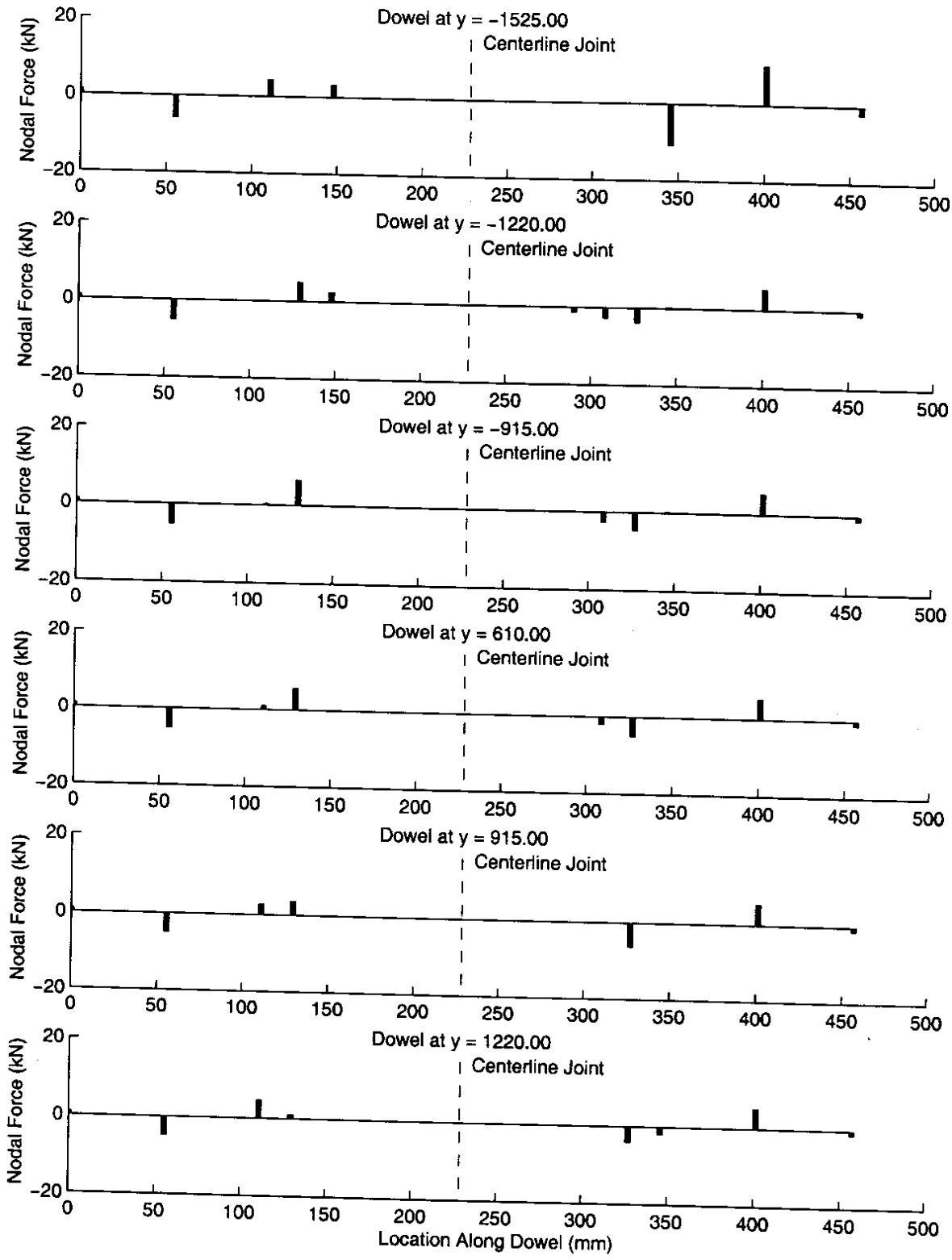

Figure 8.26: Nodal Forces on Dowels for 0.16 mm Gap – Axle and Temperature Loading

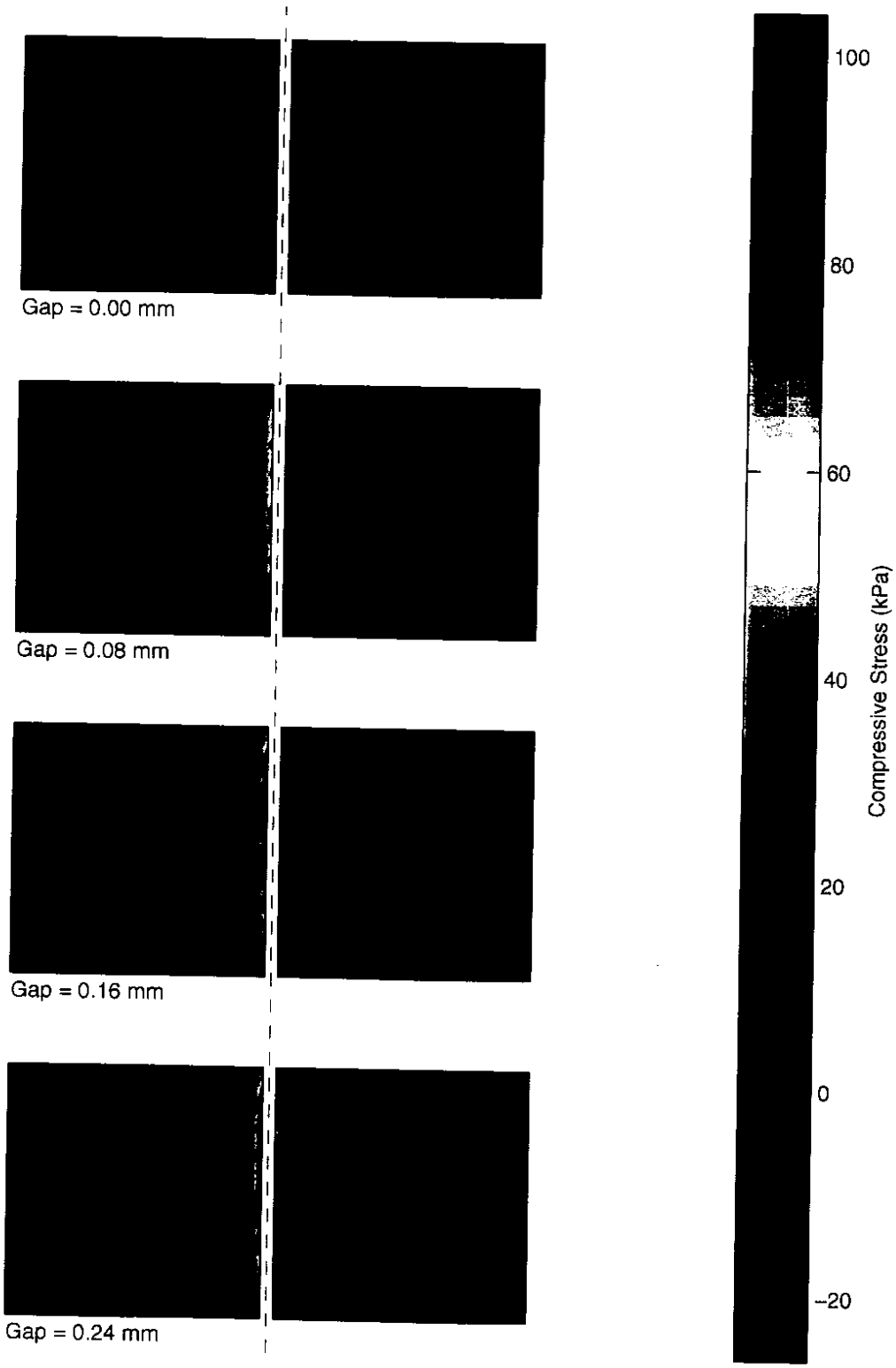

Figure 8.28: Vertical Stress on Top of Base Layer – Doweled Joint, Axle and Temperature Loading

8.6 Summary

This Chapter presented two parametric studies on joint shear transfer effectiveness. The first study examined the effect of dowel looseness on pavement response; the second study focused on the effect of the variation in initial joint opening on aggregate interlock shear transfer effectiveness. Axle loading was considered in both studies, while axle loading combined with a negative temperature gradient was also considered for the doweled model.

It was shown that small values of dowel looseness (gaps between the dowel and the slab of less than 0.12 mm) and typical seasonal variations in initial undoweled joint opening (less than 1.60 mm) can have large effects on pavement response to axle loads near the joint, with losses in joint shear transfer efficiency of up to 50% and significant increases in the slab tensile stresses. Perhaps more important, however, is the large increase in vertical stress applied to the subgrade by the loaded slab near the joint as joint shear transfer effectiveness decreases. This indicates significant potential for subgrade yielding and degradation under repeated loading, which could hasten the development of joint damage and faulting.

Under the action of combined temperature and wheel loading, gaps between the dowels and the slabs resulted in relatively modest increases in tensile stresses on top of the slabs. However, the displacement response of the system varied significantly with differing amounts of joint shear transfer. The models captured these effects quite well, illustrating the variations in slab/subgrade separation and differential joint displacements with dowel looseness.

Based on these studies, it appears that both dowel looseness and aggregate interlock nonlinearities due to commonly experienced joint openings can have large effects on the response of rigid pavement systems. The finite element models used in this study are capable of capturing these variations in response, making them valuable tools for the evaluation of existing and proposed design configurations under a variety of loadings. Several areas of future research can also be identified based on these studies, including the formation of dowel looseness and reduction of aggregate interlock load transfer due to cyclic loading, and the development of better base/subgrade models that capture soil yielding and damage under high localized stresses.

requirements.

These specific shortcomings were addressed in the development of modeling techniques and the simulations of this study.

- Multiple-slab systems of various geometries were considered. The slabs were considered as linearly elastic.
- The inclusion of multiple and debonded linearly elastic base layers was addressed.
- The models included accurately located rectangular and circular tire contact areas as well as linear temperature gradients through the slab thickness.
- Dowels were located precisely, and debonding and dowel looseness were considered explicitly.
- A two-phase model for aggregate interlock was implemented, permitting the effects of joint opening and concrete properties to be captured.
- Efficient iterative solution strategies for large-scale systems involving material and contact nonlinearities were developed and thoroughly tested.

To test the accuracy and applicability of the proposed finite element models developed in this study, a comparison of deflection and strain data with measured values from a recent laboratory study was done [33]. In particular, doweled two-slab systems subjected to corner loading were analyzed: the first model rested directly on a rubber pad (idealized as a dense liquid), the second on an unbonded cement treated base above the rubber pad. To capture the relative vertical displacements at the joint observed for both systems, a small gap was assumed to exist around the embedded portion of the dowels in the unloaded slab; this assumption was deemed reasonable based on the methods of construction. Displacement basin comparisons were reasonably accurate with excellent agreement near the joint, verifying dowel looseness as a potential cause of the observed relative joint displacements. Strain comparisons were less accurate, but reasonable agreement between measured and computed values was observed for the first test. Strain comparisons for the second test were inconclusive, with no obvious explanation.

To illustrate the applicability of the aggregate interlock and dowel modeling techniques, a series of parametric studies of a typical rigid pavement system was conducted. The system studied consisted of two rigid pavement slabs on a gravel base layer; dowel locations were based on a typical retrofit design configuration used by the Washington State Department

with normal and tangential joint displacements. Particularly significant is the large variation in shear transfer with joint opening, which may undergo significant seasonal changes. The aggregate interlock model was implemented using a sixteen-noded quadratic interface element that displaces compatibly with the solid elements it is meshed between.

- *Solution strategies.* A solution strategy appropriate for the analysis of large-scale structural systems incorporating spatially varying or nonlinear materials and contact nonlinearities was developed. A significant feature of this solution strategy is a multigrid preconditioner that permits the use of unstructured/unnested mesh sequences. General restriction and interpolation operators that rely on the evaluation of element shape functions were developed that permit multiple isoparametric element types and varying nodal degrees of freedom. These multigrid methods permit the coarse mesh stiffness matrices to be assembled in the usual fashion even in the presence of spatially varying materials with sharp boundaries, greatly simplifying implementation.

9.3 Future Work

While this study has made significant contributions to the finite element modeling of rigid pavement systems, there are several areas that would benefit from further research.

9.3.1 Formation of Dowel Looseness

The ability to predict the formation of gaps between the dowels and surrounding slab would be a particularly important topic of future research. One prior experimental study has shown this to occur under repeated load cycles [10], but at present a predictive analytical model does not exist. Prediction of long-term joint response and a better understanding of the associated mechanics of dowel-slab interaction would aid new design efforts as well as assist in the development of retrofit strategies and associated life-cycle cost analyses. This would require the development of constitutive relations that relate cumulative damage to repeated application of bearing stresses between the dowel and concrete and local finite element models incorporating these constitutive models in the regions around the dowels.

Once a viable and realistic dowel looseness prediction model has been developed, back-calculation of in-situ looseness of doweled joints might be possible. Ideally, such an evaluation would rely on standard non-destructive tests. Once the in-situ properties have been determined, the damage model could be used to predict remaining joint life.

Bibliography

[1] *The AASHO Road Test - Pavement Research.* Special Report 61E, Highway Research Board, 1962.

[2] AASHTO. *Guide for Design of Pavement Structures*, 1988.

[3] M.G. Abdel-maksoud, N. Hawkins, and E. Barenberg. Behavior of Concrete Joints under Cyclic Shear. In *Aircraft/Pavement Technology: In the Midst of Change*, pages 190–204. ASCE, 1997.

[4] S.F. Ashby and R.D. Falgout. A Parallel Multigrid Preconditioned Conjugate Gradient Algorithm for Groundwater Flow Simulations. *Nuclear Science and Engineering*, 124:145–159, 1996.

[5] F. Barzegar and S. Maddipudi. Generating Reinforcement in FE Modeling of Concrete Structures. *Journal of Structural Engineering*, 120(5):1656–1662, 1994.

[6] K.-J. Bathe. *Finite Element Procedures.* Prentice-Hall, Inc., 1996.

[7] Z.P. Bažant and P. Gambarova. Rough Cracks in Reinforced Concrete. *Journal of the Structural Division, ASCE*, 106(ST4):819–842, 1980.

[8] A. Brandt. Multi-Level Adaptive Solutions to Boundary-Value Problems. *Mathematics of Computation*, 31(138):333–390, 1977.

[9] D.R. Brill, G.F. Hayhoe, and X. Lee. Three-Dimensional Finite Element Modeling of Rigid Pavement Structures. In *Aircraft/Pavement Technology: In the Midst of Change*, pages 151–165. ASCE, 1997.

[10] Neeraj Buch and Dan G. Zollinger. Development of Dowel Looseness Prediction Model for Jointed Concrete Pavements. In *Transportation Research Record 1525*, pages 21–27, Washington, D.C., 1996. TRB, National Research Council.

[23] M.N. Fardis and O. Buyukozturk. Shear Transfer Model for Reinforced Concrete. *Journal of Engineering Mechanics*, 105(EM2):255–275, 1979.

[24] C. Farhat and N. Sobh. A Coarse/Fine Mesh Preconditioner for Very Ill-Conditioned Finite Element Problems. *International Journal for Numerical Methods in Engineering*, 28:1715–1723, 1989.

[25] P.H. Feenstra, R. Boorst, and J.G. Rots. Numerical Study on Crack Dilatancy. I: Models and Stability Analysis. *Journal of Engineering Mechanics*, 117(4):733–753, 1991.

[26] P.H. Feenstra, R. Boorst, and J.G. Rots. Numerical Study on Crack Dilatancy. II: Applications. *Journal of Engineering Mechanics*, 117(4):754–769, 1991.

[27] J. Fish, L. Pan, V. Belsky, and S. Gomaa. Unstructured Multigrid Method for Shells. *International Journal for Numerical Methods in Engineering*, 39:1181–1197, 1996.

[28] B.F. Friberg. Design of Dowels in Transverse Joints of Concrete Pavements. *Proceedings of the ASCE*, 64(9), 1938.

[29] G.H. Golub and C.F. Van Loan. *Matrix Computations.* The Johns Hopkins University Press, 1989.

[30] J. E. Goodman and J. O'Rourke. *Handbook of Discrete and Computational Geometry.* CRC, 1997.

[31] H. Guo, J.A. Sherwood, and M.B. Snyder. Component Dowel-Bar Model for Load Transfer Systems in PCC Pavements. *Journal of Transportation Engineering*, 121(3):289–298, 1995.

[32] K. T. Hall, M. I. Darter, and J. M. Armaghani. Performance Modeling of Joint Load Transfer Restoration. In *Transportation Research Record 1388*, pages 129–139, Washington, D.C., 1993. TRB, National Research Council.

[33] Michael I. Hammons. Development of an Analysis System for Discontinuities in Rigid Airfield Pavements. Technical Report GL-97-3, US Army Corps of Engineers, Apr. 1997.

[46] A.M. Ioannides, Y.-H. Lee, and M.I. Darter. Control of Faulting Through Joint Load Transfer Design. In *Transportation Research Record 1286*, pages 49–56, Washington, D.C., 1992. TRB, National Research Council.

[47] D.C. Jesperson. Multigrid Methods for Partial Differential Equations. In G.H. Golub, editor, *MAA Studies in Mathematics*, volume 24, pages 270–317, 1984.

[48] Jong keun Choi and Jang keun Lim. General Curved Beam Elements Based on the Assumed Strain Fields. *Computers and Structures*, 55(3):379–386, 1995.

[49] J. Kim, K.D. Hjelmstat, and Q.H. Zuo. Three-Dimensional Finite Element Study of Wheel Load Interaction. In *Aircraft/Pavement Technology: In the Midst of Change*, pages 138–150. ASCE, 1997.

[50] M. Kŏcvara. An Adaptive Multigrid Technique for Three-Dimensional Elasticity. *International Journal for Numerical Methods in Engineering*, 36:1703–1716, 1993.

[51] T. Krauthammer, N. Bazeos, and T.J. Holmquist. Modified SDOF Analysis of RC Box-type Structures. *Journal of Structural Engineering*, 112(4):726–744, 1986.

[52] T. Krauthammer and K.L. Western. Joint Shear Transfer Effects on Pavement Behavior. *Journal of Transportation Engineering*, 114(5):505–529, 1988.

[53] A.R. Kukreti, M.R. Taheri, and Ragnar H. Ledesma. Dynamic Analysis of Rigid Airport Pavements with Discontinuities. *Journal of Transporation Engineering*, 118(3):341–360, 1992.

[54] C.-M. Kuo, K.T. Hall, and M.I. Darter. Three-Dimensional Finite Element Model for Analysis of Concrete Pavement Support. In *Transportation Research Record 1505*, pages 119–127, Washington, D.C., 1996. TRB, National Research Council.

[55] J.P. Laible, R.N. White, and P. Gergely. Experimental Investigation of Seismic Shear Transfer Across Cracks in Concrete Nuclear Containment Structures. In *Reinforced Concrete Structures in Seismic Zones*, ACI Special Publication SP-53, pages 203–226, Detroit, Mi., 1977. American Concrete Institute.

[56] B. Li, K. Maekawa, and H. Okamura. Contact Density Model for Stress Transfer across Cracks in Concrete. *Journal of the Faculty of Engineering, the University of Tokyo*, 40(1):9–52, 1989.

[68] C.W. Oosterlee and Y. Washio. An Evaluation of Parallel Multigrid as a Solver and A Preconditioner for Singularly Perturbed Equations. *SIAM Journal on Scientific Computing*, 19(1):87–110, 1998.

[69] I.D. Parsons, I.-S. Eom, and K.D. Hjelmstad. Numerical Simulations of Load Transfer Between Doweled Pavement Slabs. In *Aircraft/Pavement Technology: In the Midst of Change*, pages 166–177. ASCE, 1997.

[70] I.D. Parsons and J.F. Hall. The Multigrid Method in Solid Mechanics: Part I - Algorithm Description and Behavior. *International Journal for Numerical Methods in Engineering*, 29:719–737, 1990.

[71] I.D. Parsons and J.F. Hall. The Multigrid Method in Solid Mechanics: Part II - Practical Applications. *International Journal for Numerical Methods in Engineering*, 29:739–753, 1990.

[72] G. Prathap and G.R. Byashyam. Reduced Integration and the Shear-Flexible Beam Element. *International Journal for Numerical Methods in Engineering*, 18:195–210, 1982.

[73] J.S. Przemieniecki. *Theory of Matrix Structural Analysis.* McGraw-Hill, Inc., 1968.

[74] H.W. Reinhardt and J.C. Walraven. Cracks in Concrete Subject to Shear. *Journal of the Structural Division, ASCE*, 108(ST1):207–224, 1982.

[75] W.J. Rider and D.A. Knoll. Solving Nonlinear Heat Conduction Problems with Multigrid Preconditioned Newton-Krylov Methods. Technical Report LA-UR-97-2929, Los Alamos National Lab., Feb. 1997.

[76] M.D. Rucki. *An Algorithmic Framework for Flexible Finite Element Modelling.* PhD thesis, The University of Washington, May 1996.

[77] Y. Saad. *Iterative Methods for Sparse Linear Systems.* PWS Publishing Co., Boston, MA, 1996.

[78] G. Sathurappan, N. Rajagopalan, and C.S. Krishnamoorthy. Nonlinear Finite Element Analysis of Reinforced and Prestressed Concrete Slabs with Reinforcement (Inclusive of Prestressing Steel) Modelled as Discrete Integral Components. *Computers and Structures*, 44(3):575–584, 1992.

Transportation Research Record 1482, pages 26–32, Washington, D.C., 1996. TRB, National Research Council.

[91] J.C. Walraven. Fundamental Analysis of Aggregate Interlock. *Journal of the Structural Division, ASCE*, 107(ST11):2245–2270, 1981.

[92] J.C. Walraven. Rough Cracks Subjected to Earthquake Loading. *Journal of Structural Engineering*, 120(5):1510–1524, 1994.

[93] Washington State DOT. *WSDOT Pavement Guide for Design, Evaluation and Rehabilitation*, 1993.

[94] Personal communication with Joe P. Mahoney, Professor, University of Washington Deparment of Civil Engineering, Dec., 1997.

[95] E. Yamaguchi and T. Ohta. Accurate and Efficient Method of Analysis for Reinforced Concrete Structures. *Journal of Structural Engineering*, 119(7):2017–2035, 1992.

[96] S.M. Zaghloul, T.D. White, and T. Kuczek. Evaluation of Heavy Load Damage Effect on Concrete Pavements Using Three-Dimensional, Nonlinear Dynamic Analysis. In *Transportation Research Record 1449*, pages 123–133, Washington, D.C., 1994. TRB, National Research Council.

[97] M. Zaman and A. Alvappillai. Contact-Element Model for Dynamic Analysis of Jointed Concrete Pavements. *Journal of Transporation Engineering*, 121(5):425–433, 1995.

[98] O.C. Zienkiewicz and R.L. Taylor. *The Finite Element Method - Volume I.* McGraw-Hill Book Company, 1994.

[99] O.C. Zienkiewicz, J.P. Vilotte, S. Toyoshima, and S. Nakazawa. Iterative Methods for Constrained and Mixed Approximation. An Inexpensive Improvement of FEM Performance. *Comp. Meth. Appl. Mech. Eng.*, 51:3–29, 1985.

McKenna lists four broad categories of classes that have been used in most object-oriented finite element programs [62]:

1. Modeling classes for generation of the finite element model.

2. Finite element model classes used to describe the model and store analysis results. Classes in this category include representations for nodes, elements, boundary conditions, and loads.

3. Numerical classes that handle computational operations, generally basic matrix, vector and tensor operations.

4. Analysis classes, used to form and solve the governing equations. Generally, analysis classes interact with the finite element model classes to assemble the system stiffness matrix and load vectors, compute the residual force vector, etc.

Model generation has not been considered in this study, and model geometry and properties are defined in separately developed input files. Categories (2) - (4) are detailed in the remainder of this Section. With this framework in hand, the object-oriented implementations of the more complex computational aspects of the present study (i.e. the embedded dowel element, multigrid solution strategies, etc.) will be discussed in later sections.

A.2.2 Finite Element Model Classes

The finite element model classes may be grouped into three major categories:

1. Model geometry, including nodal locations, element connectivities, and zero-displacement boundary conditions.

2. Element definitions, which include both material properties and computational aspects of the element discretization.

3. Loads.

The objects representing these three categories are depicted in Fig. A.1.

Model Geometry

Model geometry is represented by the *Mesh* class, which primarily provides storage for and access to lower level objects. Included in the *Mesh* class are dynamically-sized arrays of *Node* objects used to represent nodes in the finite element model. Each *Node* stores an

(x, y, z) location, the elements of which may be modified and retrieved via public member functions. The *Mesh* class also contains a dynamically-sized array of *El_conn* objects used to store element connectivities; each *El_conn* contains as member data an integer array of node numbers which may be individually accessed and modified much as elements of a vector. Nodal boundary conditions (free/fixed displacement specifications) are stored by *Nodal_bc* objects, one of which exists for every *Node*. Aside from storing and providing access to the model geometry and boundary conditions, the *Mesh* class also stores the current system displacement vector. The main computational public member function contained in the *Mesh* class is that used to form the graph of the system stiffness matrix prior to its assembly.

Element Representation

Three natural divisions were made with regard to element type, and corresponding virtual base classes were developed from which specific elements can be derived:

- The *Element* base class was designed to represent displacement-based solid and planar (in 2D) continuum elements. Both the 20-noded brick element (*Brick_20*) and 10-noded tetrahedral element (*Quad_tetra* – limited implementation) are derived from this class.

- The *Beam* class represents line elements; the 3-noded *Dowel* element and 2-noded *Beam_2* element are derived from this class.

- The *Foundation* class was developed to implement the Winkler foundation model; at present, only the quadratic *Liq_found8* element has been implemented.

This element hierarchy is illustrated in Fig. A.1. In general, each element contains public member functions for the formation and retrieval of element stiffness matrices and computation of nodal stresses and/or member forces which are required by the solution routines. Each element is also responsible for storing its nodal degrees of freedom, used in mesh traversal and mapping element vectors/matrices to system vectors/matrices. In addition, the *Element*, *Beam*, and *Foundation* classes have special functions specifically required for the analysis methods and solution strategies developed in this study which are detailed later in this Appendix. Each element contains a pointer to a material property object created independently at the time of model generation which defines appropriate constitutive relations. A single material property object may be shared by elements of the same material.

vectors. As with self-weight, the individual *Element* objects are responsible for integrating temperature-induced stresses over their volume to determine equivalent nodal loads.

A.2.3 Numerical Classes

Dense Array and Vector Classes

To facilitate element-level operations such as forming element stiffness matrices and computing element residual force vectors and loads, a set of class objects was coded specifically for linear algebra using dense matrices. These objects support zero-based parenthetical indexing through overloading of the "()" operator. Storage is allocated upon construction, and the objects may be dynamically resized at any time. To maximize performance, no checking for out-of-bound indices is supported; the programmer is responsible for sizing all arrays/vectors prior to element assignment/retrieval and matrix operations. All of the computations performed in this study were done in double precision. However, the class objects reference the global type definition `typedef double Number`, which would permit recompilation of a single precision version if desired. Throughout this Appendix, *Number* and *double* are used interchangeably.

These classes support symbolic linear algebra operations (matrix-vector multiplication, vector dot products, etc.) through public member functions employing overloaded operators. For example, the product of matrix $\mathbf{A}$ with vector $\mathbf{x}$ giving the vector result $\mathbf{b}$ is coded as $\mathbf{b} = \mathbf{A} * \mathbf{x}$. Results of computations are returned by reference to object member data to increase efficiency, i.e. the vector result $\mathbf{b}$ is returned by reference from $\mathbf{A}$ in the previous example.

A brief description of the individual objects is given below:

- *dubVector* is a simple vector class containing an array of *Numbers*. Vectors may be created using an empty constructor, as having a specified number of elements, or as defined by two *Nodes*. Public member functions support vector dot and cross products, vector-matrix multiplication, vector tensor products, assignment of a scalar or another vector (with dynamic reallocation), retrieval of maximum or minimum values, and sorting of values.

- *dub2Darray* is a dense matrix class. Arrays may be sized upon construction or dynamically resized after instantiation. Overloaded operators permit matrix-matrix and matrix-vector operation, etc. Individual columns or rows may be assigned or extracted, as may block matrices.

Member functions are also provided for access to `nzval`, `rowind`, and `colptr` as required by the *LU_Solver* object (described later). Other *Sparse_Col_K* public member functions are required for the multigrid solution strategies and are detailed in later sections.

A.2.4 Analysis Classes

The *Solver* object is the top level analysis object, and implements the solution strategy outlined in Algorithm 6.1. As shown in Fig. A.2, *Solver* relies on a *Constraint* class for enforcing fixed non-zero displacement and frictionless contact constraints (detailed in a later section of this Appendix). Description of the *Multi_grid* and *Conj_grad* classes used in

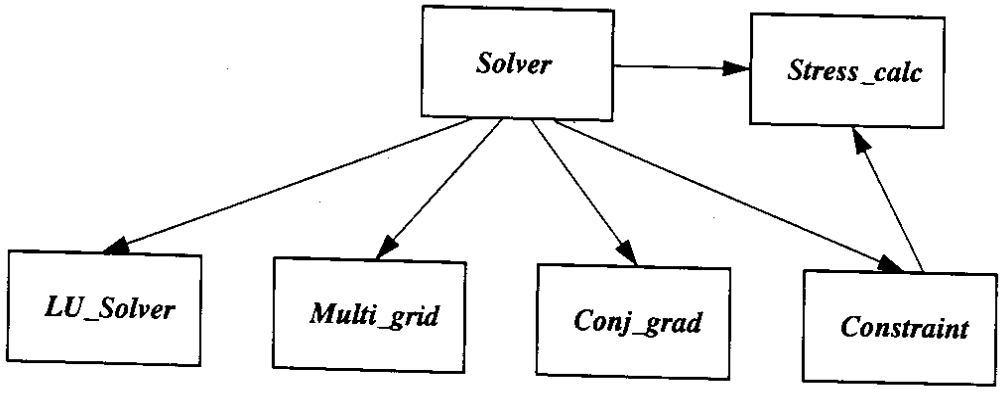

Figure A.2: Analysis Classes

the solution of the linearized system stiffness equations are also deferred until later in this Appendix.

The *LU_Solver* object is merely a wrapper providing an interface to the SuperLU sparse direct solver library routines [17, 57]. The *Multi_grid* class relies on *LU_Solver* for achieving the coarse grid solution; *LU_Solver* may also be used to directly solve the system stiffness equations for smaller problems that do not require the use of iterative solution methods. Public member functions are provided for factoring $\mathbf{K}$, and substitution for the solution. Multiple substitutions may be performed after a single factorization to increase efficiency.

Smoothed nodal stresses, along with nodal displacements, are the primary output from the finite element analysis. In addition, they are required for updating nodal contact constraints as detailed in Chapter 6. The *Stress_calc* object averages and stores the smoothed nodal stresses over the entire mesh. Each *Element* object is responsible for computing its contribution to the smoothed nodal stresses based on extrapolating the integration point stresses.

One other issue which must be addressed upon embedment of the dowel is its additional nodal connectivity and number of degrees of freedom. As mentioned earlier, each *Element*, *Beam*, and *Foundation* object stores its nodal degrees of freedom for purposes of mesh traversal, sizing of data structures, and mapping element matrices/vectors to the global matrices/vectors. Therefore, upon embedment the *Dowel* simply appends the nodal degree of freedom information as retrieved from **embedder** to its original unembedded nodal degree of freedom data. This implies that the dowel has *six* degrees of freedom at its three original nodes and *three* degrees of freedom at the nodes corresponding to **embedder** – see Chapter 4 for details. The nodal connectivity of the embedded dowel is then modified by a call to a *Mesh* public member function. These two steps, accomplished with a few lines of code in the *Dowel* `assign_embed` member function, ensure that interaction with other objects such as *Mesh* and *Sparse_Col_K* through existing *Dowel* public member functions is unaffected.

A.3.2 The *Dowel_gap* Class

The *Dowel_gap* object was created to facilitate the storage and updating of nodal constraint and bond information for all embedded *Beam* elements in a model. Member data for the *Dowel_gap* object include the following:

```
Member* ptr_to_members;
Mesh* ptr_to_mesh;
Sparse_Col_K* K;
El_conn bond_info;
El_conn constraint_info;
dubVector nodal_gaps;
```

Access to the *Beams* is provided through `ptr_to_members`, and bond, constraint on/off, and gap magnitudes are stored in `bond_info`, `constraint_info`, and `nodal_gaps`, respectively. The following public member functions provide the *Beam* objects with information required to form **T**:

`int get_bond_info(int node_num)`
Returns a 1 if node is bonded, 0 if not.

`int get_constr_info(int node_num)`
Returns a 1 if node is constrained, 0 otherwise.

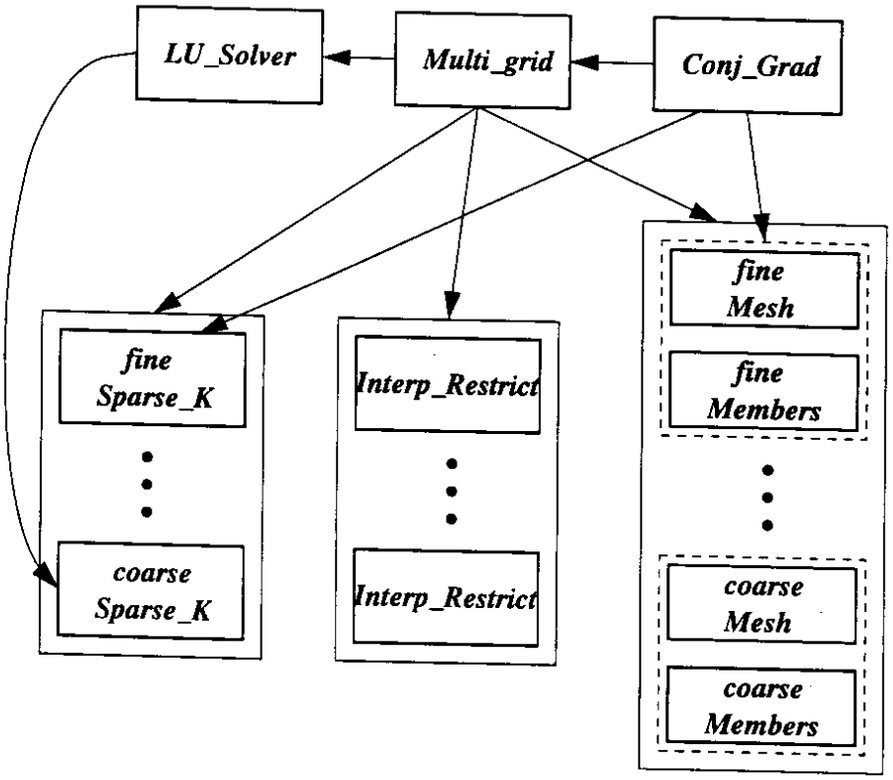

Figure A.3: Multigrid Class Structure and Implementation

operators developed in Chapter 6. Smoothing is the simplest fundamental component of the multigrid implementation. Recall that point-wise Gauss-Seidel smoothing is used, which requires only the system stiffness matrix and the current residual and displacement vectors. As such, additional functions were simply added to the *Sparse_Col_K* object to perform forward and backward Gauss-Seidel smoothing operations. Implementation of the intergrid transfer of information concepts presented in Chapter 6 is more detailed, and is the focus of the following discussion.

A.4.2 Intergrid Transfer of Information

At the heart of the intergrid transfer of information concepts developed in Chapter 6 lies the need to efficiently determine for any *Node*: (1) the element it is contained within, and (2) the local (natural) coordinates of the containing element. This information is required for restriction/interpolation as well as the intergrid transfer of material properties, where all coarse mesh elements must access the finest mesh at their integration points. As detailed in Chapter 6, a grid searching procedure is needed to reduce the number of elements which must be checked for each *Node*. This grid search has been implemented using the *Grid_sort*

```
build_sort()
 1  [X_min, X_max, Y_min, Y_max] = Mesh → get_mesh_limits()
 2  δx = (X_max − X_min)/n_dx
 3  δy = (Y_max − Y_min)/n_dy
 4  ▷ loop over all elements
 5  for i = 1 to number of elements
 6  do [x^i_min, x^i_max, y^i_min, y^i_max] = Mesh → get_el_limits(i)
 7      ▷ starting and ending cell indices
 8      low_x = (int) (x^i_min − X_min) /δx
 9      high_x = (int) (x^i_max − X_min) /δx
10      low_y = (int) (y^i_min − Y_min) /δy
11      high_y = (int) (y^i_max − Y_min) /δy
12      ▷ loop over each row in grid
13      for j = low_y to high_y
14      do k_s = j * n_dx + low_x
15          k_e = j * n_dy + high_x
16          ▷ loop over each column in grid
17          for k = k_s to k_e
18          do el_nums[k].add_val(i)
19          end
20      end
21  end
```

Algorithm A.1: Pseudo-code for the `build_sort` Function

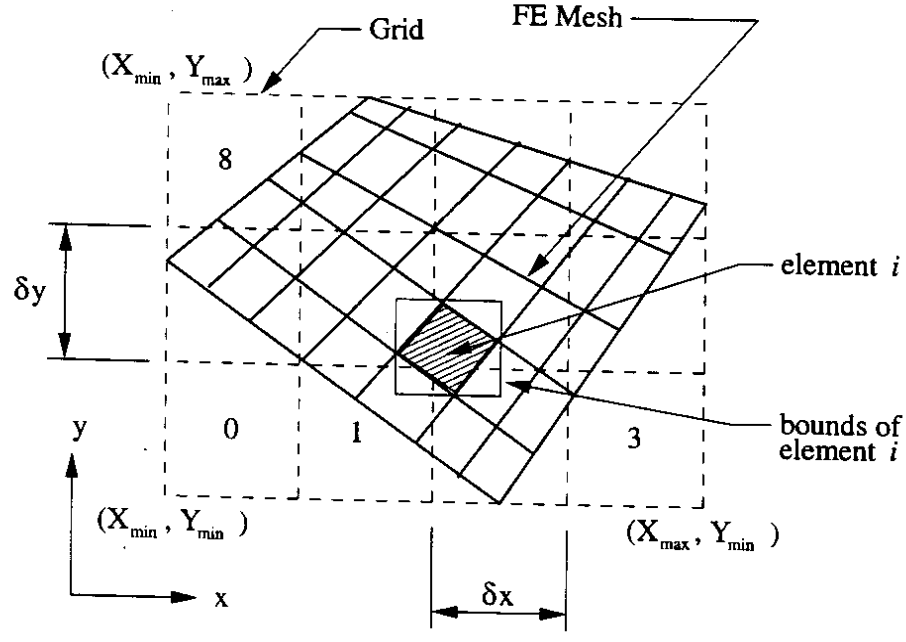

Figure A.4: Definitions for Grid Searching Algorithm

where:

$$\begin{aligned}
\mathbf{x} &= \text{3-element vector containing the given } (x, y, z) \text{ location} \\
\mathbf{x}^* &= \text{vector of element nodal locations, } [x_1, y_1, z_1, \ldots x_b, y_b, z_b]^{\mathbf{T}} \\
\mathbf{N} &= \text{the matrix of element shape functions} \\
\boldsymbol{\Upsilon} &= \text{vector of element local coordinates, } (\xi, \eta, \zeta)
\end{aligned}$$

Applying Newton's method for the solution of this equation requires the Jacobian, $\mathbf{J}$, given by:

$$\mathbf{J} = \begin{bmatrix} \frac{\partial N_i}{\partial \xi} x_i & \frac{\partial N_i}{\partial \eta} x_i & \frac{\partial N_i}{\partial \zeta} x_i \\ \frac{\partial N_i}{\partial \xi} y_i & \frac{\partial N_i}{\partial \eta} y_i & \frac{\partial N_i}{\partial \zeta} y_i \\ \frac{\partial N_i}{\partial \xi} z_i & \frac{\partial N_i}{\partial \eta} z_i & \frac{\partial N_i}{\partial \zeta} z_i \end{bmatrix}$$

where summation over i is implied. A review of isoparametric element definitions reveals that $\mathbf{J}$ is the transpose of the Jacobian used in coordinate mapping operations [98, 20], and no extra element functionality is required for its computation. Solution for the unknown element local coordinate vector, $\boldsymbol{\Upsilon}$, using Newton's method then follows as:

```
int get_local(x, Υ)
1  ▷ start at center of element
2  Υ = (0,0,0)
3  while ‖G(Υ)‖ > 0
4  do J = form_Jacobian()
5      ▷ solve for increment
6      δΥ = J⁻¹G
7      Υ+ = δΥ
8  end
```

Algorithm A.2: Solve for Element Local Coordinates

Restriction and Interpolation

Since restriction and interpolation as defined in Chapter 6 employ the same information about adjacent meshes in the hierarchy, it was logical to develop a single class, *Restrict_interp*, to perform these operations between adjacent *Mesh/Members* pairs as shown Fig. A.5. This implies that the number of *Restrict_interp* objects is always one less than the number of meshes in the hierarchy. In addition to constructors and a destructor, the *Restrict_interp* class provides only three public member functions:

incurred by the evaluation of the element shape functions for each restriction/interpolation operation is minimal.

Intergrid Transfer of Material Properties

The intergrid transfer of material properties is accomplished at the element level with the following additional required element member functions:

```
void assign_members(Members* fine_members)
void get_D(Node& gauss_nodes[i], dub2Darray& D)
```

After the elements of all coarser meshes in the multigrid hierarchy have been constructed, they are assigned pointers to the fine *Members* object. The fine mesh element numbers and local coordinates corresponding to the coarse mesh element integration points are computed and stored as coarse element member data. This permits the constitutive matrix, $\mathbf{D}$, relating stress and strain to be retrieved from the fine mesh elements during the calculation of the element stiffness matrix. Currently, these member functions have been added to each class in the *Element* and *Foundation* class hierarchies; the *Beam* elements do not account for spatially varying material properties when a multigrid solution is employed. Note that at present, this implementation is limited to total displacement nonlinearities (such as the aggregate interlock constitutive relations developed in Chapter 5). More complex constitutive models would require the tracking of more loading history parameters. In principle, however, a class could be developed to compute and update required parameters at each integration point, allowing the mechanisms for the intergrid transfer of material properties to remain largely unchanged.

A.4.3 Multigrid-Preconditioned Conjugate Gradient Implementation

Implementing the multigrid-preconditioned conjugate gradient solver (MG-PCG) is simple once the multigrid solver is in place. A *Conj_grad* class was coded specifically to implement the preconditioned conjugate gradient algorithm. Once the algorithm was coded, all that was required to implement MG-PCG was to give the *Conj_grad* object pointer access to *Multi_grid*.

At present, three other options are also available for preconditioning: diagonal, symmetric Gauss-Seidel, and incomplete LU factorization (ILU). The diagonal preconditioner retrieves the vector of diagonal elements from the *Sparse_Col_K* object, and the symmetric Gauss-Seidel preconditioner relies on the forward and backward smoothing routines coded

matrix, $\mathbf{K}' = \omega \mathbf{G}^k \mathbf{G}^{k\mathbf{T}}$, based on the currently active constraints. The perturbation $\mathbf{K}'$ is added if add = 1, and removed if add = -1.

The implementation of the above member functions is straightforward when a direct solver is used in the inner kernel of the solution algorithm. An additional level of complexity is added when solving constrained models using multigrid methods; this is discussed next.

A.5.2 Multigrid Methods for Constrained Problems

The only difficulty in solving the constrained system with a multigrid method (or multigrid-preconditioned conjugate gradient) lies in restricting $\mathbf{K}'$ to the coarser meshes in accordance with Chapter 6. Recall that this process of restriction is performed node-by-node, requiring that the coarse mesh element within which each fine mesh nodal stiffness perturbation, $\omega(\mathbf{n} \otimes \mathbf{n})$, be known. However, with the element search capabilities previously added to the *Members* class for the multigrid implementation, determination of this information becomes a trivial task. Similarly, the functions required for the evaluation of the coarse mesh element shape functions are already in place, permitting the calculation of Eq. 6.30 with little work. The only additional modifications involve notifying the coarse *Mesh* that there is additional coupling between nodes not defined by element connectivities to ensure that storage for the system stiffness matrix is properly allocated.

Given this simplicity, the required functionality for perturbing the coarse mesh stiffness matrices was added to the *Constraint* class. During model generation, a single *Constraint* object is constructed for each mesh in the hierarchy; however, the coarse mesh *Constraint* objects are each assigned a pointer to the finest mesh *Constraint* object. This permits each coarse mesh *Constraint* to compute its equivalent perturbation, $\mathbf{K}'$, based on the current constraint information known and updated only on the fine mesh.